UNIVERSITÀ
DEGLI STUDI
FIRENZE

Scuola di Scienze Matematiche,
Fisiche e Naturali

Corso di Laurea Magistrale
in Fisica

# Optimized production and probing of resonantly interacting lithium-chromium Fermi mixtures

**Candidate**
Antonio Cosco (ID number 6117398)

**Thesis Advisor**
Dr. Matteo Zaccanti

**Co-Advisor**
Prof. Giovanni Modugno

Academic Year 2021/2022

---

**Optimized production and probing of resonantly interacting lithium-chromium Fermi mixtures**
Tesi di Laurea Magistrale. University of Florence

This thesis has been typeset by LaTeX and the UniFiTh class.

Version: June 14, 2023

Author's email: antonio.cosco@stud.unifi.it

*A tutti quei ragazzi,*
*a tutte quelle ragazze che,*
*con la schiena curva per il peso delle aspettative,*
*hanno creduto l'università uno scoglio insormontabile*
*e si sono suicidati.*

# Abstract

Durante il mio progetto di tesi, svolto presso il Lab. 9 del *Dipartimento di Fisica*, mi sono concentrato sull'ottimizzazione dell'apparato sperimentale per la produzione e caratterizzazione di una nuova miscela fermionica di atomi di litio e cromo ultrafreddi. Ho contribuito alla costruzione e all'implementazione di nuove componenti dell'esperimento per indagare più approfonditamente i fenomeni derivanti dalle interazioni risonanti tra $^6$Li e $^{53}$Cr. Inizialmente, ci siamo dedicati all'ottimizzazione dei protocolli sperimentali, al fine di ottenere un campione di cromo ultrafreddo sempre più grande. Abbiamo inoltre introdotto un secondo potenziale ottico che ha consentito di aumentare il confinamento della miscela senza modificarne la temperatura, permettendoci di incrementare notevolmente la densità del campione. Ciò ha permesso di realizzare la prima miscela fermionica degenere di $^6$Li -$^{53}$Cr al mondo, con $2\times10^5$ atomi di litio e $1\times10^5$ atomi di cromo, ad una temperatura relativa di $T/T_F \sim 0.25$ per entrambe le specie. Successivamente, mi sono focalizzato sull'utilizzo di una risonanza di Feshbach eteronucleare, identificata precedentemente al mio lavoro di tesi, per la creazione di dimeri di LiCr. Grazie ai progressi raggiunti nella realizzazione della miscela degenere, è stato possibile produrre un considerevole campione di $5\times10^4$ dimeri di LiCr, di cui abbiamo intrapreso una prima caratterizzazione. Il mio principale contributo all'esperimento ha riguardato la realizzazione di un'antenna a radio-frequenza (RF) per trasferire efficientemente atomi di $^{53}$Cr tra i due livelli Zeeman a energia più bassa, compito che ha richiesto il superamento di diverse sfide. Poichè al campo cui si trova la risonanza di Feshbach Li-Cr di 1414 G l'accoppiamento tra i due stati è debole, per ottenere trasferimenti RF su tempi di poche centinaia di µs l'antenna deve lavorare a corrente alta. Inoltre, il design del setup RF ha dovuto tener conto dei vincoli dettati dal sistema da vuoto e dai vari fasci laser dell'apparato principale. Traendo spunto da un design sviluppato recentemente da colleghi del *LENS* per un'antenna RF con frequenze di lavoro a 80 MHz, adattandolo al nostro range spettrale e vincoli fisici del setup, siamo riusciti a costruire un'antenna altamente performante che rispecchiasse tutte le caratteristiche richieste. L'implementazione del nuovo setup RF per il cromo mi ha permesso di caratterizzare il rumore di campo magnetico dell'esperimento e di migliorarne significativamente la stabilità. Questo secondo significativo miglioramento tecnico è stato raggiunto grazie all'implementazione di un sistema di compensazione delle fluttuazioni del campo, principalmente causate da un rumore della corrente a 50 Hz. Tale schema, che ho implementato con successo e caratterizzato sperimentalmente, è basato sull'invio, ad una ulteriore bobina posta sopra la camera da vuoto, e concentrica rispetto alle bobine principali, del segnale di rumore (invertito opportunamente) che risulta nella generazione di un campo oscillante opposto alle fluttuazioni precedentemente misurate. Questo metodo, una volta ottimizzato, ci ha consentito di raggiungere una stabilità del campo magnetico di circa 3.6 mG, a un campo di 1414 G, ottenendo cioè una fluttuazione residua di circa $2.5\times10^{-6}$. Questi progressi tecnici, da me concepiti e implementati sul setup sperimentale pre-esistente, hanno permesso di iniziare negli ultimi mesi della mia tesi, un'accurata caratterizzazione di miscele fermioniche Li-Cr fortemente interagenti, aprendo la strada anche a molte future investigazioni di questo nuovo sistema bi-atomico ultrafreddo.

# Abstract

During my thesis done in the LiCr experiment, located in Lab. 9 of the *Department of Physics*, I focused on the optimisation of the experimental apparatus for the production and characterization of the novel fermionic mixture of ultracold lithium and chromium atoms. I contributed to the construction and implementation of new components of the experiment to further investigate phenomena arising from resonant interactions between $^6$Li and $^{53}$Cr. During the first part of my thesis I was taking part to optimise the experimental protocols in order to obtain a larger sample of ultracold chromium. I introduced a second optical potential in addition to the primary optical trap. This made it possible to increase the confinement of the mixture without changing the temperature, and to significantly increase the density of the sample. This allowed us to realise the world's first degenerate fermionic mixture of $^6$Li -$^{53}$Cr, with $2 \times 10^5$ lithium atoms and $1 \times 10^5$ chromium atoms, at a relative temperature of $T/T_F \sim 0.25$ for both species. This achievement served as a starting point to produce heteronuclear Feshbach dimers using a previously identified Feshbach resonance. We routinely obtain $5 \times 10^4$ LiCr dimers which we currently characterize thoroughly. This requires very good magnetic field stability and fast radio-frequency (RF) transfer. The main part of my thesis was to realise a RF antenna to efficiently transfer $^{53}$Cr atoms between the two lower-energy Zeeman levels, which turns out to be challenging. At the field of the Feshbach resonance of 1414 G, the weak coupling strength between the two states requires that the antenna must be operated at high currents in order to achieve Rabi oscillation times of order of hundreds of microseconds. Furthermore, the design of the RF setup had to take into account the constraints imposed by the vacuum system and the various laser beams of the main apparatus. I have adapted the recent design of a RF antenna working for lithium at 80 MHz, developed at *LENS*, to work with the three times higher frequency of chromium of 240 MHz. I have simulated and optimized the components and have built and characterized the antenna with the atoms and I have proven its efficiency. The implementation of the new RF setup for chromium also allowed me in the last part of my thesis to characterise the magnetic field noise of the experiment and significantly improve its stability. This second significant technical upgrade was achieved through the implementation of a compensation scheme for field fluctuations, mainly caused by 50 Hz current noise and higher harmonics. This scheme, which I have successfully implemented and experimentally characterised, is based on creating, with an additional coil, an inverted noise signal opposite to the previously measured fluctuations. This method, once optimised, allows us to achieve a magnetic field stability of 3.6(6) mG, at a field of 1414 G, resulting in a residual fluctuation of $2.5(4) \times 10^{-6}$. These technical advances, which I conceived and implemented on the existing experimental setup, allowed me to begin, in the last months of my thesis, an accurate characterization of strongly interacting Li-Cr fermionic mixtures, also paving the way for many future investigations of this new ultra-cold diatomic system.

# Contents

# Introduction

Quantum matter composed by unequal kinds of fermionic particles, such as quarks of different colors, or electrons belonging to different lattice bands, is known to promote a plethora of exotic phenomena [1–6], qualitatively distinct from those characterizing single-component systems. The combination of quantum statistics with a mass asymmetry and a distinct response to external fields of two different fermionic species, indeed provides an increased level of complexity, with a strong impact both at the few- and many-body level. In this context, heteronuclear Fermi mixtures of ultracold atoms, resonantly interacting close to a Feshbach resonance [7], are regarded as clean and versatile frameworks optimally-suited for the disclosure of exotic few-particle states [8–20], and the exploration of novel quantum phases – primarily in the context of unconventional superfluid pairing [21–31] and quantum magnetism [32–36].

In particular, Fermi mixtures with mass ratios $8.17 \lesssim M/m \lesssim 13.6$ are especially appealing from a few-particle physics perspective, as they are predicted to support, already in three dimensions, non-Efimovian few-body cluster states, completely unexplored thus far, which exhibit universal character and a peculiar $p$-wave orbital symmetry [9, 13, 15, 18, 37]. These elusive states are extremely relevant also from a many-body viewpoint, in light of their collisional stability. In fact, owing to the *halo* nature of such non-Efimovian clusters, largely exceeding in size the van der Waals range of the interatomic interaction potential, their existence does not trigger an increase of inelastic decay processes [38], in stark contrast to the widely-explored Efimovian case [39]. Therefore, the presence of fermionic trimers [9,13,15] and bosonic tetramers [18,37] – expected to exist for $8.17 \lesssim M/m \lesssim 13.6$ [9] and $8.86 \lesssim M/m \lesssim 13.6$ [18], respectively – may uniquely allow one to experimentally attain qualitatively new many-body regimes, within which strong few-body correlations add to, or may even overcome, the standard two-body ones. Yet, none of the Fermi-Fermi mixtures nowadays available, i.e. $^{6}$Li-$^{40}$K [40–42], $^{40}$K-$^{161}$Dy [43, 44] and $^{6}$Li-$^{173}$Yb [45, 46], exhibits a mass ratio that allows to probe such an appealing scenario, although related few-body effects have been disclosed in Li-K [47].

Our interest for the novel lithium-chromium system is three-fold: first, the peculiar chromium-lithium mass ratio, of about 8.8, is extremely close to the critical values above for which both three- and four-body non-Efimovian states are predicted to emerge [9, 13, 15, 18, 37]. This feature, combined with the recent discovery of various magnetic Feshbach resonances well suited to control Li-Cr interactions [48], makes such a bi-atomic combination an unparalleled framework with which to explore a new class of *elastic* few-body effects and their impact at the many-body level [15, 18]. Second, in the regime of strong repulsive interactions, three-body recombination processes are predicted to be drastically suppressed for the specific Li-Cr mass ratio [49], lithium-chromium Fermi mixtures thus representing a pristine platform to explore Stoner's ferromagnetism [50] and related phenomena [51–55], "immune" to the pairing instability. Finally, recent *ab initio* calculations [56] foresee, for the ground state of the LiCr dimer, a sizable electric dipole moment of about 3.3 Debye, combined with a $S=5/2$ electronic spin, thereby making Li-Cr mixtures also extremely appealing candidates to realize ultracold paramagnetic polar molecules.

Our strategy to produce degenerate lithium-chromium Fermi mixtures is formally similar to the all-optical one developed for the lithium-potassium system in the Innsbruck experiment [57]. In spite of its conceptual simplicity, successful application of this approach to Li-Cr mixtures has required to tackle various challenges – mostly connected with fermionic chromium and its rather limited experimental investigation [58–60]. Specifically, a few major issues make the production of ultracold $^{53}$Cr gases non-trivial. First, chromium suffers from rather strong light-assisted inelastic collisions [58], which so far limited the $^{53}$Cr number collected in the MOT to roughly $10^6$ [60]. Second, direct loading of chromium atoms from the MOT into an infrared optical dipole trap has proved to be challenging, owing to detrimental light-shifts [61, 62]. Finally, efficient sympathetic cooling of chromium with lithium should not be taken for granted. Although the Li-Cr background scattering length, of about 42 $a_0$ [48], is close to the Li-K one [40, 63] – and thus sufficient to guarantee a good thermalization rate – efficient Li-Cr sympathetic cooling in a standard 1070 nm optical trap is hard to achieve, given that the chromium polarizability, relative to the lithium one, is about $1 \div 3$, in contrast with a potassium-to-lithium polarizability ratio of about 2 at such wavelength [57].

A detailed description of the experimental protocols, that I contributed to devise in Lab. 9 during the first part of my thesis, to produce large double-degenerate Li-Cr Fermi mixtures will be subject of Chapter 2. These results are reported in the recently published work [64].

Once the quantum degeneracy of such a novel bi-atomic system was experimentally attained, our activities focused on the investigation of Li-Cr mixtures in the regime of resonant inter-species interactions.

Specifically, by employing two $s$-wave Li-Cr Feshbach resonances that were identified before the start of my thesis, we focused on characterization of the atom-molecule conversion process. Feshbach dimer formation representing a fundamental step towards few- and many-body studies with strongly-interacting Li-Cr Fermi mixtures, and also being the crucial starting point to realize, in the future, quantum gases of ground-state LiCr molecules.

A summary of the first experiments that I contributed to conduct on this topic will be given in Chapter 3. While the outcome of this characterization indeed appeared extremely promising – as we could demonstrate the ability to create ultracold LiCr molecular samples of more than $5 \times 10^4$ dimers, with atom-to-molecule conversion efficiency above 60% – these first attempts also revealed some technical issue of our setup, which needed to be solved, in order to go further with the investigation of the mixtures under resonant conditions.

Overcoming these technical problems with upgrades to the experimental apparatus represents the major activity that I carried out during my thesis. In particular, a first contribution that I made to the Li-Cr experiment is to device, realize and integrate on the main experimental machine an efficient RF antenna to perform coherent transitions between adjacent Zeeman levels of chromium, at high fields exceeding 1400 G. This major work is reported in Chapter 4 of this thesis.

A second technical improvement I was able to contribute successfully during my master thesis period is represented by the implementation of an advanced stabilization scheme of the magnetic field bias near the high-field Li-Cr Feshbach resonance. As a result of my efforts, I could achieve a few mG stability of the magnetic field around 1400 G, as I will describe in Chapter 5. There I will also briefly show how the successful realization of the chromium antenna, combined with the achieved field stability, allowed us to recently characterize some properties of LiCr Feshbach dimers.

# Chapter 1

# Fundamental properties of two- and three-body fermion systems: a basic introduction

In this Chapter, I summarize the theoretical background useful to understand the main scientific results obtained during my thesis. My aim is to give an overview of the physical phenomena and theoretical tools that are pertinent for understanding resonantly-interacting atoms (and molecules) in the ultracold regime. In particular, I will recall some well-established textbook results on two-particle scattering, focusing on collisions that occur at low energy, relevant for ultracold gases. I will then discuss the Feshbach resonance phenomenon, and recall the properties of two-body systems under strongly-interacting conditions. This chapter follows [65].

## 1.1 Two-body scattering physics

When two quantum particles having mass M and m, respectively, collide with each other, their states and wavefunction are altered, as a result of their interaction via the interatomic potential $V(\mathbf{r})$, where $\mathbf{r}$ represents the distance between the particles. If $V(\mathbf{r})$ is non-zero, the motion of the pair changes with respect to the case without interaction, in which a plane wave $\sim e^{ikz}$ describes the pair's motion in the center-of-mass frame, $\boldsymbol{k}$ denoting the relative momentum. The scattering energy is given by $\hbar^2 k^2/(2m_r)$, where $m_r$ is the reduced mass calculated as $Mm/(M+m)$. In particular, a non-zero interaction results in an extra component that adds to the system wavefunction. For $\mathbf{r}$ approaching infinity, this component takes the form of an outgoing spherical wave $\sim e^{ik'r}/r$, which combines with the incoming plane wave. The scattering amplitude, $f(\boldsymbol{k}, \boldsymbol{k'})$, which represents the magnitude of this scattered wave, contains all details related to the collisional process, and it generally depends on the incoming (outgoing) momentum $\boldsymbol{k}$ ($\boldsymbol{k'}$). Considering the case of elastic scattering, where $|\boldsymbol{k}| = |\boldsymbol{k'}|$, and restricting to the case of a central potential ($V(\boldsymbol{r}) = V(r)$), the scattering amplitude can be expressed as a sum over partial waves with a given angular momentum quantum number $l$

$$f(\boldsymbol{k},\boldsymbol{k'}) = f(k,\theta) = \sum_{l=0}^{\infty}(2l+1)P_l(\cos\theta)f_l(k) \tag{1.1}$$

where $P_l$ are the Legendre polynomials, and $\theta$ represents the angle between the incoming and outgoing momenta. When the two particles are indistinguishable, Eq. (1.1) needs to be adjusted to account for the symmetry (or antisymmetry) properties of the bosons or fermions under particle exchange. In such a way, the partial wave expansion for identical bosons (fermions) will only include even (odd) waves, as the Legendre polynomials have a parity of $(-1)^l$.

It is possible to represent each partial-wave amplitude $f_l(k)$ in several equivalent forms expressed in terms of the associated phase shift $\delta_l(k)$ [66]

$$f_l(k) = \frac{1}{2ik}(e^{2i\delta_l(k)}-1) = \frac{1}{kcot\delta_l(k)-ik} = \frac{sin(2\delta_l(k))}{2k} + i\frac{sin^2(\delta_l(k))}{k}. \tag{1.2}$$

From the scattering amplitude the scattering cross section can be obtained making an integral over the solid angle

$$\sigma(k) = \int |f(k,\theta)|^2 d\Omega = 4\pi\sum_{l=0}^{\infty}(2l+1)\frac{sin^2(\delta_l(k))}{k^2} \equiv \sum_{l=0}^{\infty}\sigma_l(k). \tag{1.3}$$

Comparing Eq. (1.2) and Eq. (1.3) and remembering that $P_l(0)=1$ for each $l$, we obtain

$$\sigma(k) = \frac{4\pi}{k}Im\left[f(k,0)\right]. \tag{1.4}$$

It is important to note how each partial-wave component in Eq. (1.3) reaches its maximum value, named *unitary limit*,

$$\sigma_{l,MAX}(k) = (2l+1)\frac{4\pi}{k^2} \qquad \text{when } \delta_l(k) = \frac{\pi}{2}. \tag{1.5}$$

Likewise, having information about $f(k,\theta)$, also the elastic scattering rate $1/\tau$ can be determined. Considering the collision of a particle within a medium of density $\bar{n}$ the scattering rate is linked to the forward scattering amplitude averaged over all collision momenta, $\langle f(k,\theta=0)\rangle$, through the relation

$$1/\tau = \bar{n}\,\frac{\hbar}{m_r}\,4\pi\,Im\,\langle f(k,0)\rangle. \tag{1.6}$$

Additionally, $f(k,\theta)$ provides information also about the *energy shift* $h\,\delta\nu$, experienced by one particle due to its interaction with the surrounding medium. In this case one finds that [67, 68],

$$\delta\nu = -\bar{n}\,\frac{\hbar}{m_r}\,Re\,\langle f(k,0)\rangle. \tag{1.7}$$

The scattering problem becomes considerably simpler if we consider collisions at low momenta ($k\to 0$) involving short-range interaction potentials, which are those that have a power law form, $V(r)\sim r^{-\alpha}$ with $\alpha > 3$, for $r\to\infty$. This scenario is particularly relevant when we study non-magnetic atom pairs that exhibit a van der Waals interaction, represented by the potential $V_{vdW}(r) = -C_6/r^6 = -E_{vdW}(r/R_e)^6$, with $E_{vdW}$ and $R_e$ denoting the van der Waals energy and range, respectively. For that kind of short-range potentials, for each $l$ value, it can be shown that

$$\delta_l(k) \sim k^{2l+1} \qquad \text{for } k \to 0 \tag{1.8}$$

and, therefore from Eq. (1.2), that $f_l(k) \sim k^{2l}$. Consequently, when atoms undergo collisions in the ultracold regime, in which the de Broglie wavelength is much greater than the van der Waals range ($kR_e \ll 1$), the resulting scattering is primarily isotropic, namely $s$-wave ($l = 0$).

In particular (see e.g. Ref. [69] for details), the net effect of $V(r)$ on the two-body system at large inter-particle separation, $r \gg R_e$, can be formally taken into account by imposing a boundary condition at the origin for the log-derivative of the radial wavefunction $\psi(\mathbf{r})$:

$$\frac{[r\psi]'}{[r\psi]}|_{r\to 0} = k\, cot\delta_0(k), \tag{1.9}$$

the so-called Bethe-Peierls boundary conditions [70]. While in the generic scenario the replacement of $V(r)$ by the condition Eq. (1.9) does not simplify the problem – as it requires to know the phase shift – this becomes a valuable tool in the case of low-energy scattering, $kR_e \ll 1$.

In this regime, Eq. (1.2) can be approximated by expanding it in terms of the small parameter $kR_e$. Specifically, for the $s$-wave channel ($l = 0$), this expansion yields a dependence of the form

$$k\, cot\delta_0(k) \approx -\frac{1}{a} - R^* k^2 + ..., \tag{1.10}$$

where the constants $a$ and $R^*$ are defined as the *scattering length* and the *effective range parameter*, respectively. The $s$-wave scattering amplitude now becomes

$$f_0(k) = -\frac{1}{\frac{1}{a} + R^* k^2 + ik}. \tag{1.11}$$

It is important to note that this equation can be reproduced with an idealized zero-range (pseudo-)potential, thereby establishing that all short-range potentials are interchangeable provided they have the same $R^*$ and $a$.

## 1.2 The Feshbach resonance phenomenon

An essential characteristic of Eq. (1.11) is that it exhibits the familiar *Breit-Wigner* resonance shape [66]. This kind of resonance is relevant to describe low-energy collisions, when the scattering state, at energy $E = \hbar^2 k^2/(2m_r)$, is coupled to a quasi-stationary state, at energy $E_{res}$, via a coupling amplitude $\gamma > 0$, for which

$$f_{BW}(E) = -\frac{\hbar\gamma/\sqrt{2m_r}}{E - E_{res} + i\gamma\sqrt{E}}. \tag{1.12}$$

Comparing Eq. (1.12) with Eq. (1.11), equivalently recast in energy units, it is easy to verify the link between the parameters ($a$, $R^*$) and ($E_{res}$,$\gamma$), respectively:

$$a = -\frac{\hbar\gamma}{\sqrt{2m_r}E_{res}} \tag{1.13}$$

$$R^* = \frac{\hbar}{\sqrt{2m_r}\gamma}. \tag{1.14}$$

$R^*$ depends only on the coupling amplitude, while $a$ depends on both $\gamma$ and $E_{res}$. In equivalent terms, the coupling *energy* between the scattering and quasi-stationary states equals

$$\gamma^2 = \frac{\hbar^2}{2m_r R^{*2}}. \tag{1.15}$$

From Eq. (1.13) is important to note that the sign of the scattering length depends only on the sign of $E_{res}$: if $E_{res} < 0$, i.e. a real bound state exists, the scattering length is positive, while $a < 0$ only if $E_{res}$ is positive. This is possible because $\gamma$ is a positive-defined quantity.

The scattering length amplitude can be tuned if the energy $E_{res}$ can be varied with respect to the scattering threshold. In particular, when $E_{res} \to 0$, $|a| \to \infty$, that, following the Eq. (1.10), corresponds to $\delta_0 \to \pi/2$. In the case of ultracold systems, the value of $E_{res}$ can be adjusted through the Zeeman effect, resulting in the occurrence of the Feshbach resonance (FR) phenomenon [7].

A Feshbach resonance appears when two atoms in a specific hyperfine and Zeeman state configuration (denoted as the *open channel*) have their scattering threshold nearly degenerate with a molecular state supported by the interatomic potential asymptotically connected to a different hyperfine state combination, (referred to as the *closed channel*), see Fig. 1.1. Thereby having a non-zero differential magnetic moment $\delta\mu = \mu_c - \mu_o$ between closed and open channels, the energy of the quasi-stationary state can be written as $E_{res} = \delta\mu(B - B_0)$, where $B$ represents an external magnetic field, and $B_0$ the field value at which the scattering threshold and the bound state in the closed channel become degenerate. Eq. (1.13) can be expressed now as function of magnetic field

$$a(B) = -\frac{\hbar\gamma}{\sqrt{2m_r}\delta\mu(B - B_0)}. \tag{1.16}$$

By defining the magnetic width of the Feshbach resonance as

$$\Delta B \equiv \frac{\hbar\gamma}{\sqrt{2m_r}a_{bg}\delta\mu}, \tag{1.17}$$

and the background scattering length $a_{bg}$ as the value that $a$ assumes far away from $B_0$, we can re-write Eq. (1.16) as [7]

$$a(B) = a_{bg}(1 - \frac{\Delta B}{B - B_0}). \tag{1.18}$$

By appropriately combining Eq. (1.17) and Eq. (1.14) the effective range parameter is given by

$$R^* = \frac{\hbar^2}{2m_r}\frac{1}{a_{bg}\Delta B\delta\mu}. \tag{1.19}$$

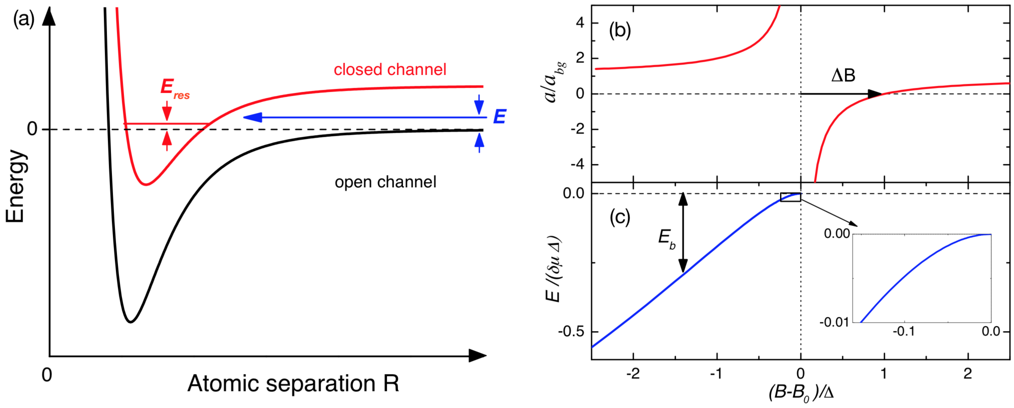

**Figure 1.1.** (a) Basic two-channel model for a Feshbach resonance. The phenomenon arises when two atoms collide with an energy $E$ in the entrance channel and become resonantly linked to a molecular bound state with energy $E_{res}$, which is supported by the closed channel potential. In the ultracold regime, collisions happen at energies close to zero, $E_{res} \to 0$. In this case, resonant coupling can be achieved by adjusting the magnetic field to tune $E_c$ close to zero, provided that the magnetic moments of the closed and open channels are not equal. (b) Scattering length $a$, and (c) molecular state energy $E$ near a magnetically tuned Feshbach resonance. The binding energy is defined to be positive, $E_b = -E$. The inset shows the universal regime near the point of resonance where $a$ is very large and positive. Figure taken from [7].

If we consider that large (small) values of $\gamma$ indicate strong (weak) coupling between the scattering channel and the quasi-discrete level, we can alternatively classify a Feshbach resonance as *broad* or *narrow*, depending whether the effective range parameter in Eq. (1.19) is smaller or larger than the true range of the potential $R_e$: $R^* \leq R_e \Rightarrow$ broad resonance; $R^* \gg R_e \Rightarrow$ narrow resonance. In Ref. [7], this classification is made using a *dimensionless resonance strength parameter* $s_{res}$, which can be written as $s_{res} \sim 0.96R^*/R_e$. Narrow resonances are characterized by a small value of this parameter, $s_{res} \ll 1$. Vice-versa, $s_{res} \gg 1$ for broad resonances.

## 1.3 Feshbach dimer

As mentioned above, close to the resonance position at $B_0$, the two channels are strongly coupled, and the scattering length is very large $|a| \gg R_e$. Let us now move to consider how the finite coupling $\gamma$ with the open channel modifies properties of the bound state near the FR, otherwise represented by a closed-channel molecule for $\gamma = 0$. To this end, we look for the pole of $f_0(k)$ in Eq. (1.11) at negative energies: i.e, we replace $k \to i\kappa$, with $\kappa > 0$, so that $\epsilon_b = -\frac{\hbar^2\kappa^2}{2m_r} < 0$, with the associated wavefunction falling off like $\psi_b(r) \sim e^{-\kappa r}/r$ at $r \gg R_e$. We thus look when

$$\frac{1}{a} - R^*\kappa^2 - \kappa = 0. \tag{1.20}$$

It is easy to verify that this happens only when $a>0$, for

$$\kappa = \frac{\sqrt{\frac{4R^*}{a} + 1} - 1}{2R^*} \equiv \frac{1}{a^*}, \tag{1.21}$$

thus yielding

$$\epsilon_b = -\frac{\hbar^2}{2m_r a^{*2}}. \tag{1.22}$$

The above result interpolates between two familiar forms obtained in the limits of small and large $R^*/a$ values, respectively: For $R^*/a \ll 1$ – i.e. close to the resonance pole, or in the broad resonance case – one has $1/a^* \sim 1/a$, so that Eq. (1.22) becomes

$$\epsilon_b|_{R^*/a \ll 1} \sim -\frac{\hbar^2}{2m_r a^2} \equiv \epsilon_0. \tag{1.23}$$

A plot of the binding energy as function of magnetic-field detuning is shown in Fig. 1.1(c). In this case, the bound state energy features a typical parabolic trend $\epsilon_0 \propto -1/a^2 \propto -(B-B_0)^2$: the dimer is a halo state whose energy and wavefunction solely depend on the scattering length $a$ (universal regime). In the opposite limit $R^*/a \gg 1$, instead, $1/a^* \sim 1/\sqrt{aR^*}$ and, exploiting Eqns. (1.18) and (1.19), one finds a dimer energy trend

$$\epsilon_b|_{R^*/a \gg 1} \sim -\frac{\hbar^2}{2m_r a R^*} = \delta\mu(B-B_0). \tag{1.24}$$

In this case, the bound state energy linearly decreases with the field detuning, and it coincides with the one of the bare closed-channel molecule. It is important to emphasize that the dimensionless parameter $R^*/a$ also quantifies the open/closed channel fraction characterizing the (dressed) Feshbach molecule in the zero-range approximation. Referring the interested reader to Ref. [69] for the derivation of the result, it is useful to keep in mind that the dimer open-channel fraction is given by

$$P_{open} = \frac{1}{\sqrt{1+4R^*/a}}, \tag{1.25}$$

and, correspondingly, the closed-channel fraction is obtained as $P_{closed} = 1 - P_{open}$. It is easy to verify that, for $P_{open} \sim 1$, the binding energy follows the universal behavior Eq. (1.23) whereas, in the opposite limit $P_{open} \ll 1$, the Feshbach dimer essentially coincides with the bare closed-channel molecular state, Eq. (1.24).

Correspondingly, the magnetic moment associated with the Feshbach dimer is given by

$$\partial\epsilon_b/\partial B = \mu_o P_{open} + \mu_c(1 - P_{open}) \tag{1.26}$$

at all detunings: as such, experimental measurement of the dimer magnetic moment around a FR provides information about the magnetic field dependence of the open-channel fraction, thereby of $R^*/a$ – see Ref. [71]. In general, the transition from one regime to the other will occur at magnetic field detunings that depend on the character of the resonance considered: for broad resonances, the universal regime Eq. (1.23), with $P_{open} \sim 1$, will extend over a $B$-field region of order $\Delta B$ from the resonance center $B_0$, whereas for narrow FRs this will only occur for detunings $|B - B_0| \ll \Delta B$.

At a first glance, the distinction between narrow and broad FRs does not seem to cause a significant change: from a two-body perspective, any broad resonance becomes narrow when the incoming momenta and/or detunings are sufficiently large.

Vice-versa, also narrow resonances will behave as broad ones for sufficiently small $k$ and $|B-B_0|$ values, so that $R^*k^2 \ll 1/a$ in Eq. (1.11). In practice, though, such a distinction is highly relevant, given that in realistic situations one will have (i) a finite $B$-field stability, that limits the accuracy with which to access the $R^* \ll a$ region in experiments; (ii) a finite momentum distribution, either due to a finite thermal spread at $T > 0$ or, for fermionic samples, to the presence of a finite Fermi momentum $\kappa_F$ even at zero temperature. In the broad resonance case, one will typically have $R^* \sim R_e \ll 1/\kappa_F$, and thus all momenta $k$ will simultaneously reach unitary conditions $\delta_0(k) = \pi/2$ for $1/a = 0$. In turn, for narrow resonances and realistic densities $n = \kappa_F^3/(6\pi^2)$, $R^*\kappa_F \gg 1$, so that different momenta will reach the unitary limit, see Eq. (1.5), at different detunings. This makes that the low-temperature many-body regimes which can be accessed near broad and narrow resonances are qualitatively different, see e.g. Refs. [72–75].

# Chapter 2

# Production of a degenerate Fermi-Fermi mixture of $^{6}$Li and $^{53}$Cr atoms

In this Chapter I report on the realization of a degenerate Fermi mixture made of $^{6}$Li alkali and $^{53}$Cr transition metal ultracold atoms. This result was obtained during the first period of my thesis, and that has been already published in Ref. [64]. In particular, in the following I describe how we could overcome various challenges in the experiment, obtaining degenerate samples comprising more than $2{\times}10^{5}$ Li and $10^{5}$ Cr atoms, polarized in their lowest Zeeman states, at temperatures of about 200 nK, corresponding to $T/T_{F,Li}{\sim}T/T_{F,Cr}{\sim}0.25$ [76]. The Chapter is organized as follows: in Section 2.1 I describe our new protocol to produce a dual-species Li-Cr MOT. In particular, I discuss how the $^{53}$Cr MOT atom number can be substantially increased with respect to previous studies [58, 60], reaching up to $8{\times}10^{7}$ within a 2 s loading time and in presence of a MOT of $10^{9}$ $^{6}$Li atoms. This optimization was made by my colleagues, before starting my thesis, so I will just give here a quick summary. In Section 2.2, I present an efficient scheme to load simultaneously Li and Cr atoms in a bichromatic optical dipole trap (BODT) directly from the MOT, based on the implementation of a “dark spot”, obtained through a weak green beam at 532 nm superimposed to the main trapping beam at 1073 nm [77]. In Section 2.3, I show the evaporation trajectories followed by the two components and, in particular, how the sympathetic cooling efficiency at ultra-low temperatures can be substantially increased exploiting a narrow interspecies Feshbach resonance. Finally, in Section 2.4 I describe how a crossed bichromatic beam, added to our main BODT, allows us to strongly improve the chromium degree of degeneracy, and to simultaneously reach deeply-degenerate conditions for both atomic components. This upgrade in the experimental setup was carried out during the first months of my thesis, to which I most actively contributed.

## 2.1 Dual species $^{6}$Li-$^{53}$Cr MOT

The strategy we adopted to create a degenerate Fermi mixture consists of an all-optical approach [57] and it consists of the following main steps, summarized in

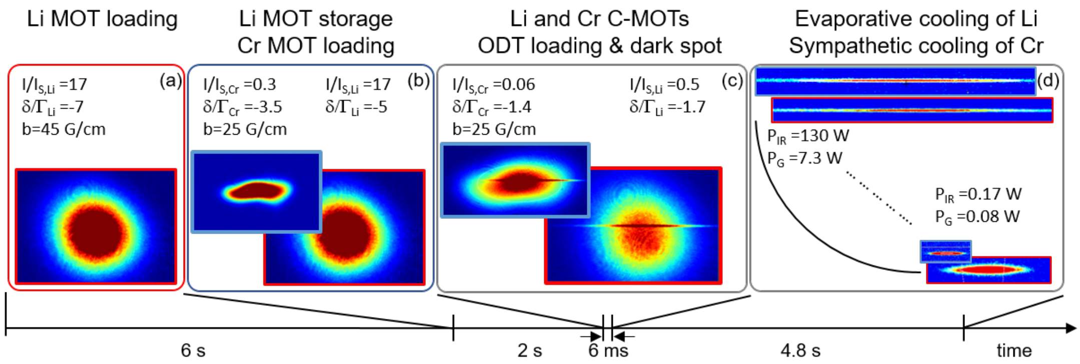

**Figure 2.1.** Schematic overview of the experimental routine discussed in the text. Our protocol consists of the following main steps: sequential loading of a cold Li-Cr mixture in a dual-species magneto-optical trap (first two panels); Efficient collection of the two components into a bichromatic optical dipole trap through the implementation of a "dark spot" for the chromium MOT (middle panel); Evaporative cooling of a two-state lithium mixture and simultaneous sympathetic cooling of chromium (last panel). Optimized values of the most relevant experimental parameters are specified for each stage. Typical absorption images, acquired at the end of each step of the routine, are shown for the two mixture components, with Li (Cr) images being framed red (blue). The time-line of the experimental cycle, overall lasting 12.8 s, is shown below the panels.

Fig. 2.1: (i) realization of a cold mixture in a dual-species magneto-optical trap (MOT) [60]; (ii) direct loading of the two components into an optical dipole trap; (iii) evaporative cooling of a two-state lithium mixture and simultaneous sympathetic cooling of chromium.

The experimental apparatus employed for the present studies, apart from targeted changes in the optical setup summarized below, has been described in detail in the previous works of Lab. 9. In particular, the experimental setup and first MOT optimization can be found in Ref. [60, 78, 79]. Details about experimental procedure, still not fully updated, and Feshbach spectroscopy are instead given in Ref. [80]. To produce the lithium MOT, we essentially follow the scheme developed by Burchianti *et al.* in Ref. [81]. Laser cooling and trapping of such a element is well-established, and it requires only two laser lights addressing the $D_2$ ($^2S_{1/2}\rightarrow{}^2P_{3/2}$) atomic line at 671 nm, see Fig. 2.2(a): the cooling light, addressing the $F = 3/2 \rightarrow F' = 5/2$ transition, and the repumper light, detuned by 228 MHz from the cooling one, near resonant with the $F = 1/2 \rightarrow F' = 3/2$ transition. With respect to the previously reported performance of the Li MOT [60], a further optimized shaping of both MOT and Zeeman slower (ZS) beams allowed us to increase the lithium atom number collected in the MOT from $4\times10^8$ to $10^9$, after a typical loading time of 6 seconds. For the $^{53}$Cr component, a much more substantial increase in the MOT atom number was achieved during the time of my thesis, resulting in an improvement by almost two orders of magnitude relative to previous studies [58, 60].

I will make use of the next pages of this section to summarize our new upgraded chromium optical setup with respect to the reported one and, after recalling some theoretical results about the MOT loading dynamics, to discuss our experimental findings and procedures to realize large cold Cr samples, also in combination with the Li component. This optimization of the chromium MOT was mainly carried out by my colleagues A. Ciamei and S. Finelli at the start of my thesis.

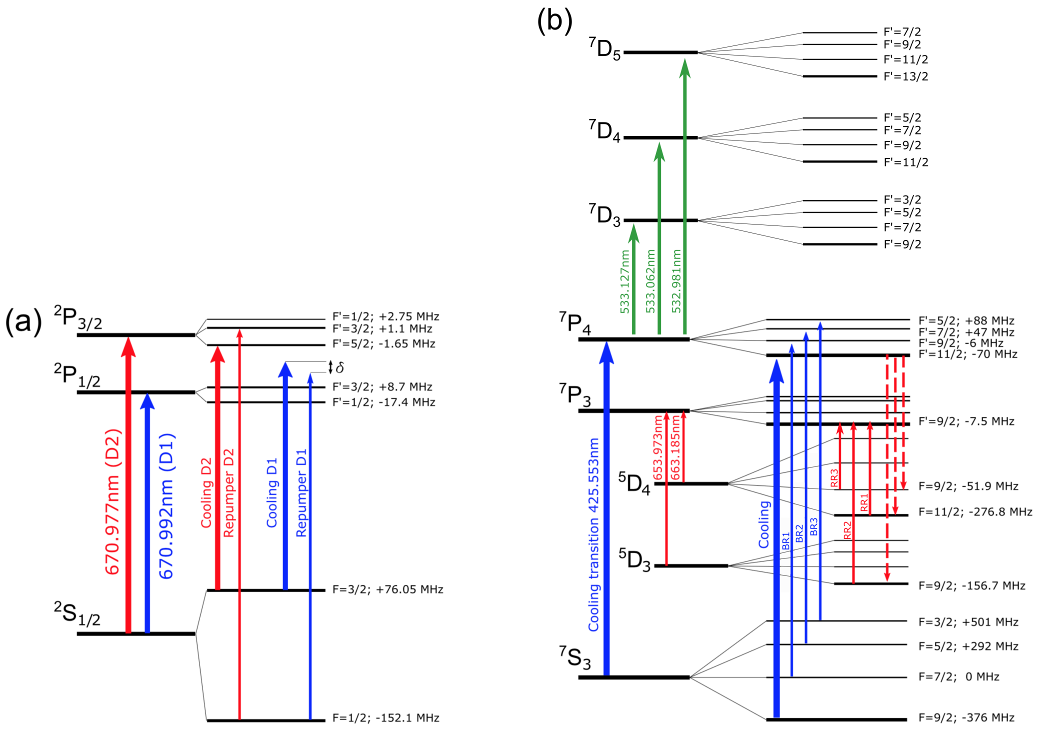

**Figure 2.2.** (a) Sketch of the fine and hyperfine energy levels relevant for the laser cooling of $^6$Li atoms (not to scale), including those exploited for the gray optical molasses based on the D1 line (blue arrows). The saturation intensities of these two lines are $I_{sat}^{D1} = 7.59\,\mathrm{mW/cm^2}$ and $I_{sat}^{D2} = 2.54\,\mathrm{mW/cm^2}$ respectively. The widths of both transition is $\Gamma = 5.87\,\mathrm{MHz}$. (b) Sketch of energy levels and optical transitions addressed for the laser cooling of $^{53}$Cr atoms (not to scale). For each relevant hyperfine level originating from the non-zero nuclear spin $I = 3/2$, the $F$ quantum number and the detuning in MHz, referenced to an assumed $I = 0$ state, are shown. A single frequency-doubled laser at 425.5 nm delivers the light exciting atoms from $^7S_3$ to $^7P_4$, addressing the main cooling transition labeled "Cooler" (solid blue), and the repumping transitions denoted $BR_1$, $BR_2$ and $BR_3$ (solid blue) in order of decreasing gain on the steady-state MOT number. Metastable $^5$D states onto which $^7P_4$ atoms decay by spontaneous emission are repumped back into the cooling cycle by three additional "red repumper" beams labeled as $RR_1$, $RR_2$ and $RR_3$, with the same indexing used for $BRs$. These lights are delivered by two independent master oscillators at 663 and 654 nm, see Ref. [60] for more details. $RR_1$ and $RR_3$, detuned from each other by only 225 MHz, are obtained by two separate sets of acousto-optic modulators. The three green transitions around 533 nm, coupling the $^7P_4$ to the $^7D_{3,4,5}$ states, are relevant for the operation of the "dark spot" discussed in Sec. 2.2.

### Improved $^{53}$Cr MOT optical setup.

As described in Refs. [58, 60], laser cooling of fermionic chromium is based on the $^7S_3 \to {}^7P_4$ ($F_S = 9/2 \to F'_P = 11/2$) atomic line, see Fig. 2.2(b) for a sketch of the energy level diagram and addressed optical transitions. Besides the cooling light, three blue repumpers, respectively denoted as $BR_1$, $BR_2$ and $BR_3$, are required to operate the MOT. Furthermore, even with all blue repumpers on, the MOT transition remains slightly leaky, since optically excited atoms can decay from the $^7P_4$ state onto underlying $^5D_3$ and $^5D_4$ metastable states. Therefore, three additional "red" repumpers, denoted $RR_1$, $RR_2$ and $RR_3$ in order of repumping efficiency, are needed to fully close the cooling cycle. In particular, $RR_3$, not implemented in previous work, Ref. [60], was introduced right before I started my thesis, which yielded a further increase of 10% in the steady-state MOT atom number.

We carefully optimized the size of all laser beams shone on the Cr MOT cloud, with the freedom of changing the power partition between different beams and under the constraint of maximum available blue power of 500 mW. In particular, we have increased the MOT and repumper beam waists by about a factor of two relative to the previous setup described in Ref. [60], now featuring $1/e^2$ radii of about 0.65 cm, effectively increasing the capture volume by almost one order of magnitude. Notably, these improvements on the chromium setup enabled us to identify a peculiar region in the detuning-intensity plane of the MOT cooling light, within which light-assisted losses are drastically suppressed, as shown in the following.

### $^{53}$Cr MOT: a few theoretical considerations.

In order to understand our strategy and the experimental data presented below, I recall some textbook results [82] about the loading dynamics in a MOT. Quite generally, the atom number in a MOT follows a time evolution defined by the rate equation

$$\frac{dN}{dt} = \Gamma_L - \alpha N(t) - \frac{\beta}{\langle V \rangle} N^2(t), \tag{2.1}$$

where $\Gamma_L$ is the loading rate, $\alpha$ is a one-body decay rate, $\beta$ is the rate coefficient per unit volume for light-assisted collisions, and $\langle V \rangle$ denotes the density-weighted volume of the cloud. Since in our experiment we exploit all (blue and red) repumping lights, we can neglect the one-body loss term, and safely set $\alpha$=0. Eq. (2.1) then yields the asymptotic value for the collected atom number

$$N_\infty = \sqrt{\frac{\Gamma_L \langle V \rangle}{\beta}}. \tag{2.2}$$

From Eq. (2.2) one can immediately see that, in order to increase $N_\infty$, one needs to maximize $\Gamma_L$ (solely dependent on the transverse cooling and Zeeman slowing parameters but not on the MOT ones), enlarge $\langle V \rangle$ and minimize $\beta$.

Let us consider how these two quantities depend upon the normalized detuning $\delta/\Gamma$ and saturation parameter $s_0 = I/I_S$ of the MOT (for the $^7S_3 \rightarrow {}^7P_4$ chromium line, the natural linewidth is $\Gamma = 2\pi\times 5.02$ MHz, and $I_S$=8.52 mW/cm$^2$ the associated saturation intensity).

In the limit of $s_0 \ll 1$ and $|\delta| \gg \Gamma$, one obtains that the MOT volume scales as [82]

$$\langle V \rangle \sim \left( \frac{\Gamma}{16\mu' k_L} \right)^{3/2} \frac{(2\delta/\Gamma)^6}{(b\, s_0)^{3/2}}, \tag{2.3}$$

where $k_L$ denotes the laser wavevector, $b$ the magnetic field gradient, and $\mu'$ the effective differential magnetic moment for the cooling transition.

The dominant light-assisted loss processes affecting a chromium MOT involve pairs of one ground $S$- and one excited $P$-state atom. Thus, denoting with $\Pi_P$ the $P$-state population, on quite general ground one expects the rate coefficient to scale as $\beta \propto \Pi_P(1-\Pi_P)$. Considering the standard result for $\Pi_P$ for a two-level atom [82], in the low-intensity and large-detuning limit one obtains that, up to a constant,

$$\beta \sim s_0/(2\delta/\Gamma)^2. \tag{2.4}$$

Combining this dependence of $\beta$ upon the MOT parameters, with the one for $\langle V\rangle$ given by Eq. (2.3), one then expects the MOT atom number to feature a scaling of the kind

$$N_\infty \propto \frac{\sqrt{\Gamma_L}}{b^{3/4}}\frac{(\delta/\Gamma)^4}{s_0^{5/4}}. \tag{2.5}$$

From the overall trend of Eq. (2.5), one can see how, for a given loading rate $\Gamma_L$, light-assisted losses can be mitigated – thereby substantially increasing $N_\infty$ – by working at low $s_0$ values, large detunings, and weak field gradients of the MOT, although a compromise must be found, in order to guarantee a sufficiently strong force and high capture velocity of the MOT.

A well-known system, where very strong light-assisted losses are successfully circumvented by following these concepts, is metastable $^4$He* [83, 84]: in that case, operating the MOT at large detunings on the order of $|\delta| \sim 40\Gamma$ while keeping large $s_0 > 10$ values to maintain a sufficiently high capture velocity, it is possible to collect more than $10^9$ atoms within a few-second loading time. For the $^{53}$Cr system, this strategy is challenging to follow. On the one hand, the saturation intensity (linewidth) of chromium is more than 50 times (3 times) larger than the one of He*, and the limited amount of blue power available does not allow us to reach $s_0 \gg 1$, without diminishing the performance of transverse cooling and hyperfine pumping stages at the chromium oven [60], thus decreasing $\Gamma_L$. Moreover, contrary to metastable He, $^{53}$Cr features a rich and rather dense hyperfine spectrum which, in combination with large $s_0$ and $|\delta|/\Gamma$ values, may allow the cooling light to address undesired transitions. Indeed, the small optimum Zeeman slower detuning and low exit velocity shown in our previous work [60], was already interpreted as a strong sensitivity to residual Doppler shifts during the MOT capture. Hence, we opted to follow a strategy opposite to the one of $^4$He*, based on minimizing $s_0$ while keeping relatively small light detunings of a few $\Gamma$.

### $^{53}$Cr MOT: experimental results.

Experimentally, to test the feasibility of the strategy above discussed, we measured the atom number collected in the MOT after a 2 s loading time, exploring different (small) values of $s_0$. For each $s_0$ value, the light detuning was scanned until the maximum number was observed. The study was performed by intentionally keeping both $\Gamma_L$ and $b$ constant. Specifically, we worked at a field gradient $b$=25 G/cm along the vertical direction. In order to better count the collected atoms, at the end of the loading stage we performed a compressed MOT (C-MOT) stage lasting about

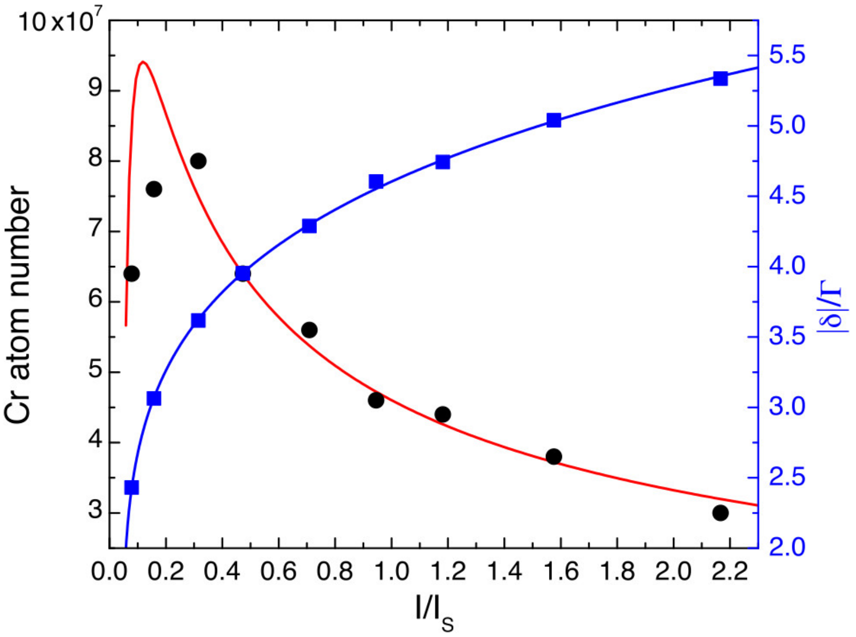

**Figure 2.3.** Characterization of the maximum chromium atom number collected in the MOT after 2 s loading, as a function of $I/I_S$ (black circles, left axis). $I = 2\times 2P/w^2$ is the peak intensity of one single (retro-reflected) MOT beam, characterized by a $1/e^2$ radius $w$=6.5 mm. Each data point is the average of at least five independent measurements. For each $I/I_S$, the experimental data exhibit a constant 10% uncertainty. For each value of $I/I_S$, the corresponding optimum detuning $|\delta|/\Gamma$, experimentally determined, is shown as blue squares, right axis. The blue line shows the best fit to a power law $|\delta|/\Gamma = (I/I_S)^\alpha$, see text. The red solid line corresponds, up to a multiplicative factor, to $N_\infty$ given by Eq. (2.5), assuming the best-fitted power-law dependence of $|\delta|/\Gamma$ on $(I/I_S)$.

6 ms, that strongly reduces the cloud size while not affecting the atom number. Then both MOT gradient and lights were turned off, and an absorption image was acquired after 2 ms time-of-flight, from which the atom number was obtained through a 2D-Gaussian fit.

The results of this characterization, reported also in Ref. [64] are summarized in Fig. 2.3. The atom number (black circles, left axis), is plotted as a function of the normalized single-beam peak intensity $I/I_S$, together with the corresponding optimum detuning experimentally identified (blue squares, right axis). One can notice how, throughout the scanned parameter space, a substantial increase in the collected Cr atoms could be observed, relative to our previous study [60], and samples ranging from 30 to 80 million particles were obtained. The behavior of $|\delta|/\Gamma$ versus $s_0$ is well fitted to a power-law, with exponent $\alpha = 0.22(1)$, see blue line. Such a value is relatively close to, but smaller than, the one that would maintain a constant $\beta/\langle V\rangle$ rate for light-assisted collisions in Eq. (2.5), i.e. $\alpha = 5/16 \sim 0.31$. On the other hand, a non-constant loss rate is signaled by the observed variation of the MOT atom number, see black circles in Fig. 2.3. Remarkably, the observed behavior is nicely reproduced by the textbook model expectation Eq. (2.5), shown as solid red line in Fig. 2.3, up to a multiplicative constant. The small mismatch between experiment and theory, visible at very low $s_0$ values, we ascribed to the fact that in this regime the estimated MOT capture velocity becomes very close to, or even slightly smaller than, the exit velocity of our Zeeman slower [60]. Parallel to that, the MOT size in this regime was found to rapidly increase approaching the beam radius, thus making finite-size effects more important.

The identification of a region of MOT parameters able to strongly mitigate light-assisted losses allowed us to greatly speed up and simplify the experimental routine to produce a large $^6$Li-$^{53}$Cr mixture in the cold regime. Since a loading time of 2 s suffices to reach $N_\infty$ for chromium, and that the MOT performances summarized in Fig. 2.3 are not affected by the presence of an overlapping lithium cloud, it is not anymore needed to pursue accumulation of Cr atoms in magnetically-trapped $D$ states [58], a procedure that requires significantly longer loading times, and whose efficiency is limited by the presence of a large Li MOT [60]. As a final remark, it is worth emphasizing that while the optimum loading conditions summarized in Fig. 2.3 strongly reduce the Cr MOT density, they do not limit the capture efficiency of the C-MOT stage, operated at constant cooling light parameters. As a consequence, the strong increase in the MOT atom number achieved during my thesis directly turns into a significant density increase after the C-MOT, hence providing a substantial gain for the successive step of optical trap loading within our experimental routine.

### Optimized loading of a dual species $^6$Li-$^{53}$Cr MOT.

The ability to rapidly collect a large number of $^{53}$Cr atoms directly in the MOT allowed for an optimized sequential loading of the Li-Cr mixture in our dual-species magneto-optical trap. The most convenient strategy we experimentally identified – and that represents our current experimental routine – is summarized in the following: (i) We first load lithium atoms for about 6 s, at an optimum gradient of about $b = 45\,\mathrm{G/cm}$ along the vertical direction. During this time, the chromium lights and ZS field are already on, although few Cr atoms are collected at this stage. (ii) We switch off the Li Zeeman slower and decrease the MOT gradient down to $b = 25\,\mathrm{G/cm}$, which is the optimum value found for chromium. The light detuning for lithium is correspondingly slightly diminished to ensure a good storage of this species during the chromium MOT loading. (iii) We operate the Cr MOT for about 2 seconds with the optimum light parameters reported in Fig. 2.3. (iv) We then turn off the Cr Zeeman slower (light and field), and adiabatically transfer the cold Li-Cr mixture from the quadrupole field of the MOT coils into that of a smaller set of "Feshbach" coils [60], yielding the same gradient but allowing for a faster switch off. (v) Finally, a 6 ms-long C-MOT phase is applied on both species simultaneously, in order to compress and cool the mixture. This is done, without changing the field gradient, by diminishing the intensity of the MOT lights, and moving the cooling frequency closer to resonance. Specifically, for chromium the C-MOT detuning is set to about -1.4 Γ and the beams intensity is reduced to about 20%, relative to that employed during the loading. For lithium, the detuning is moved from about -7 to -1.7 natural linewidths ($\Gamma_{Li}/(2\pi) = 5.87\,\mathrm{MHz}$), and the light intensity is substantially reduced, passing from more than $17\,I/I_{S,Li}$ at the loading stage, down to about $0.5\,I/I_{S,Li}$ ($I_{S,Li}$=$2.54\,\mathrm{mW/cm^2}$) [60].

At the end of this procedure, lasting 8 seconds overall, we manage to obtain cold Li-Cr mixtures comprising $10^9$ Li and $8\times10^7$ Cr atoms, at a temperature of about

300 µK.

## 2.2 Loading of $^{6}$Li-$^{53}$Cr mixtures into a BODT

As anticipated in the Introduction, our experimental strategy is based on an all-optical approach conceptually analogous to the one employed for Li-K mixtures [57]. As a crucial step, this requires an efficient loading of the cold Li-Cr mixture, delivered by our dual species MOT discussed in Sec. 2.1, into a high-power optical dipole trap. Also in this case a few factors make the Li-Cr system more challenging than the Li-K one. First, the chromium polarizability for standard infrared (IR) laser trapping lights at 1064 or 1070 nm is only about 30% of the lithium one, see red profiles in Fig. 2.4(a), making the resulting IR trap not suited to guarantee an efficient sympathetic cooling of Cr. Indeed, a 1070 nm beam, characterized by power $P_{IR}$ (expressed in Watt) and $1/e^2$ waist $w_{IR}$ (in micron), yields a maximum trap depth for lithium and chromium that, expressed in mK, are given by $U_{Li,IR} \sim -38.3 P_{IR}/w_{IR}^2$ and $U_{Cr,IR} \sim -12.7 P_{IR}/w_{IR}^2$, respectively.

We could mitigate this issue by superimposing a green beam at 532 nm to the IR trap. This second light is tightly confining for chromium, whereas it anti-confines lithium, see green profiles in Fig. 2.4(a). Denoting the power and waist of the green beam with $P_G$ and $w_G$, respectively, one finds in this case $U_{Li,G} \sim +39.2 P_G/w_G^2$ and $U_{Cr,G} \sim -23.5 P_G/w_G^2$. Therefore, by tuning the relative power of the two lights of this bichromatic optical dipole trap one can control the overall trap depth ratio for the two species, see black profiles in Fig. 2.4(a). Experimentally, the BODT is realized by overlapping our IR trap, already discussed in Ref. [77] and based on a multimode fiber laser module from IPG Photonics (YLR-300) delivering up to 300 W, with a high-power laser at 532 nm. For the latter, we employ a Sprout-G source by Lighthouse Photonics, nominally delivering up to 15 W. The two BODT beams, propagating in the horizontal $(x, y)$ plane, are recombined on a dichroic mirror and then focused onto the center of the Li-Cr MOT clouds, with waists along the vertical (horizontal) direction of $w_{IR,z}$=44 µm ($w_{IR,y}$=58 µm), and $w_{G,z}$=45 µm ($w_{G,y}$=48 µm), for the IR and green light, respectively.

A second technical problem of Li-Cr is that the direct loading of atoms from the MOT into the optical trap, contrarily to the lithium case, see e.g. Ref. [81], has been found to be challenging for chromium [61, 62, 85]. Besides increasing light-assisted losses owing to an increased density of the trapped cloud, the IR light shifts both $^{7}S_3$ and $^{7}P_4$ atomic levels – connected by the main cooling transition – to lower energy, with a shift for the excited state larger than the one of the ground state. Therefore, the detuning $|\delta|$ of the MOT light, experienced by Cr atoms within the IR trap, is effectively reduced (and it may eventually change sign). From light-shift measurements, that were performed by monitoring the resonance frequency of absorption imaging of a cold Cr cloud in presence of our IR beam, we obtained a trap-averaged shift of -0.021(2) MHz/W. This implies that the (C-)MOT detuning, felt by atoms within the IR trap with $P_{IR} \sim$200 W, is moved towards resonance by about $+1\Gamma$. It thus becomes almost impossible to simultaneously guarantee a good efficiency of the C-MOT stage for Cr atoms both in- and out-side the IR trap, especially given the inhomogeneous intensity distribution of the trapping beam.

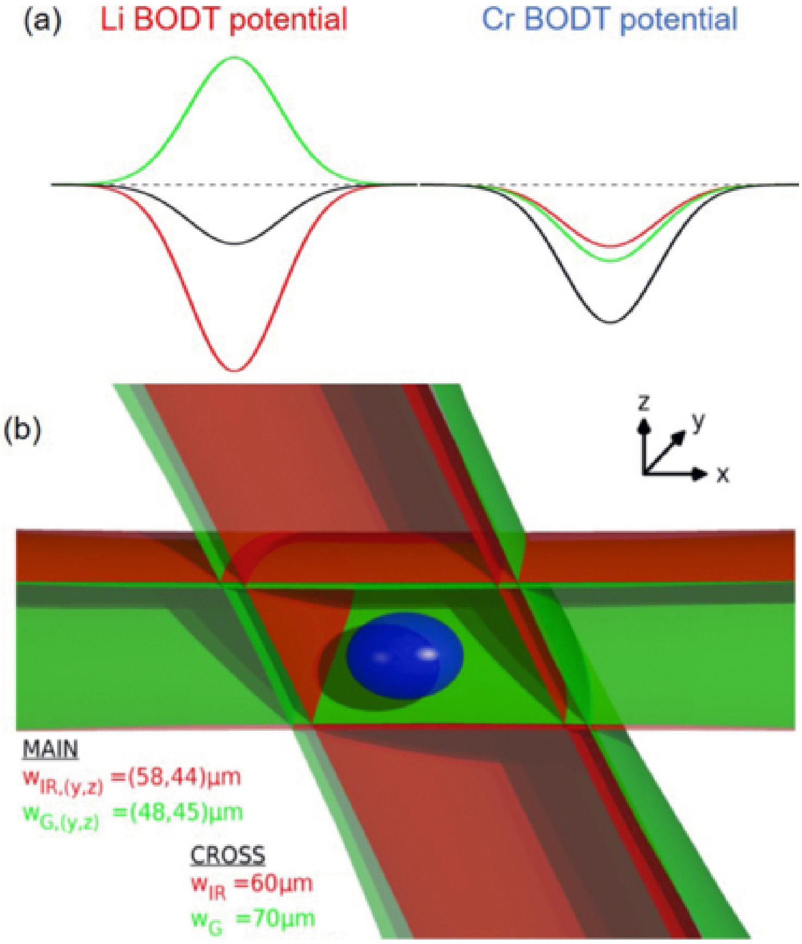

**Figure 2.4.** **(a)** Sketch of the optical potentials experienced by Li (left panel) and Cr (right panel) atoms confined in the BODT. The IR light (red curves) yields a trapping potential about 3.3 times deeper for Li than for Cr atoms, whereas the green beam (green curves) anti-confines lithium and tightly confines chromium, see text for details. By adjusting the parameters of the two beams, in the figures assumed to feature equal waists and an IR-to-green power ratio of 2, one can obtain an overall BODT potential (black curves) deeper for the Cr than for the Li component. **(b)** Schematic view of our BODT setup. Two overlapped IR and green beams, propagating in the horizontal plane along the $x$ direction, and featuring waists indicated in the figure, provide the primary trapping potential for the atomic mixture, sketched in blue. A secondary bichromatic trap, realized by two additional overlapped IR and green circular beams with waists of about 60 and 70 µm, respectively, crosses the main BODT at an angle of about 15° from the vertical direction. The crossed BODT beam, turned on at the end of the evaporation stage, allows us to tune the densities of the two mixture components independently while not modifying the trap depth, see Sec. 2.4.

One way to circumvent this problem is to flash the IR trap only once the MOT light is turned off. Experimental trials in this direction, given our large MOT atom number and the high IR power at our disposal, allowed us to capture about $10^6$ $^{53}$Cr atoms within the IR beam at typical power of 130 W. Yet, this non-adiabatic loading method was found to considerably heat up the sample, and it is far from being optimum also for the lithium component. More involved loading schemes, alternative to the instantaneous flash of the IR trap, have been devised in Refs. [61, 62, 85], which rely on the accumulation of metastable $D$-state atoms in a combined magnetic and optical potential.

In our case, we found a convenient way, offered by our BODT setup, to successfully overcome this major technical issue. The key point is that the 532 nm light dramatically perturbs the cooling transition, owing to the presence of three atomic lines that connect the $^7P_4$ level to the $^7D$ states, see Fig. 2.2, all centered around 533 nm and featuring linewidths ranging from 0.9 to about 10 MHz. A relatively weak laser field near 532 nm, blue-detuned from these lines by less than one nanometer, thus suffices to strongly shift the $^7S_3 \rightarrow {}^7P_4$ transition towards higher frequencies. Contrarily to the IR case discussed above, this implies that the effective detuning of the MOT light experienced by atoms within a 532 nm beam is strongly moved out of resonance. The green light of our BODT can thus be efficiently exploited to (over-)compensate the detrimental effect of the IR main beam on the Cr C-MOT, realizing an effective "dark spot".

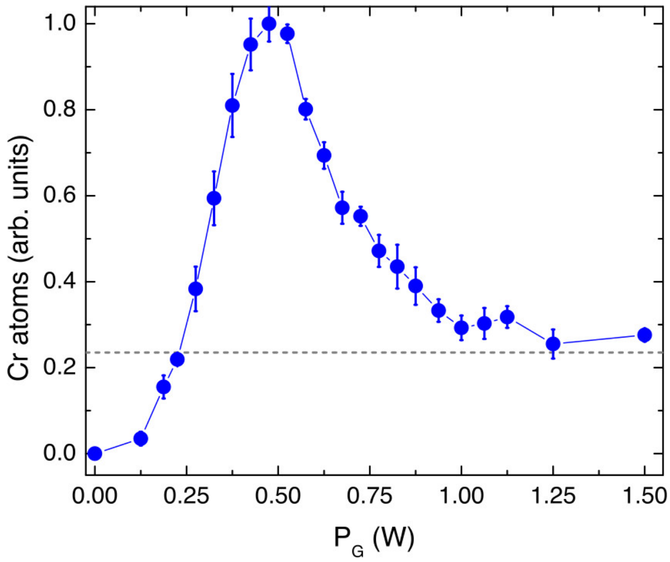

**Figure 2.5.** Characterization of the chromium atom number collected in the BODT directly from the C-MOT, as a function of the green beam power acting as a "dark spot". The Cr population (blue circles), recorded in the BODT after a hold time of 100 ms through absorption imaging that follows a time-of-flight expansion of 200 µs, is normalized to the maximum value found throughout the scan, centered at 0.47(1) W. Each point corresponds to the average value of at least four independent measurements. Error bars represent the standard deviation of the mean. Horizontal dashed line marks the value obtained by instantaneously flashing the IR trap at the end of the C-MOT stage. For this data set, the IR beam has a fixed power of 130 W, and the parameters of the C-MOT stage are kept constant to their optimum values, obtained in the absence of the BODT. The Sprout-G module used to realize the "dark spot" has a wavelength of 532.2 nm.

We tested the feasibility of this loading strategy by rising the IR beam up to 130 W and, simultaneously, the green beam to a variable power level, through a 3 ms-long linear ramp that started 1 ms before the chromium C-MOT stage. The laser cooling light parameters were kept fixed to the optimum values experimentally found in the absence of the optical trapping potential. 5 ms after the end of the BODT ramp, both MOT lights and gradient were switched off. By turning off the cooling light 20 µs before the repumper ones we made sure that the Cr component was in the $F_S = 9/2$ hyperfine ground-state. After an additional hold time of 100 ms, we turned off the BODT and recorded, through an absorption image following a time-of-flight expansion, the number of Cr atoms collected in the trap.

The result of this characterization is summarized in Fig. 2.5, that shows the chromium number loaded into the optical trap, normalized to its maximum value, as a function of the power of the green light (blue circles). One can notice how, without the green beam being applied, almost no atoms could be collected in the IR potential. By increasing the power of the 532 nm light, instead, we observed a sharp enhancement of the atom number which, for our specific BODT beam parameters, reaches its maximum at $P_G$=0.47(1) W. A further increase of the green beam power beyond this optimum value progressively diminished the Cr atom number. For $P_G \geq$1.25 W, this was found to approach the value obtained by instantaneously flashing the IR trap right at the end of the C-MOT stage, marked by the horizontal gray line in Fig. 2.5. This behavior can be understood by considering that, once the green light reaches this power level, atoms falling within the BODT volume are effectively transparent to the C-MOT light, and thus completely unaffected by it.

Owing to the strong inhomogeneity of the light shift experienced by the Cr C-MOT atoms throughout the BODT region at the loading, it was hard to quantify the actual light shifts based on the method employed to characterize the IR beam at high temperature. Measurements performed in the ultracold regime, where the Cr sample is localized near the center of the green laser, yielded a peak shift of +38(5) MHz/W, characterized by a (positive) slope almost 2000 times larger than the IR (negative) one [80]. Correspondingly, at the optimum value shown in Fig. 2.5, atoms residing at the center of the green beam experience an effective red shift of the cooling light of about -3.6 Γ.

Not aiming at a quantitatively accurate description of the observed loading dynamics – which can be quite involved – I remark here only a few qualitative and general experimental facts. First, throughout the power range explored in Fig. 2.5, the green beam had negligible impact on the total trap depth, which was solely set by the high-power IR beam. Second, depending on the specific laser source employed for realizing the green BODT beam, the optimum power may quantitatively move to higher or lower values, but the qualitative trend would remain unaffected, as long as the wavelength of the green light remains close to, but shorter than, 532.9 nm. Third and most importantly, application of such a scheme allowed us to substantially enhance the optical trapping efficiency, compared to the instantaneous flash of the IR beam. Indeed, this "dark spot" strategy, currently employed in our everyday routine, yields more than a four-fold improvement in the BODT atom number, and it does not cause any detectable excitation nor heating of the atomic sample. Under optimum conditions, such a protocol allows us to store up to $4 \times 10^6$ Cr atoms in the optical trap, at temperatures of about 250 µK, slightly lower than the typical

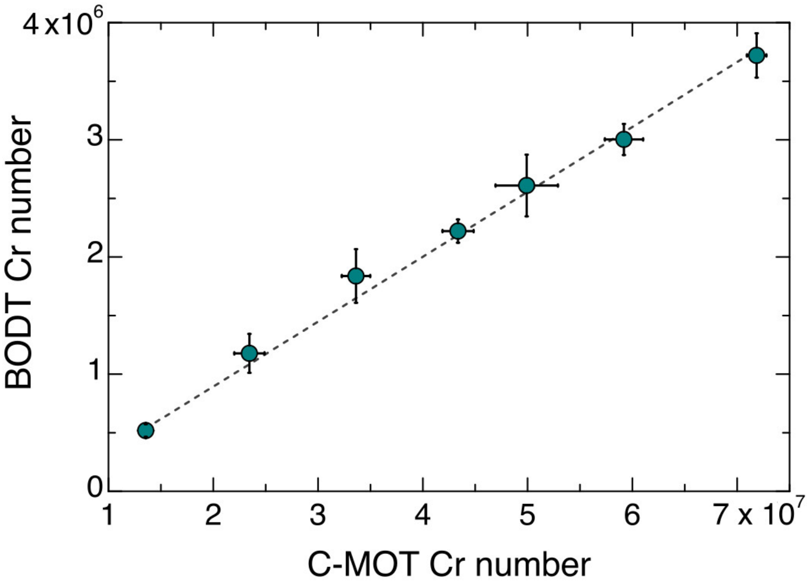

**Figure 2.6.** Dependence of the number of chromium atoms collected in the BODT upon the C-MOT atom number. The latter is adjusted by reducing the MOT loading time while not varying the MOT parameters. The IR beam is set to a power of 130 W, and the green light is adjusted to the optimum value shown in Fig. 2.5. Data are recorded, after a hold time of 100 ms in the BODT, through absorption imaging that follows a time-of-flight expansion of 200 µs. Each point corresponds to the average value of at least four independent measurements of both C-MOT and BODT numbers. Horizontal and vertical error bars represent the standard deviation of the mean. A linear fit to the data, see dashed line, yields an overall MOT-to-BODT transfer efficiency of 5.5(2)%.

C-MOT one. Finally, it is also important to stress that the absolute number of atoms that can be transferred into the BODT from the MOT following this procedure was found to scale linearly with the MOT atom number itself, as shown in Fig. 2.6: up to the largest MOT clouds we could produce, we did not observe any saturation effect on the optically-trapped samples, with a constant 5.5% MOT-to-BODT transfer efficiency. This observation demonstrates how the “dark-spot” method indeed allows us to maintain light-assisted losses negligible up to the highest achievable densities, thereby making the ODT loading dynamics of chromium as simple as the one of lithium and other alkalis.

Besides enabling to collect a significant amount of $^{53}$Cr atoms, which may be appealing also for single-species setups dealing with cold (fermionic or bosonic) chromium, the successful implementation of this direct loading method is especially advantageous in our mixture experiment. Indeed, the presence of the weak green laser field is essentially irrelevant for the loading of the lithium component: up to $2{\times}10^7$ $^6$Li atoms, with temperatures of about 280 µK are stored in the BODT when the IR trap power is set to 130 W, with transfer efficiencies similar to those reported in Ref. [81] for the single species case.

Since the two species feature similar temperatures, the simultaneous loading of the Li-Cr mixture in the BODT does not perturb too strongly the chromium performance, although the initial trap depth ratio, uniquely set by the IR beam, yields at 130 W $U_{Li,IR}$ ~1.9 mK and $U_{Cr,IR}$ ~0.65 mK, thus causing a rather strong asymmetry in the temperature-to-trap-depth ratio between the two components. In fact, while $\eta_{Li} = U_{Li,IR}/k_B T_{Li} \sim 7$, for chromium we obtain $\eta_{Cr} = U_{Cr,IR}/k_B T_{Cr} \sim 3$. For this reason, the chromium BODT population, after a hold time of 100 ms, in presence of the overlapping Li sample, is typically found to drop by almost a factor of 3. This effect was partly reduced by applying a 350 µs-long $D_1$ molasses phase on lithium within the BODT [81], about 3 ms after the end of the C-MOT stage, once the magnetic field quadrupole gradient has been zeroed. This allows us to reduce the lithium temperature, although not substantially, from 300 down to approximately 220 µK, a value slightly lower than the chromium one. At the end of the $D_1$ cooling, a 20 µs-long hyperfine pumping pulse is applied [81], which transfers all lithium atoms into the $F = 1/2$ ground-state manifold. Finally, within 20 ms the green power is linearly ramped up to its maximum value, corresponding to a net power of 6 W onto the atoms, leading to about a 10% increase (6% decrease) of the chromium (lithium) trap depth.

The application of the BODT loading method for $^{53}$Cr discussed above, and its integration within the two-species experimental cycle, allows us to store in our optical trap cold Li-Cr mixtures at about 250 µK, composed by $2\times10^7$ $^6$Li atoms populating the two lowest Zeeman states $m_F = \pm 1/2$ of the $F = 1/2$ manifold, coexisting with about $2\times10^6$ $^{53}$Cr atoms, asymmetrically distributed among the four lowest-lying Zeeman state of the $F = 9/2$ hyperfine level. Specifically, without performing any Zeeman-selective optical pumping stage, about 55% of the Cr sample are typically found in the lowest Zeeman state, $m_F = -9/2$. The remaining Cr atoms are distributed among the three higher-lying levels, $m_F = -7/2$, $-5/2$ and $-3/2$, with relative populations of 25%, 13% and 7%, respectively. This represents the starting point for the successive stages of evaporative and sympathetic cooling, that I describe in the following section. For convenience, in the following I denote the different Zeeman levels of both species with Li$|i\rangle$ and Cr$|i\rangle$ respectively, with $i = 1, 2, ...$ labelling the atomic state starting from the lowest-energy one.

## 2.3 Evaporative and sympathetic cooling stages

Once the two species have been loaded into the BODT, while the green BODT beam is ramped up to its maximum value, with a linear ramp of 5 ms. Parallel to this, we also found it convenient to linearly increase, within 55 ms, the magnetic field bias up to 880 G, *i.e.* about 50 G above the broad Feshbach resonance occurring between the two lowest Zeeman states of lithium, Li$|1\rangle$-Li$|2\rangle$. At this field [7], intra-species lithium collisions are unitarity-limited at all temperatures relevant for this thesis, whereas inter-species Li-Cr collisions are at their background level, characterized by a scattering length $a_{bg} \sim 42\ a_0$ determined by our team in Ref. [48] prior to the start of my thesis. The magnetic-field curvature of our coils provides an additional in-plane harmonic confinement, characterized at 880 G by a lithium (chromium) frequency of about 8.5 Hz (7.0 Hz), which adds to the BODT potential. The initial trap depth ratio between the two components, $U_{Li}/U_{Cr} \sim 3$, and the low initial value of $\eta_{Cr} \sim 3$, are not optimal for an efficient storage of chromium atoms in the presence of the lithium sample. For this reason, we found it experimentally convenient to start the evaporation immediately after the green beam was upraised.

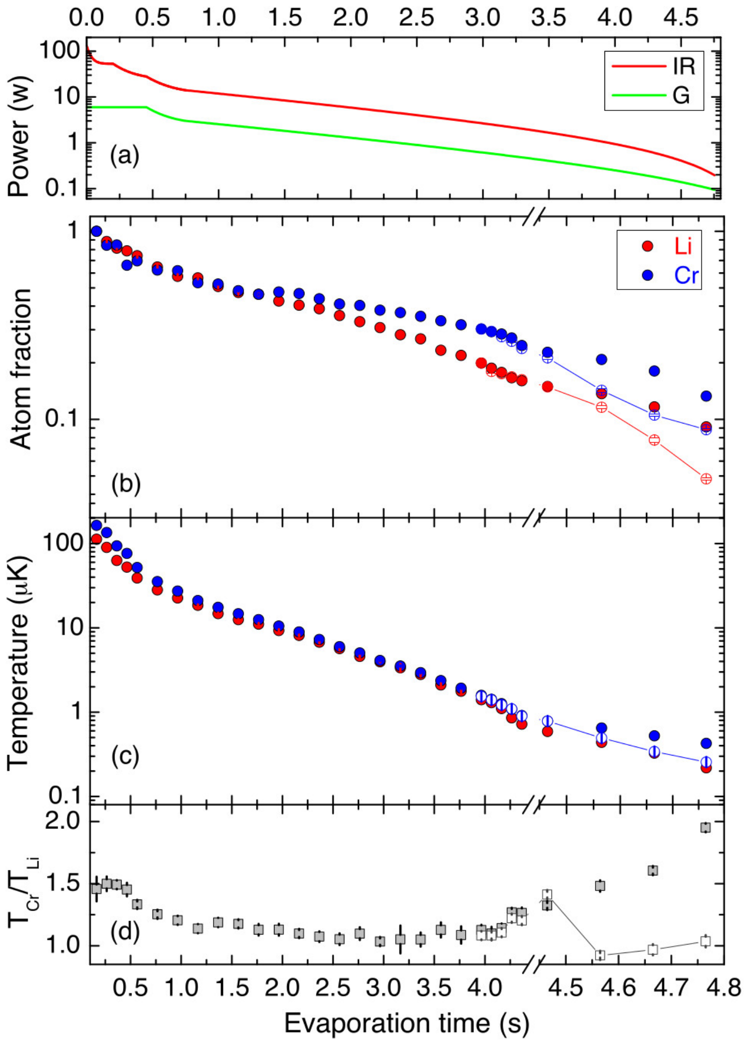

**Figure 2.7.** **(a)** Evolution of the IR and green BODT powers during the evaporation ramp. The IR power is reduced through four consecutive exponential ramps, lasting 0.2, 0.25, 0.3 and 4 s, respectively, and characterized by $1/e$ decay times $\tau_1$=30 ms, $\tau_2$=125 ms, $\tau_3$=150 ms, and $\tau_4$=1.6 s. The green power is decreased through two consecutive ramps, simultaneous to the last two IR ones, and featuring same durations and decay times. **(b)** Evolution of the Li$|1\rangle$ (red circles) and Cr$|1\rangle$ (blue circles) atom number during the evaporation ramp. Both datasets are normalized to the atom numbers recorded after the first 165 ms of evaporation, where $N_{Li|1\rangle}$=5.1(1)× $10^6$ and $N_{Cr|1\rangle}$=1.05(3)×$10^6$. Empty symbols refer to the number evolution when the "Feshbach cooling" stage is applied, see text. **(c)** Same as panel (b) but for Li and Cr temperatures. For both (b) and (c) panels, numbers and temperatures are obtained from Gaussian fits to the atomic distributions, imaged after variable time-of-flight expansion. Note that, for the coldest samples, the temperature extracted from the Gaussian fit overestimates the real one, owing to Fermi degeneracy, up to about 40%. Each data is the average of at least three independent measurements. Empty symbols refer to the temperature evolution when the "Feshbach cooling" stage is applied. **(d)** Ratio between chromium and lithium temperatures, without (full squares) and with (empty squares) application of the "Feshbach cooling" stage.

The evaporative cooling stage that we experimentally optimized during the first period of my thesis, overall lasting for about 5 s, is performed by decreasing the power of the BODT beams – hence the trap depth – through a series of exponential ramps. These are schematically shown in Fig. 2.7(a) for the IR and green lights, respectively. Figs. 2.7(b) and (c) show the corresponding evolution of the normalized atom number and temperature, that we experimentally determined, for the Li$|1\rangle$ (red circles) and Cr$|1\rangle$ (blue circles) component, respectively. These observables were extracted from Gaussian fits to the density distributions of the two atomic clouds, monitored via spin-selective absorption imaging following time-of-flight expansion. The Li$|2\rangle$ component, not shown in the Figure, throughout the evaporation stage was found at a temperature equal to the one of Li$|1\rangle$, and the corresponding atom number, relative to that of Li$|1\rangle$, remained roughly constant at a value $N_{Li|2\rangle}/N_{Li|1\rangle}$=0.71(5). Additionally, Fig. 2.7(d) displays the ratio between the chromium and lithium temperatures throughout the evaporation stage.

During the first 400 ms of the optimized BODT-ramp, evaporative cooling of lithium is established by decreasing only the IR beam power, from 130 W down to 28 W. This first step, sufficiently slow to allow for intra-species thermalization of lithium, is somewhat too fast for the chromium component, the temperature of which is found to be about 50% higher than the lithium one, see Fig. 2.7(d). Despite the rather poor efficiency of sympathetic cooling observed within this initial stage, such a ramp allows us to rapidly diminish the $U_{Li}/U_{Cr}$ ratio, from the initial value of 3, down to about 1. In order to maintain the chromium cloud well overlapped to the lithium one at all times, we also found it convenient to minimize the differential gravitational sag of the two components by applying a magnetic-field gradient $b$ along the vertical direction to counterbalance the gravitational force. Experimentally, we found an optimum value of about 1.6 G/cm, which corresponds to an almost perfect levitation of the chromium component, and to an effective weak "anti-gravity" for lithium, of about -$g/2$.

For evaporation times longer than 0.5 seconds, where $U_{Li}/U_{Cr}\sim$1, the observed trajectories signal a good inter-species thermalization and a satisfactory sympathetic cooling. The observed decrease in atom number is indeed significantly smaller for the Cr than for the Li component (see Fig. 2.7(b)), while the chromium temperature closely follows the lithium one with less than 15% mismatch, see Fig. 2.7(c) and (d), up to about 4 s. Here, we typically obtain about $3\times10^5$ Cr$|1\rangle$ atoms at $T_{Cr}\sim$1.5 µK, coexisting with about $1.1\times10^6$ Li$|1\rangle$ and $7.5\times10^5$ Li$|2\rangle$ atoms at $T_{Li}\sim$1.35 µK, close to the onset of quantum degeneracy for both lithium components. By further decreasing the BODT trap depth following our optimized trajectories shown in Fig. 2.7(a), we observe a progressive increase of $T_{Cr}/T_{Li}$, see Fig. 2.7(d). A convenient way to circumvent such a limited inter-species thermalization is offered by the presence of various $s$-wave Li-Cr Feshbach resonances, located at fields above 1400 G and experimentally discovered before the start of my thesis [48]. In particular, the Li$|1\rangle$-Cr$|1\rangle$ mixture possesses a ∼0.5 G-wide FR at 1414 G, and the Li$|2\rangle$-Cr$|1\rangle$ combination exhibits a resonance of similar character around 1461 G. Both features are immune to two-body losses [48] and, in spite of their relatively narrow character, allow us to magnetically control the Li-Cr scattering length $a$, and thus to increase the Li-Cr elastic scattering cross section well above its background value.

In order to exploit such a possibility, about 1.5 s after the start of the evaporation stage, we linearly ramp the magnetic field from 880 G, up to 2 G above the center of one of either resonances. There, the Li-Cr scattering length is not significantly different from its background value, $a \sim a_{bg}$, and also the intra-species Li$|1\rangle$-Li$|2\rangle$ scattering length approaches its large and negative background value, of about -2500 $a_0$ [86]. About 4 s after the start of the evaporation, we then reduced the magnetic-field detuning to $\lesssim$100 mG from the resonance center, correspondingly tuning the Li-Cr scattering length to $a \lesssim$-200 $a_0$, yet not causing a significant enhancement of inter-species three-body losses. A detailed characterization of such a "Feshbach cooling" mechanism near a narrow resonance will be subject of a future study. The empty symbols in Fig. 2.7(b)-(d) panels highlight the impact of the Feshbach cooling mechanism on the final part of the evaporation ramps. One can see how, for fixed BODT power ramps, an increased Li-Cr scattering rate negligibly affects the Li temperature, whereas it causes a strong decrease of the Cr one, allowing for a perfect cancelation of the relative temperature mismatch, see empty squares in Fig. 2.7(d). The much quicker inter-species thermalization was found to be accompanied by a more sizable atom loss of both species, see blue (red) empty circles in Fig. 2.7(b) for the Cr (Li) component. Yet, this only moderately decreases the degree of degeneracy of lithium, while for chromium the atom loss was outweighed by the strong temperature reduction, resulting in a substantial increase in the Cr phase-space density.

By following this protocol, overall lasting less than 5 s, we can experimentally realize degenerate Li-Cr Fermi mixtures, comprising up to $3.5\times10^5$ Li$|1\rangle$ and $2.5\times10^5$ Li$|2\rangle$ atoms at $T/T_{F,Li} \sim$0.25, coexisting with about $10^5$ Cr$|1\rangle$ atoms at $T/T_{F,Cr} \sim$0.5. The corresponding degree of degeneracy $T/T_{F,i}$ was obtained by fitting time-of-flight images to finite-temperature Fermi-Dirac distributions. For both species, the extracted reduced temperatures were found to be compatible with the value estimated on the basis of the measured atom number and trap frequencies ($\nu_x$, $\nu_y$, $\nu_z$) – within a 20% uncertainty equal to (16, 115, 156) Hz and (13, 124, 118) Hz for Li and Cr, respectively – and given the temperature $T=$ 130(20) nK, obtained by fitting the low-density wings of the atomic density distributions. I also remark that at the end of the evaporation the populations of the additional chromium minority components Cr$|i > 1\rangle$, initially loaded within the BODT, were found to be negligible, owing to the combined effect of inelastic two-body losses occurring throughout the evaporation ramp, and to the lack of thermalization with lithium, given the spin-selective character of the "Feshbach cooling" mechanism.

The evaporation trajectories summarized in Fig. 2.7(a) and currently used in our experimental cycle, can be also adapted to produce single-species samples of either species. For lithium, this is straightforward: without loading the chromium component, the same BODT power ramps discussed above yield crossover superfluids of more than $4.5\times10^5$ pairs, when the bias field is tuned towards the pole of the broad intra-species Feshbach resonance at 832 G. This number can be further increased up to about $6\times10^5$ when the same time evolution of the trap depth is realized by means of the sole IR light of the BODT, resulting in performances similar to, and even slightly better than, those reported in Ref. [81].

To realize polarized Fermi gases of $^{53}$Cr, the protocols above discussed can be modified only partially, owing to the fact that quantum degeneracy of this species relies in our setup on sympathetic cooling with lithium. Yet, a slight increase

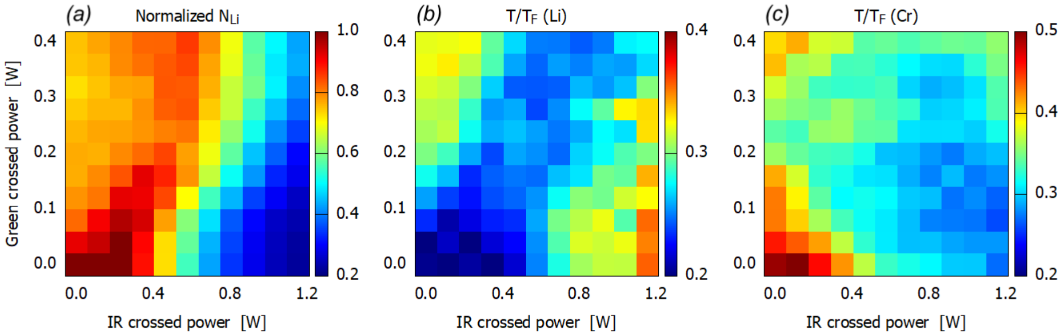

**Figure 2.8.** **(a)** Lithium atom number, normalized to its value measured in the sole main BODT at the end of the evaporation ramp, as a function of green and IR powers of the crossed BODT. **(b)** Normalized lithium temperature, $T/T_{F,Li}$, monitored as a function of green and IR powers of the crossed BODT. The degree of degeneracy is obtained as the average value extracted from fitting at least four independent Li images, acquired at 3 ms time-of-flight. **(c)** Same as in panel (b) for the reduced chromium temperature $T/T_{F,Cr}$. For chromium, a 4.6 ms time-of-flight expansion was employed.

of the green-to-IR power ratio during the evaporation allows us to obtain about 70% larger Cr samples at 220(20) nK, at the expense of a significant reduction of both Li components, which can be eventually completely removed at the end of the evaporation stage by further increasing the power of the green BODT arm. Sympathetic cooling of $^{53}$Cr with $^{6}$Li thus appears as a promising route to realize large Fermi gases of this yet poorly explored atomic species, so far produced only in combination with its most abundant bosonic isotope $^{52}$Cr [59]. In fact, the possibility to exploit the different Li and Cr polarizabilities to the IR and green lights of our BODT, absent when isotopic Cr mixtures are considered, together with our substantially larger Cr MOT, allows for an almost 200 fold increase in the $^{53}$Cr atom number that can be brought to $T/T_{F,Cr} \lesssim 1$, relative to previous studies [59].

## 2.4 Increasing quantum degeneracy in a crossed BODT

As discussed in the previous section, the degree of degeneracy, obtained at the end of the evaporation stage discussed therein, is quite different for the two mixture components, with lithium being highly degenerate while chromium featuring $T/T_{F,Cr} \sim 0.5$. By further decreasing the BODT trap depth, we never observed any substantial gain in phase-space density, a reduced temperature being counterbalanced by a drop in the atomic densities for both species.

To overcome this problem, once the evaporation stage is ended, we found it convenient to raise a second bichromatic trapping beam, which crosses the main BODT at an angle of about 15° from the vertical direction, see Fig. 2.4. Such a secondary beam has been obtained by exploiting the same laser sources, recycling part of the IR and green powers of the main BODT, damped at the end of the evaporation procedure. Both IR and Green crossed beams are almost circular, and at the atom position they feature waists of about 60 µm and 70 µm, respectively. Being oriented almost vertically, such a second bichromatic beam does not modify the overall trap depth experienced by the two atomic components, and hence their temperature, whereas it allows us to control the confinement – and thus the density and Fermi energy – of each cloud almost independently.

In order to test this possibility, once the evaporation ramp was performed, we raised up the crossed BODT at various IR and green power levels through a 50 ms linear ramp. After about 50 ms, we then recorded time-of-flight images of both Li$|1\rangle$ and Cr$|1\rangle$, and obtained the corresponding atom number and degree of degeneracy by fitting the atomic clouds to a finite-temperature Fermi-Dirac distribution. We checked that the employed timings, although not exceeding the typical axial ones in the sole main BODT trap, do not cause any detectable excitation nor trigger subsequent dynamics of the Li and Cr clouds. Exploitation of much longer ramp/hold times resulted instead in a poorer collection efficiency of the lithium component within the crossing region. The results of this characterization are summarized in the contour plots in Fig. 2.8: panels (a) and (c) show the chromium and lithium normalized temperatures $T/T_{F,Cr}$ and $T/T_{F,Li}$, respectively, as a function of green and IR powers of the crossed beam. Fig. 2.8(b) presents the corresponding trend for the Li$|1\rangle$ atom number, normalized to $3.5{\times}10^5$, which is the value obtained without application of the crossed beam. The chromium component, characterized by an axial size in the main BODT roughly two times smaller than the lithium one, was found to be efficiently transferred into the crossed trap at all green and IR powers that we explored, resulting in a Cr number, not shown in Fig. 2.8, that varies less than 15% throughout the investigated parameter space.

One can notice the qualitatively different response of the two mixture components to the crossed BODT. On the one hand, for chromium, application of either crossed beam leads to a substantial increase in the degree of degeneracy: as shown in Fig. 2.8(c), we found several IR and green combinations that could yield a two-fold decrease of $T/T_{F,Cr}$, passing from about 0.5 down to 0.25, solely caused by the large Cr density increase within the crossed trap. On the other hand, for lithium, application of one single (IR or green) crossed beam caused a decrease of the atom number, see Fig. 2.8(a), accompanied by a reduction of the degree of degeneracy, see Fig. 2.8(b). The response to the IR trap can be explained by the initially larger cloud size and mean energy-to-trap depth ratio of this atomic component, compared to the Cr ones. These factors imply a limited collection efficiency and a progressively increased anharmonicity of the experienced potential, which lead to a reduction of local density and degree of degeneracy. The response to the green crossed trap can instead be explained by the anti-confining effect on the Li species: even for low green powers, the atom number reduction is accompanied by a drop of local density within the crossing region, and hence of Fermi degeneracy.

However, when both IR and green lights are applied, over a quite wide range of parameters we observe an efficient storage of lithium atoms in the crossed BODT, at an almost constant $T/T_{F,Li}$, see Fig. 2.8(b). As expected, this occurs roughly around the diagonal of Figs. 2.8(a) and (b), where the anti-confinement of the green beam is (more than) counterbalanced by the IR light, and where anharmonicities of the experienced potential – estimated through trap frequency measurements – appear to be negligible. These observations highlight how the implementation of the crossed BODT allowed us to significantly enhance the parameter space which can be explored with the Li-Cr mixture in our setup: by simply tuning the (absolute

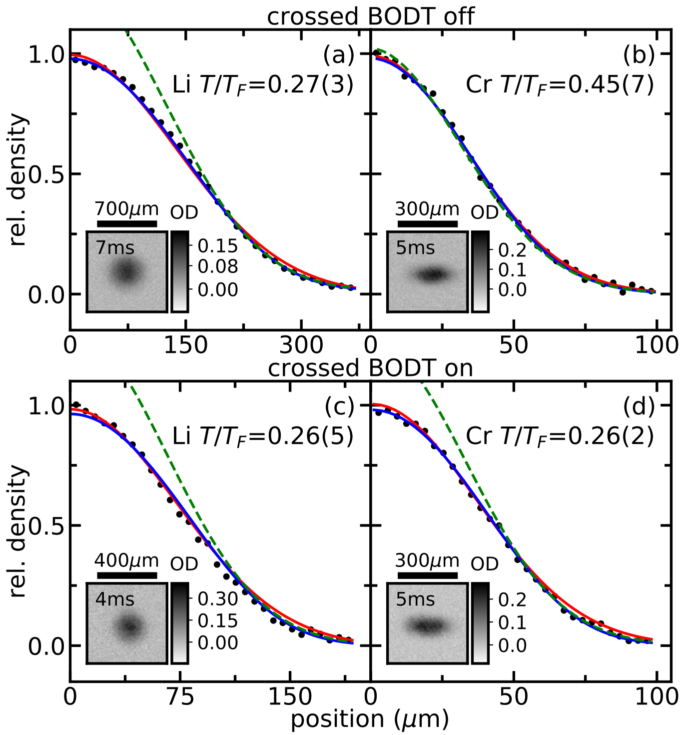

**Figure 2.9.** Axially-integrated density profiles (black circles) of a lithium (panel **(a)**) and chromium (panel **(b)**) Fermi gas, simultaneously prepared into the main BODT trap only. Profiles are obtained from the average of about 20 independent absorption images, acquired after time-of-flight expansion and shown as insets. Experimental data are compared with best fits to a Fermi-Dirac (blue line) and a Gaussian (red line) distribution. A Gaussian fit to the low-density tails of the density distributions (green line) accurately captures the atom temperatures whereas it overestimates the central density of highly-degenerate samples. For each component, the reduced temperature $T/T_F$ obtained from the former fit, together with the fit uncertainty, is specified in the panel. Panels **(c)** and **(d)** show the same as (a) and (b), but for a Li-Cr mixture released from a crossed BODT with IR and green powers set to 0.81 W and 0.20 W, respectively. Application of such crossed BODT does not alter the lithium degree of degeneracy, whereas it allows to strongly reduce $T/T_{F,Cr}$, and to obtain Li-Cr mixtures with both components at one fourth of their Fermi temperature.

and relative) powers of the two crossed lights, one can pass from the regime where lithium is highly degenerate and chromium is an almost thermal gas, to the opposite one.

Most importantly, over a sizable range of parameters we could simultaneously achieve a high degree of degeneracy for both $^6$Li and $^{53}$Cr components. As an example, in Figure 2.9 I show axially-integrated density profiles (black circles) of lithium and chromium Fermi gases, obtained from absorption images, see insets, acquired after time-of-flight expansion from the sole main BODT trap (panels (a) and (b)), and from a crossed BODT (panels (c) and (d)). Data are compared with best fits to a Gaussian and to a Fermi-Dirac distribution function, shown in red and blue, respectively. In both configurations, the lithium sample exhibits a roughly constant and low $T/T_{F,Li}$ value, see panels (a) and (c) in Fig. 2.9, and a corresponding constant peak density of about $1{\times}10^{12}$ cm$^{-3}$. For the chromium component, application of the crossed beam negligibly affects the gas temperature and the atom number, constantly about $1.0\times10^5$, while it strongly modifies the peak density, which increases from slightly less than $2\times10^{12}$ cm$^{-3}$ in the sole main BODT, to about $4\times10^{12}$ cm$^{-3}$ within the crossed trap. Correspondingly, the chromium degree of degeneracy is substantially improved, with the initial $T/T_{F,Cr}$=0.45(7) being lowered down to 0.26(2), see Figs. 2.9(b) and (d).

In conclusion, the experimental procedures described in this Chapter, and that I contributed to optimize during the initial period of my thesis, represent the starting point for all experiments performed with Li-Cr Fermi mixtures in the regime of strong interactions, that I discuss in the following Chapter.

# Chapter 3

# Resonantly interacting mixtures: Feshbach dimer formation, and new technical challenges.

As anticipated in the Introduction, one of the major motivation to create Fermi mixtures of lithium and chromium atoms is in the novel few- and many-body physics that this system may allow us to explore, in the regime of strong interspecies interactions. Since extensive Feshbach spectroscopy studies on Li-Cr were already performed prior to the start of my thesis, and that these enabled our team to build an accurate coupled-channel collisional model for this novel system [48], the natural step, following the production of degenerate Fermi mixtures discussed in the previous Chapter, was to explore the properties of such an ultracold system in the regime of strong interactions, accessible near a Li-Cr $s$-wave resonance. Among various possibilities to characterize the resonant regime, we have chosen to first focus our efforts in the production of ultracold Feshbach LiCr dimers from the bi-atomic mixture, and to investigate their properties: atom-to-molecule conversion efficiency and magnetic moment.

In this Chapter, I will first provide a succinct overview of the scattering properties and Feshbach resonances featured by the Li-Cr mixture, summarizing the results detailed in Ref. [48]. Second, I will briefly recall a few experimental schemes that are typically employed to form and probe ultracold dimers near a FR. Finally, I will show preliminary results on Feshbach dimers and discuss how these provided us evidence for a high atom-to-molecule conversion efficiency yielding more than 50k LiCr dimers, but, at the same time, how our data unveiled a few technical limitations, which needed to be overcome.

## 3.1 Overview of FRs and scattering properties of Li-Cr

In the following, I will provide a brief overview of the scattering properties of $^{6}$Li-$^{53}$Cr Fermi mixtures which were recently characterized [48] – prior to the start of my thesis – in a joint effort between our team – that performed extensive loss-spectroscopy measurements – and the theorist Prof. A. Simoni (Univ. Rennes), who could build, starting from experimental data, a full coupled-channel (CC) model for our Li-Cr system.

Experimentally, six different Li$|i\rangle$-Cr$|j\rangle$ spin-state combinations were investigated, with $i = 1, 2$ and $j = 1, 2, 3$, each being characterized by the total spin projection quantum number, $M_f = m_{f,Li} + m_{f,Cr} = -i + j - 4$, thus spanning $-5 \leq M_f \leq -2$. By scanning the magnetic field from 0 up to about 1500 G, more than 50 interspecies FRs could be pinpointed through loss spectroscopy. The observed features are arranged in complex but *non-chaotic* patterns and show qualitatively distinct features for $B$-fields below and above 150 G. While few, sparse and narrow resonances characterize the $B \geq 150$ G high-field region, more complex patterns were found at lower fields, with strong loss peaks often arranged in doublet or triplet structures, see Fig. 3.1, taken from Ref. [48].

This suggested that narrow and isolated $s$-wave features only occur in the high-field region, while the low-field spectra originate from strong FRs occurring in $l > 0$ partial waves – split by magnetic dipole-dipole interaction [87, 88] and possibly other couplings [89] – as also supported by their sensitive dependence upon the system temperature [48]. This intuition was indeed confirmed by the theoretical analysis carried out by A. Simoni based on full CC calculations, which account for: (i) the atomic hyperfine and Zeeman energies [90, 91], defining the asymptotic collision thresholds; (ii) The strong and isotropic electrostatic interaction – both $l$ and $M_f$ conserving – represented by the *sextet* $X^6\Sigma^+$ and *octet* $a^8\Sigma^+$ potentials, parametrized by *sextet* $a_6$ and *octet* $a_8$ $s$-wave scattering lengths, respectively, as well as the dispersion coefficients $C_6$ and $C_8$; (iii) Weaker anisotropic couplings, originating from both long-range magnetic spin and short-range second-order spin-orbit interactions. These can couple different partial waves and hyperfine states with different $M_f$ or $l$, provided that $\Delta l = 0, \pm 2$ and $M_f + m_l$ is conserved, $m_l$ being the projection of $l$ along the magnetic-field quantization axis [7]. Through least-square iterations by comparison with experimental data, the initially unknown values of $a_6$, $a_8$, and of all other parameters entering the CC Hamiltonian were optimized [48].

A global least-square fit – able to reproduce all observed FR locations with very good accuracy – provided the best-fit results $a_6 = 15.46(15)\ a_0$, $a_8 = 41.48(2)\ a_0$, $C_6 = 922(6)\ a.u.$, and $C_8 = 9.8(5)\,10^4\ a.u.$, with errors denoting one standard deviation obtained from the fit covariance matrix. The Li-Cr scattering properties obtained from the optimized CC model of Ref. [48] can be summarized as follows: First, the Li-Cr mixture exhibits a background $s$-wave scattering length, which is almost everywhere close to the octet $a_8$ value, of about 42 $a_0$. The low-field spectral region is entirely dominated by $p$-wave FRs, featuring $m_l$ splittings much larger than those found in alkali systems [87–89], owing to the increased role of spin-spin dipole coupling in Li-Cr mixtures, and to the coincidentally small relative magnetic moment of the molecular states involved. Particularly interesting in this respect is the presence, in the Li$|2\rangle$-Cr$|1\rangle$ mixture, of a strong $p$-wave FR with $m_l = -1$, centered around 24 G and essentially immune to two-body losses. This feature, which is intrinsically *chiral* in nature, could serve for future many-body surveys of $p$-wave resonant Fermi mixtures [92] in yet unexplored regimes. Also several $s$-wave FRs were identified within various Li-Cr spin-combinations. Owing to the relatively small values of $a_6$ and $a_8$, similarly to the Li-K case [40, 63], these features are generally narrow in nature, since the FR character – as for bi-alkalis [7] – is determined by the difference between sextet and octet scattering lengths, the larger being this difference,

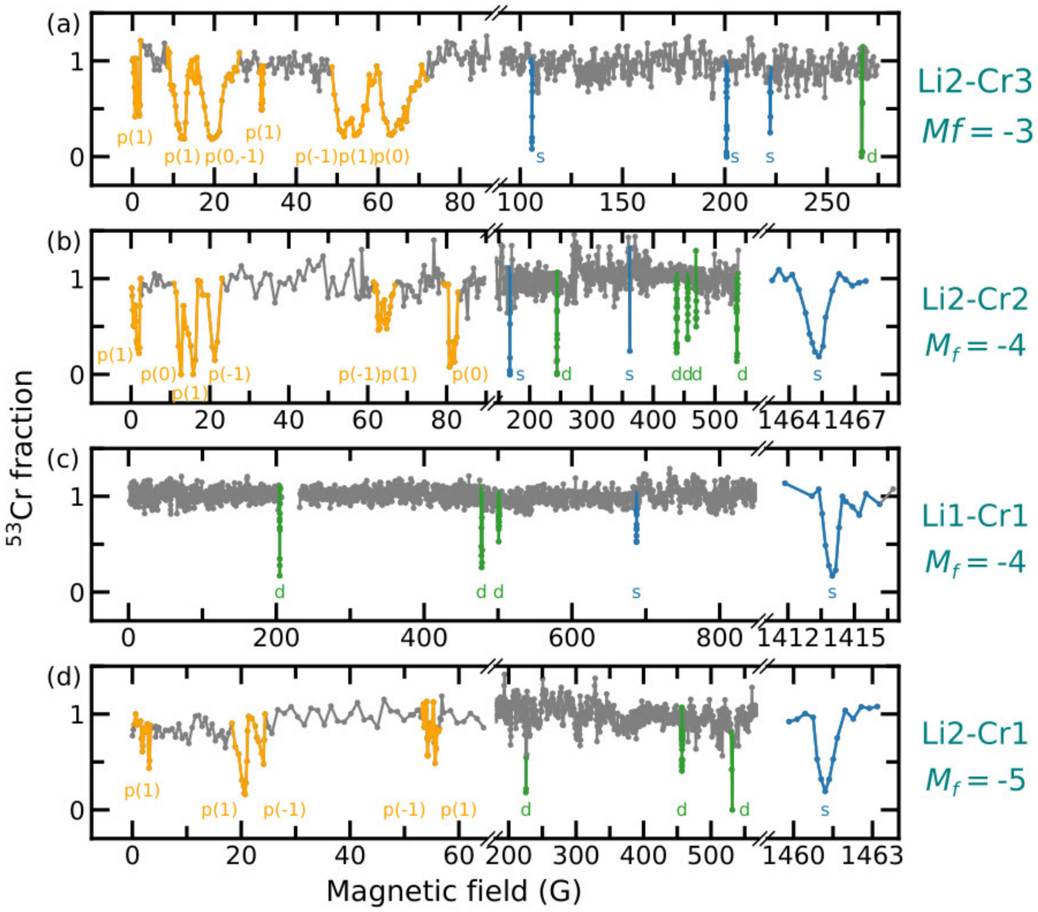

**Figure 3.1.** Overview of $^6$Li-$^{53}$Cr loss spectra. The remaining Cr number, normalized to its background value, recorded after an interaction time $t_H$ with lithium, is plotted as a function of the magnetic field for four different combinations: **(a)** Li$|2\rangle$-Cr$|3\rangle$, $M_f = -3$; **(b)** Li$|2\rangle$-Cr$|2\rangle$, $M_f = -4$; **(c)** Li$|1\rangle$-Cr$|1\rangle$, $M_f = -4$; **(d)** Li$|2\rangle$-Cr$|1\rangle$, $M_f = -5$. Each point is the average of at least four independent measurements. $t_H$ =4 s for all but the (c) panel, where $t_H$ =5 s. Features that the quantum collisional model developed by A. Simoni links to $s$-, $p$- and $d$-wave molecular levels are colored blue, orange and green, respectively. Numbers in brackets indicate the assigned $m_l$. Figure and caption adapted from Ref. [48].

the wider the corresponding features [7]. Specifically, the model of Ref. [48] connects all FRs observed above 1400 G to $l_r = 0$ molecular levels of $X^6\Sigma^+$ potentials, all featuring magnetic-field widths $\Delta B \sim 0.5$ G and differential magnetic moments $\delta\mu = 2$ $\mu_B$, yielding effective-range parameters of $R^* \sim 6000$ $a_0$, in perfect agreement with the expectation given by Eq. (1.19). Most importantly, one of these features occurs around 1414 G within the absolute Li$|1\rangle$-Cr$|1\rangle$ ground state, thus completely immune to two-body inelastic losses, and a second one is found at 1461 G for the Li$|2\rangle$-Cr$|1\rangle$ mixture, also exhibiting negligible dipolar relaxation rates. These two features are the ones that we have characterized in the experiments performed during my thesis, focusing in particular on the atom-to-molecule conversion process, as outlined in the following.

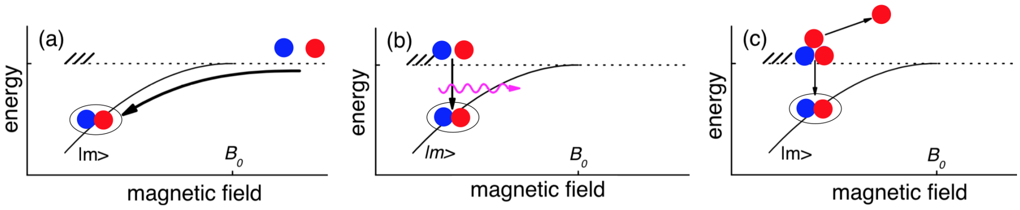

**Figure 3.2.** Illustration of experimental schemes typically employed to create ultracold molecules from ultracold atoms. The solid line marks the weakly bound molecular state $|m\rangle$, which dissociates into the continuum – indicated by the dotted line – at resonance $B = B_0$. In panel (a), the magnetic field is ramped across the resonance, which adiabatically converts two interacting atoms into one molecule; in (b), an oscillatory magnetic field drives the transition from the scattering state to the molecular state. In a similar way, a radio-frequency pulse can drive the transition from a non-resonant scattering state into the dimer level, by changing the internal state of one (or both) atoms; in (c), a three-body recombination event results in molecule formation. Figure adapted from Ref. [7]

## 3.2 Ultracold Feshbach molecule formation

Realizing ultracold gases of molecules, rather than atoms, represents a major goal for a rapidly developing and cross-disciplinary research field, spanning from cold chemistry and precision measurements, to many-body physics studies and quantum information processing. Among various possibilities, conversion of pairs of ultracold atoms into weakly-bound molecules close to a Feshbach resonance, represents the sole experimental method that, so far, has allowed to produce molecular gases in the sub-μK temperature, and at phase-space densities close to, or even above, 1, i.e. in the quantum-degenerate regime. Feshbach resonances here provide the experimental key to bind pairs of colliding atoms into molecules. Various schemes to create ultracold molecules near Feshbach resonances have been developed over the last two decades, and most of them rely on the application of time-varying magnetic fields. The three panels of Fig. 3.2, adapted from Ref. [7], summarize three of such schemes, which have been applied to a variety of bosonic and fermionic atomic gases, as well as to an increasing number of heteronuclear mixtures.

Ramping an external magnetic field across a Feshbach resonance is the most commonly adopted scheme to form Feshbach molecules. This scheme, usually referred to as a Feshbach ramp, or to magneto-association, is based on the concept that the resonant coupling between the scattering state and the molecular one opens up a way to adiabatically convert interacting atom pairs into weakly-bound molecules. The atomic gas is prepared at a magnetic field $B_i$ away from resonance on the BCS side, where the two-body system does not support a weakly bound state, and the scattering length is $a < 0$, see Chapter 1: in the example of Fig. 3.2(a), where the magnetic moment of the molecular state is lower than that of the atomic state, this corresponds to $B_i > B_0$. In order to implement the adiabatic passage, the field is then ramped to a final value $B_f$ below the center of the resonance, $B_f < B_0$, where a weakly bound state exists just below the scattering threshold, thus converting atom pairs into Feshbach molecules. To optimize the atom-to-molecule conversion on a specific Feshbach resonance, hence to maximize the final number of Feshbach molecules, it is crucial to optimize the ramp speed and the phase-space density of the parent atomic gases. Since this method relies on an adiabatic passage, in the limit in which inelastic losses can be neglected, the efficiency is expected to increase for decreasing $B$-field ramp rate. Quite generally the magneto-association efficiency is well described by a Landau-Zener model of the following kind [93]:

$$f = f_0 \left(1 - e^{-\Gamma/(f_0|\dot{B}|)}\right), \tag{3.1}$$

where $f$ is the efficiency, $\Gamma$ is a characteristic ramp rate, and $f_0$ is the saturation value reached for slow $B$ field ramps. For simplicity, we here assume $f$ to be measured with respect to the minority atomic component, although the discussion can be equivalently carried out in the opposite case. This model is particularly instructive, since it allows us to independently extract information about the fast-sweep regime, i.e. $\Gamma/(f_0|\dot{B}|) \ll 1$ where $f \to \Gamma/|\dot{B}|$, and the saturated regime, i.e. $\Gamma/(f_0|\dot{B}|) \gg 1$ and $f \to f_0$. These two regimes are governed by different physical mechanisms. The former only concerns the two-body physics and only depends on the collision parameters, atomic densities and $|\dot{B}|$ as follows [93]:

$$\Gamma = \langle n \rangle \frac{(2\pi)^2 \hbar}{\mu} \left| a_{bg} \Delta \right| . \tag{3.2}$$

Here $\langle n \rangle$ is the density of the majority component averaged over the distribution of the minority one, $\mu$ is the reduced mass of the system, $a_{bg}$ is the background scattering length, and $\Delta$ is the width of the resonance. The latter, namely the saturated regime, is determined by the thermodynamics of the sample, and experiments show that the saturated efficiency increases with increasing phase-space density of atomic gases. Despite the lack of analytical models, Monte-Carlo simulations based on the idea that atoms can only be associated if they lie within a certain distance in phase-space from each other, were shown to provide a quantitative description for Bose gases, Fermi gases, as well as Bose-Fermi mixtures, albeit less accurately for heteronuclear mixtures [7, 93, 94].

Another powerful method to produce ultracold Feshbach molecules is based on a modulation of the magnetic field strength, named “wiggle spectroscopy”. The oscillating field induces a stimulated transition of two colliding atoms into a bound molecular state, when the modulation frequency is tuned to match the dimer binding energy, see Fig. 3.2(b). This technique is especially useful for bosonic gases, because wiggle association can occur at bias fields $B < B_0$ quite far away from the resonance pole $B_0$, where heating and atom losses remain moderate or negligible. An alternative method conceptually similar to wiggle spectroscopy is based on RF spectroscopy. In this case, a radio-frequency pulse can drive the transition from the scattering state of a non-resonant atom pair into the dimer level associated with the FR, by changing the internal state of one atom (or of both, in the case of spin-polarized bosons). In contrast to the magnetic field modulation method, radio-frequency transitions – typically falling in the range of tens of MHz – involve a change of spin channel.

A particular situation for molecule formation arises for spin mixtures of $^6$Li near the broad 832 G Feshbach resonance. On the low-field side of the FR there

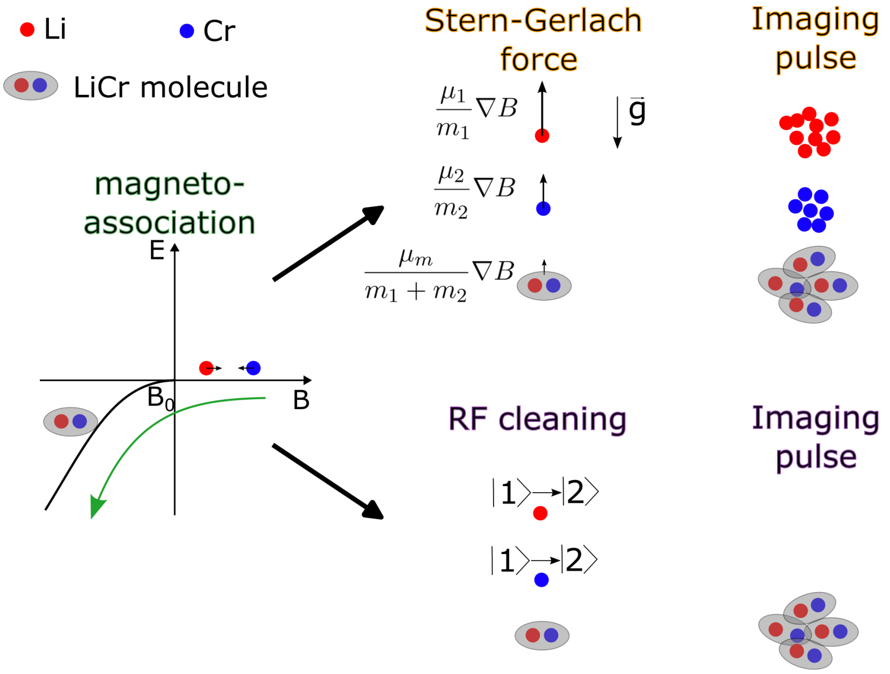

**Figure 3.3.** Scheme of the two methods used for detecting LiCr molecules. (above) Exploiting the *Stern-Gerlach* force, we can spatially resolve dimers from atoms in absorption imaging signals; (below) the RF cleaning method allows us to remove unbound Li and Cr atoms via an RF transfer to a dark state that does not interact with the imaging light.

is a wide field range, where the $s$-wave scattering length is large and positive and where the weakly bound state exhibits a pronounced halo character, see Chapter 1. The molecular state shows an extraordinary stability against inelastic decay, which opened the way to efficiently create molecular BECs by straightforward evaporative cooling at a constant magnetic field $B < B_0$. The formation of molecules in this region can be understood in terms of a chemical atom-molecule equilibrium [95, 96], where exoergic three-body recombination events compete with endoergic two-body dissociation processes, see Fig. 3.2(c). From a balance of these processes one can intuitively understand that molecule formation is favored at low temperatures and high number densities, i.e. at high phase-space densities. Such a method is extremely powerful, but it has a more limited range of applicability compared with the former ones, as it requires fermionic species – or fermionic mixtures – that exhibit broad resonances with $s_{res} \gg 1$.

## 3.3 Ultracold Feshbach molecule detection

None of the techniques described above can be experimentally demonstrated and optimized without counting the number of associated molecules. An implicit requirement is the ability to isolate and identify a molecule signal from an atomic signal in absorption images. The main problem to be addressed is the fact that Feshbach molecules, given their weak but non-zero binding energy, do not feature cycling optical transitions spectrally resolved from the atomic ones [7]. Typically, molecules are imaged through their constituent atoms after dissociation. This can either be forced by an inverse Feshbach ramp, or simply result from photon scattering when an imaging pulse addressing the close-by atomic line is applied. While the former case is quite general, the latter requires a sufficiently strong coupling of the Feshbach state with the atomic light and, correspondingly, low binding energies [57, 93]. Given the lower effective cross-section of molecule-light interaction compared to the atom-light case, the observed molecule numbers are in principle an underestimation [93].

There are two methods in which the resulting absorption signal can be isolated from the atomic ones. The first method consists in a *Stern-Gerlach* type experiment, in which the different acceleration resulting from a Stern-Gerlach force is exploited to resolve the molecular from atomic clouds, see Fig. 3.3. After magneto-association, the trap is switched off and a vertical magnetic field gradient $\nabla B$ is applied during the subsequent time of flight. The centers of mass of the atomic and molecular clouds will then be subject to different accelerations. Let us call $m_{1,2}$ the atomic masses, $\mu_{1,2}$ the atomic magnetic moments and $\mu_m$ the molecule magnetic moment. Then the centers of mass of the atomic clouds will move with an acceleration $g + \mu_{1,2} \times \nabla B / m_{1,2}$, while the molecular cloud will have an acceleration given by $g + \mu_m \times \nabla B / (m_1 + m_2)$. Because of the time of flight expansion due to the small but finite temperature of the ultracold gas, $\nabla B$ must be large enough to be able to resolve the molecule cloud from the atomic one. Finally, absorption imaging is performed. This method exploits the different kinematics to resolve the particle species and isolate the molecule signal.

The second method requires the selective transfer of only the atomic component to another internal state which does not interact with the imaging pulse, i.e. a dark state, see Fig. 3.3. Recalling the main problem discussed above, the state transfer cannot be typically performed optically. The transfer is often achieved by exploiting a Radio-frequency transition from the initial Zeeman level $|1\rangle$ to a final Zeeman level $|2\rangle$. The transition line is narrow enough to spectrally resolve molecules from atoms even for very weak binding. Afterwards, absorption imaging can be performed. We stress that this method can be used to expel the leftover atoms from the trap with little effect on molecules, by exploiting a dedicated optical blast resonant with state $|2\rangle$. Finally, we note that this method can be used in combination with an inverse Feshbach ramp, as to dissociate molecules prior to the imaging pulse and resulting in stronger absorption signal and more accurate counting [93].

In the following, both detection methods will be used, without the need for an inverse Feshbach ramp before the imaging pulse over the explored final $B$-field detunings. In fact, we have experimentally verified that, by doing so, the molecule number is only slightly underestimated, by less than 10%, which can be neglected in this work.

## 3.4 Experimental procedures and first results

The collision parameters associated with the Feshbach resonance exploited in the experiment set some practical experimental requirements to be met in the laboratory. To explore resonantly interacting Li-Cr Fermi mixtures and magneto-associate LiCr

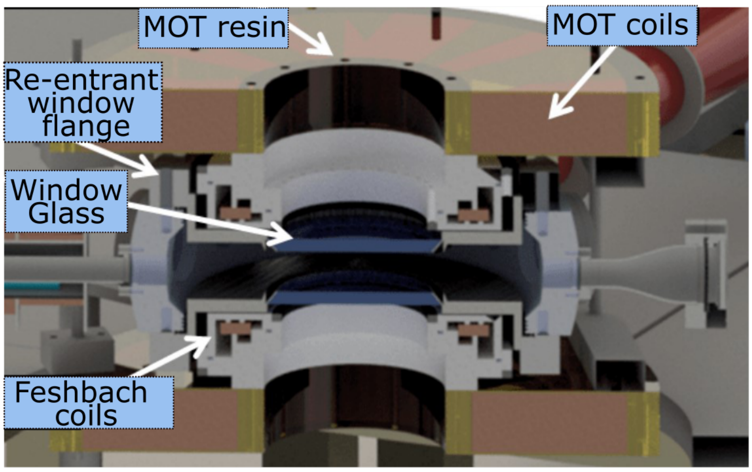

**Figure 3.4.** Cross section drawing of the experimental chamber where the main MOT and Feshbach coils are shown.

dimers, we focused on the $s$-wave resonance between Li$|1\rangle$ and Cr$|1\rangle$, located at approximately 1414 G, and on the resonance between Li$|2\rangle$ and Cr$|1\rangle$ at 1461 G, as discussed in Chapter 3.1. This choice was motivated by three factors: first, the absence of the centrifugal barrier in the interatomic potential due to its $s$-wave nature; second, the largest available $\Delta B/B_0 = 3 \times 10^{-4}$ of the entire Feshbach spectrum; and finally, immunity to two-body losses. Meeting these practical requirements associated with the collision parameters of the resonance was crucial for the success of the experiment. The relevant collision parameters are the background scattering length $a_{bg} = 42\, a_0$, the differential magnetic moment $\delta\mu = 2\mu_B$ between the atomic scattering state and the molecular state, the magnetic field width $\Delta B = 0.47$ G, and $R^* = 6000 a_0$.

As explained in Chapter 1, these resonances are narrow, and the strongly interacting region where we expect $|k_F a| > 1$ for our sample conditions is of order 10 mG, to be compared with the offset field of 1414 G. Moreover, since it is located at such a high field, the RF-transitions between lowest lying, high-field seeking states of Li and Cr are extremely weak.

The narrow resonance nature, combined with a high $B_0$, calls for high stability and precise tuning of the magnetic field. To achieve this, several sets of coils serve for different purposes, as shown in Fig. 3.4. First, the large MOT coils offer the bulk of the magnetic field bias, with a resolution of approximately 45 mG. Their current is stabilized using an UltraStab LEM (see Section 5 for details). Second, the "Feshbach" coils produce a magnetic field gradient for the compensation of the differential gravitational sag and Stern-Gerlach separation experiments. Third, vertical compensation coils, located a few cm away from the MOT coils (not shown in the Figure), finely tune the magnetic field on the few-ms timescale around the MOT coils field bias, with a resolution of approximately 2 mG. Finally, a small one-loop coil beneath the bottom glass window (not shown in the Figure) drives radio-frequency radiation, inducing transitions between lowest Zeeman levels of lithium at around 80 MHz.

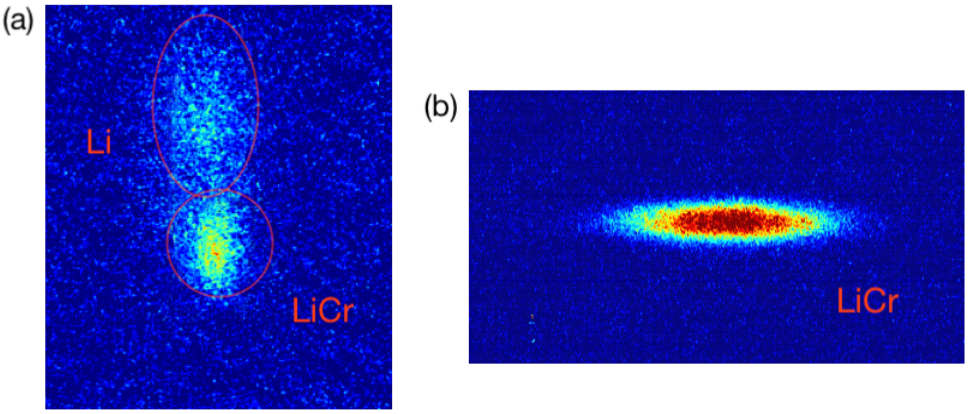

**Figure 3.5. (a)** Typical absorption image on the Li atomic line used to detect molecules with the *Stern-Gerlach* method: LiCr molecules and lithium atoms are spatially resolved. **(b)** Absorption image on the Li atomic line used to detect molecules with the *RF cleaning* method: all the unbound atoms have been transferred into a dark state and only molecules are visible.

The basic experimental sequence used to produce a molecular gas starts after the forced evaporation and sympathetic cooling of the Li-Cr mixture described in Chapter 2. After “Feshbach” cooling, we first ramp the field with the compensation coils further away from the resonance pole on the BCS side to a detuning of about 100 mG, where the atoms are only weakly interacting, and three-body recombination is negligible. After that, we perform a linear ramp with a typical inverse rate of about 100 ms/G in order to cross the resonance and stop below the resonance pole on the BEC side of it. Finally, we can detect the molecules with either of the two methods described above, without the need for an inverse Feshbach ramp. For the Stern-Gerlach type experiment, we employ the very same gradient already present at the end of evaporation, of about 1.5 G/cm, which levitates chromium atoms, pushes lithium atoms upwards, and lets molecules fall. After switching off of the BODT, atoms and molecules undergo a 10 ms-long time of flight before absorption imaging, which shows clearly resolved atomic lithium and molecules signal, see Fig. 3.5(a).

For the RF cleaning method, we switch off the ODT, we transfer lithium atoms from state $|1\rangle$ to $|2\rangle$, and then take an absorption picture with zero atomic background, see Fig. 3.5(b). The RF pulse is applied during the first few ms of time of flight, when the atom-molecule density overlap is already dropped, as to avoid unwanted shifts and broadening of the atomic transition line. Since the magnetic moment of the transition of the lithium at this field is only 37.7045 kHz/G, the oscillating $B$-field amplitude needed to drive 1 ms-long $\pi$-pulses is about 13 mG, which requires sending about 20 W of RF power to our antenna. For this purpose we employ a 100 W amplifier after our waveform synthesizer.

In the following, I present preliminary results on the maximum number of associated molecules and conversion efficiency. The initial atomic samples are confined in the final bichromatic optical trap, as described in Chapter 2, the only difference being that right before the magneto-association ramp, the power of the green ODT is reduced to optimize the molecule number. The lithium sample has a

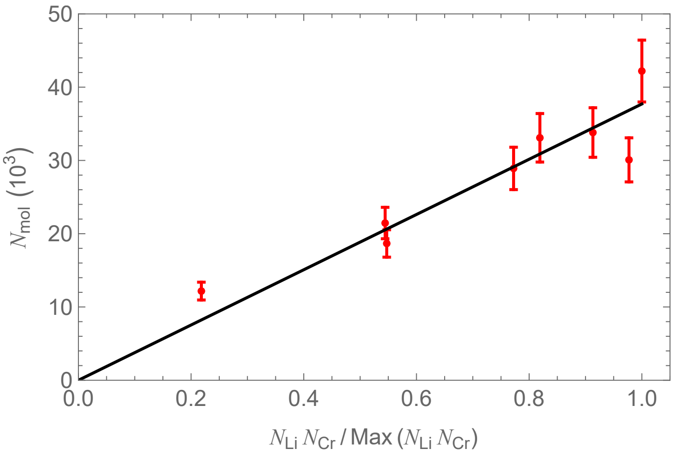

**Figure 3.6.** Number of LiCr dimers as a function of the product between the initial lithium and chromium atom number. The molecule number increases linearly with the initial number of atom pairs, as expected.

temperature of approximately 160 nK, peak density of $8 \times 10^{11}\mathrm{cm}^{-3}$ and reduced temperature $T/T_{F\,Li} = 0.25$, while the chromium sample has a temperature 200 nK, peak density of about $1 \times 10^{12}$ $\mathrm{cm}^{-3}$ and reduced temperature $T/T_{F\,Cr} = 0.5$. These conditions represent typical Fermi mixtures obtained in our laboratory, consisting of $160 \times 10^3$ $^6$Li and $90 \times 10^3$ $^{53}$Cr atoms at the end of evaporation.

First, we measure the total number of Feshbach dimers as a function of $N_{Li} \times N_{Cr}$ via the Stern-Gerlach detection method. $N_{Li} \times N_{Cr}$ is varied by tuning the number of Cr atoms loaded initially into the ODT from the C-MOT while keeping the evaporation parameters and final trap configuration fixed. The results are reported in Fig 3.6. Our results show that almost $50 \times 10^3$ molecules can be routinely produced in our laboratory from the largest samples, and that the number of molecules is indeed proportional to the product of $N_{Li}$ $N_{Cr}$ as expected, with no sign of saturation effects.

In the second measurement, exploiting the largest mixtures we could produce, we measure the association efficiency with respect to the minority component of Cr atoms, as function of the inverse $B$-field ramp rate. To perform this measurement, we employ RF cleaning on lithium, followed by Li and Cr imaging pulses to count the molecule number and the total number of associated and non-associated Cr atoms, i.e. the initial Cr atom number. The results are presented in Fig. 3.7.

As explained in Section 3.2, the data can be fitted with the well-known Landau-Zener functional form of Eq. (3.1), with best-fit parameters of $f_0 = 0.62(7)$ and $\Gamma = 6.8(4) \times 10^{-3}$ G/ms, respectively. The solid line indicates the fitted Landau-Zener behavior, the dashed line describes the fast-sweep regime, and the dotted line shows the saturated conversion efficiency. It is worth noting that the obtained 62% efficiency is relatively high compared to the literature, especially for other Fermi mixtures using narrow Feshbach resonances (about 40% in $^6$Li-$^{40}$K, see Ref. [57]). The extracted value of $\Gamma$ can be compared with the theoretical prediction given by Eq. (3.2), which yields 0.24 G/ms, using the resonance parameters and the observed Li density averaged over the Cr cloud of $\langle n_{Li} \rangle = 4.7 \times 10^{11}$ $\mathrm{cm}^{-3}$. This value is more

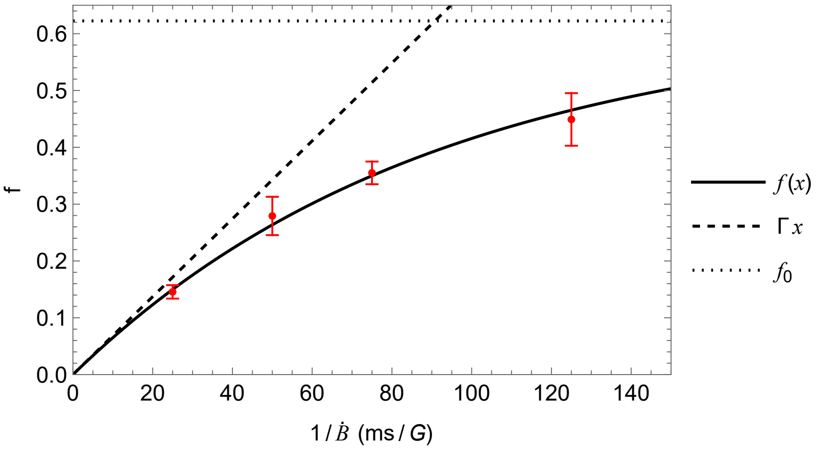

**Figure 3.7.** Atom-molecule conversion efficiency $f$ referenced to the Cr atom number as function of the inverse ramp rate $x = 1/\dot{B}$. Red circles show the experimental results, while the solid line shows the fitted Landau-Zener model. The dashed line shows the derived efficiency in the fast ramp limit, and the dotted line shows the saturated efficiency.

than one order of magnitude larger than the experimental value and the origin for such a mismatch is currently under investigation.

These experimental results are extremely appealing, as they testify that Li-Cr mixtures are ideal for studies of resonantly-interacting Fermi mixtures and production of dimers. However, the experiment also highlighted some technical limitations. In particular, if the end point of the magneto-association ramp was set too close to the resonance pole, say within 20 mG from it, the molecule number showed large shot-to-shot fluctuations. This problem was avoided in the measurements described above by setting a sufficiently large final detuning from resonance. Later and more advanced experiments on LiCr molecules clearly showed the limitations arising from magnetic field noise.

In order to quantitatively assess our magnetic field stability, we focused on the molecule magnetic dipole moment. This is expected to vary as a function of the detuning from resonance according to the mixing of the molecule and atomic scattering state, which is quantified by the open and closed channel fractions (see Chapter 1).

We measured the magnetic moment of LiCr dimers via a Stern-Gerlach type experiment. In this experiment, the Stern-Gerlach force was applied for a fixed time of flight but the final detuning from the resonance pole was varied. After the time of flight an absorption picture was taken, from which the center of mass of the molecule cloud was extracted and used to infer the magnetic moment, knowing the initial *in-situ* position, the gradient $\nabla B$, the molecule mass, $m_{Li} + m_{Cr}$. The data are shown in Fig. 3.8 together with the analytic theory curve Eq. (1.26). Interestingly, despite the narrow character of the resonance, the magnetic field stability and the signal to noise ratio in absorption images were high enough to observe the predicted magnetic moment variation. However, on a quantitative basis, the data appeared to be significantly smeared out, compared to the theoretical curve.

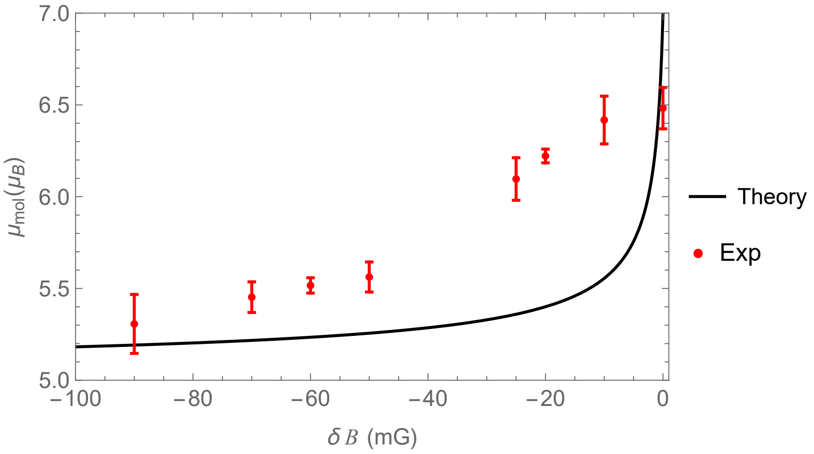

**Figure 3.8.** Magnetic dipole moment of LiCr dimers as function of magnetic field detuning ($\delta B$) from the resonance pole. Red circles show the measurement results and the solid line is the theoretical expectation obtained from Eq. (1.26), using the open-channel fraction in Eq. (1.25) to interpolate between the atomic ($7\,\mu_B$) and molecule ($5\,\mu_B$) magnetic moments.

From the above discussion, we concluded that there were two main problems to be addressed on the experiment. The first is the stability of the bias Zeeman field, and the second is the inefficient driving of Li$|1\rangle\to$Li$|2\rangle$ transitions at such high B-fields. The latter issue is also a possible cause of magnetic field noise, since when using high RF power, we observe a strong perturbations of the $B$-field current stabilization electronics, hence of the magnetic field experienced by the molecules. Moreover, independently of the antenna efficiency, the employed lithium RF transition requires a strong oscillating $B$-field, which, by construction, has a non-negligible component along the vertical axis, thus directly causing a modulation of the bias $B$-field experienced by the molecules.

We found that using RF transitions on the chromium species is a principal solution to these problems. Indeed, given the RF transition shift of $\delta\mu/h = 6.041\,\mathrm{kHz/G}$ and $\delta\mu/h = 0.77\,\mathrm{kHz/G}$, for Cr and Li respectively, the new antenna is expected to yield a 8-fold increase in the sensitivity to the Zeeman field. As it will be explained in Chapter 5, this will allow us to characterize the corresponding magnetic field noise and significantly reduce it by active compensation. In addition, the transition dipole moment of Cr$|1\rangle\to$Cr$|2\rangle$ is about $\mu_{eg}/h = 156.402\,\mathrm{kHz/G}$, while the one of Li$|1\rangle\to$Li$|2\rangle$ is $\mu_{eg}/h = 37.7045\,\mathrm{kHz/G}$, thus leading to a four-fold increase of the Rabi frequency for fixed RF $B$-field amplitude.

The use of a new chromium antenna, which I will discuss in the next Chapter, has several important implications that have enabled us to improve the overall quality of our experiments. First, a lower RF power is required for fixed antenna radiation efficiency, which reduces the cross-talk with current stabilization electronics. This has allowed us to minimize the effect of undesired interference, and to improve the precision of our measurements. Additionally, the smaller amplitude of the oscillating $B$-field needed for fixed $\pi$-pulse time in combination with a dedicated antenna design, significantly reduces the unwanted modulation of the bias $B$-field onto the molecules.

In the following chapters, I will provide a detailed explanation of how I built an efficient antenna addressing chromium RF transitions, and how I used it to characterize and improve the $B$-field stability of the experiment. Thanks to these technical improvements, which represent my major contribution to the Li-Cr experimental setup during my thesis period, we have been able to optimize our experimental apparatus, and to improve the accuracy and precision of our measurements.

# Chapter 4

# Radio-Frequency antenna

One of my main contributions to the experiment during my thesis has been the realization of a high-current radio-frequency (RF) antenna, allowing us to perform fast and coherent transitions between the lowest Zeeman levels of the ground-state of $^{53}$Cr at high magnetic fields of about 1.4 kG. With the constant support of A. Trenkwalder I designed, produced and tested the antenna that I subsequently installed on the main experimental apparatus, above the top re-entrant window of the experimental chamber. Since the coupling term of the transition $\mathrm{Cr}|1\rangle \rightarrow \mathrm{Cr}|2\rangle$ is relatively low, i.e. $\mu_\perp/h = 156.402\,\mathrm{kHz/G} \ll \mu_B/h = 1.4\,\mathrm{MHz/G}$, we need a sufficiently high RF intensity in order to drive fast transitions on the Cr atoms. For this reason, the AC current through the antenna and thus the transverse $B$-field has to be maximized and the antenna has to be placed close to the atoms on a viewport to avoid shielding of the metallic vacuum chamber, but without blocking optical access. Moreover, unwanted radio-frequency interference with other parts of the experiment should be minimized.

To take all these issues into account, I made use of the idea of F. Scazza *et al.* [97], who created a highly-performing banana-shaped antenna at 80 MHz, for the lithium experiment at *LENS*. In addition to taking into account space limitations, and without blocking access for laser beams, the banana-shaped antenna also allows for an excellent efficiency in terms of radiated power. The main difference from the design in Ref. [97] is our operating frequency of 240 MHz used to transfer chromium atoms between the two lowest hyperfine states around 1414 G. The three times higher frequency results in small modifications of the design of the antenna matching circuit compared to Ref. [97].

In this chapter, following a brief theoretical introduction on radiation-matter interaction, I will present the details of the technical challenges which we had to overcome to finally construct an efficient high-power RF antenna at this frequency. In detail, I will explain the estimation of the magnetic field generated by the antenna coil, and the design and simulation of the matching circuit. I will describe how I have built the antenna and optimized the matching for the designed frequency and I will finally present measurements conducted with chromium atoms that show that this antenna performs very well and perfectly matches the expectations.

## 4.1 Atoms interacting with electro-magnetic fields: recall of some textbook results

Let us approximate an atom as a two-level system, which is immersed in a radiation field oscillating at frequency $\omega$. The two-level approximation is justified when $\omega \sim \omega_0$, where $\omega_0$ is the frequency separation between the two atomic levels (see Fig. 4.1). A generic state can be expressed as [98]

$$|\psi\rangle = a_g\,|g\rangle + a_e\,|e\rangle\,, \tag{4.1}$$

where $|g\rangle$ and $|e\rangle$ represent the electronic ground state and the excited state with energies $\hbar\omega_g$ and $\hbar\omega_e$, respectively. The separation in energy between these states defines the resonance frequency in radians per second $\omega_0 = \omega_e - \omega_g$. The Hamiltonian relative to the unperturbed atom can be written in its eigen-basis as:

$$H_{at} = \hbar\omega_g\,|g\rangle\,\langle g| + \hbar\omega_e\,|e\rangle\,\langle e| \tag{4.2}$$

Following Ref. [98] we introduce the relevant Hamiltonian for the atomic electron interacting with an external electromagnetic field:

$$H = \frac{[\boldsymbol{p} + e\boldsymbol{A}(\boldsymbol{r},t)]^2}{2m} - eV(\boldsymbol{r},t) + U(\boldsymbol{r}), \tag{4.3}$$

where $\boldsymbol{A}(\boldsymbol{r},t)$ and $V(\boldsymbol{r},t)$ are, respectively, the vector and scalar potentials describing the electromagnetic field, which are connected to the electric field $\boldsymbol{E}$ and to the magnetic field $\boldsymbol{B}$ by the relations

$$\begin{aligned} \boldsymbol{B} &= \nabla \times \boldsymbol{A} \\ \boldsymbol{E} &= -\nabla V - \frac{\partial \boldsymbol{A}}{\partial t}. \end{aligned} \tag{4.4}$$

$U(\boldsymbol{r})$ accounts for the interaction between the atomic nucleus and the electron. We are examining the scenario of classical radiation, where the field propagates in the

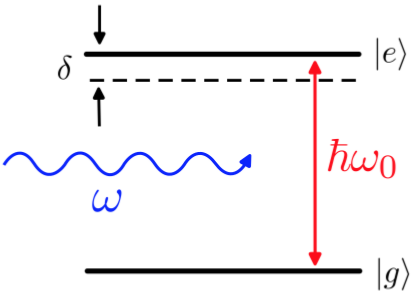

**Figure 4.1.** Scheme of a two-level atom, ground state $|g\rangle$ and exited state $|e\rangle$, separated by an energy $\hbar\omega_0$, immersed in an electromagnetic field oscillating at frequency $\omega$, detuned by $\delta$.

direction of the $z$-axis as a planar wave, exhibiting both electric and magnetic fields

$$\begin{aligned} \boldsymbol{E}(z,t) &= E_0 \cos(kz - \omega t)\,\hat{x} = \frac{E_0}{2}\left[e^{i(kz-\omega t)} + h.c.\right]\hat{x} \\ \boldsymbol{B}(z,t) &= B_0 \cos(kz - \omega t)\,\hat{y} = \frac{B_0}{2}\left[e^{i(kz-\omega t)} + h.c.\right]\hat{y}. \end{aligned} \tag{4.5}$$

The measurable fields $\boldsymbol{B}$ and $\boldsymbol{E}$ associated with the potentials $\boldsymbol{A}$ and $V$ are invariant under "gauge" transformations

$$\begin{aligned} \boldsymbol{A} &\to \boldsymbol{A}' = \boldsymbol{A} + \nabla\chi \\ V &\to V' = V - \frac{\partial \chi}{\partial t}, \end{aligned} \tag{4.6}$$

where $\chi$ is an arbitrary scalar function.

Therefore, the potentials $\boldsymbol{A}$ and $V$ are not unique but an appropriate "gauge" must be selected. We use the *radiation gauge*:

$$\begin{aligned} \boldsymbol{A}(z,t) &= \frac{E_0}{2}\left[\frac{1}{i\omega}e^{i(kz-\omega t)} + h.c.\right]\hat{x} \\ V(z,t) &= 0. \end{aligned} \tag{4.7}$$

The spacial dependence of the vector potential can be approximated by a series expansion of the $e^{ikz}$ term. Typical dimensions of atomic orbitals are on the order of the Bohr radius ($a_0 \simeq 0.53\mathring{A}$), which is significantly smaller than the wavelength $\lambda = 2\pi/k$ of the radiation required to resonantly excite the atoms (in the visible, or in the RF range, as for our case of interest). Consequently, since $a_0 \ll \lambda$, the spacial variation of the electromagnetic field on the unperturbed electron wavefunction can be neglected, $kz \ll 1$, and the zero-order electric dipole approximation can be applied, i.e.

$$e^{ikz} \sim 1. \tag{4.8}$$

Under the electric dipole approximation, $\boldsymbol{A}$ does not depend on position. It is thus possible to choose a gauge function $\chi = -\boldsymbol{r}\cdot\boldsymbol{A}$, which allows us to cancel the contribution of the vector potential:

$$\begin{aligned} \boldsymbol{A}'(\boldsymbol{r},t) &= 0 \\ V'(\boldsymbol{r},t) &= \boldsymbol{r}\cdot\frac{\partial A}{\partial t} = -\boldsymbol{r}\cdot\boldsymbol{E}(t). \end{aligned} \tag{4.9}$$

With this convenient *gauge* choice for the electromagnetic potential, the derivation of the interacting Hamiltonian is easier, and Eq. (4.3) can be written as

$$H = \frac{\boldsymbol{p}^2}{2m} + U(\boldsymbol{r}) + e\,\boldsymbol{r}\cdot\boldsymbol{E}(t), \tag{4.10}$$

in which we recognize $\boldsymbol{p}^2/2m + U(\boldsymbol{r})$ as the unperturbed Hamiltonian $H_a$, and the interaction term that corresponds to the potential energy $-\boldsymbol{d}\cdot\boldsymbol{E}(t)$ of an electric dipole $\boldsymbol{d} = -e\,\boldsymbol{r}$ in an oscillating electric field $\boldsymbol{E}(t)$.

On the basis spanned by the unperturbed electronic states $|g\rangle$ and $|e\rangle$, it is easy to show that the dipole interaction Hamiltonian $H_{int} = e\,\boldsymbol{r}\cdot\boldsymbol{E}(t)$ has off-diagonal matrix elements, i.e. it couples the ground and excited states according to:

$$\begin{aligned}\langle e|\,H_{int}\,|g\rangle &= \int d\boldsymbol{r}\,\psi_e^*(e\boldsymbol{r}\cdot\boldsymbol{E})\psi_g = \\ &= \frac{1}{2}e\boldsymbol{E}_0\left(e^{-i\omega t}+c.c.\right)\int d\boldsymbol{r}\,\psi_e^*\,\boldsymbol{r}\,\psi_g = \\ &= \frac{1}{2}e\boldsymbol{E}_0\left(e^{-i\omega t}+c.c.\right)\cdot\boldsymbol{d}_{eg} \\ &= \hbar\frac{\Omega}{2}\left(e^{-i\omega t}+c.c.\right),\end{aligned} \tag{4.11}$$

with $\boldsymbol{d}_{eg}$ denoting the $|g\rangle \rightarrow |e\rangle$ *transition dipole moment*, defined as

$$\boldsymbol{d}_{eg} \equiv -e\,\langle e|\,\boldsymbol{r}\,|g\rangle = -e\int d\boldsymbol{r}\,\psi_e^*\,\boldsymbol{r}\,\psi_g \tag{4.12}$$

which only depends on the unperturbed wavefunctions. The *Rabi frequency*, is defined as

$$\Omega \equiv -\frac{\boldsymbol{d}_{eg}\cdot\boldsymbol{E}_0}{\hbar} \tag{4.13}$$

and it quantifies how strong is the coupling between the two levels with the electromagnetic field. Considering that $\boldsymbol{r}$ is an odd operator, so that

$$\langle g|\,H_{int}\,|g\rangle = \langle e|\,H_{int}\,|e\rangle = 0. \tag{4.14}$$

The total Hamiltonian reads

$$H = \hbar\omega_g\,|g\rangle\,\langle g| + \hbar\omega_e\,|e\rangle\,\langle e| + \frac{\hbar\Omega}{2}(e^{-i\omega t}+c.c.)\,|e\rangle\,\langle g| + \frac{\hbar\Omega^*}{2}(e^{-i\omega t}+c.c.)\,|g\rangle\,\langle e| \tag{4.15}$$

which can be represented in the matrix form

$$H = \hbar\begin{pmatrix}\omega_g & \frac{\Omega^*}{2}(e^{-i\omega t}+c.c.)\\ \frac{\Omega}{2}(e^{-i\omega t}+c.c.) & \omega_e\end{pmatrix}. \tag{4.16}$$

In this representation, a constant energy term can be subtracted from the diagonal of the Hamiltonian. This redefinition ensures that the energy of the ground state is zero, while the energy of the excited state is given by $\hbar\omega_0 = \hbar(\omega_e - \omega_g)$.

Let us now focus our attention to the time-dependent Schrödinger equation that governs the dynamics of the system described by the Hamiltonian

$$i\hbar\frac{\partial}{\partial t}\,|\psi\rangle = H\,|\psi\rangle \tag{4.17}$$

with

$$|\psi\rangle = a_g\,|g\rangle + a_e\,|e\rangle. \tag{4.18}$$

Solving the time-dependent Schrödinger equation thus amounts to solve the system of coupled equations

$$\begin{cases} i\dot{a}_g = \frac{\Omega^*}{2}\left(e^{-i\omega t}+c.c.\right)a_e \\ i\dot{a}_e = \frac{\Omega}{2}\left(e^{-i\omega t}+c.c.\right)a_g + \omega_0\,a_e\end{cases} \tag{4.19}$$

for the amplitudes $a_g$ and $a_e$, respectively. The dotted coefficients $\dot{a}_g$ and $\dot{a}_e$ indicate their time derivatives. The differential equations with time-dependent coefficients in (4.19) can be simplified to a system of equations with constant coefficients using the *rotating wave approximation* (*RWA*). This amounts to expressing the equations in a rotating basis, and neglecting the fast-oscillating terms. One can choose different bases for the system, but a convenient option is to consider a new basis in which the ground state $|\tilde{g}\rangle$ is identical to $|g\rangle$, and the excited state $|\tilde{e}\rangle$ differs from $|e\rangle$ by a phase factor rotating at the same frequency $\omega$ as the driving field. Using this basis, the state $|\psi\rangle$ can be expanded as follows:

$$\begin{cases} \tilde{a}_g = a_g \\ \tilde{a}_e = a_e e^{i\omega t}. \end{cases} \tag{4.20}$$

Substituting Eq. (4.20) in Eq. (4.19) we obtain the equations for the new coefficients

$$\begin{cases} i\dot{\tilde{a}}_g = \frac{\Omega^*}{2}(1+e^{-2i\omega t})\tilde{a}_e \\ i\dot{\tilde{a}}_e = \frac{\Omega}{2}(1+e^{2i\omega t})\tilde{a}_g - \delta\tilde{a}_e, \end{cases} \tag{4.21}$$

where $\delta = \omega - \omega_0$ is the *detuning*, namely the difference between the oscillation frequency of the field and the one of the unperturbed atomic transition.

Since typically the Rabi frequency $\Omega \ll \omega$ and $\omega_0$, and $|\omega - \omega_0| = |\delta| \ll \omega + \omega_0 \sim 2\omega$, one can safely neglect the fast oscillating terms with $e^{\pm 2i\omega t}$ in Eq. (4.21), applying the *RWA*. As a result, the total Hamiltonian does no longer depend on time, and

$$H_{RWA} = \hbar \begin{pmatrix} 0 & \frac{\Omega^*}{2} \\ \frac{\Omega}{2} & -\delta \end{pmatrix}. \tag{4.22}$$

The Schrödinger equation can now be solved analytically. Assuming that at $t = 0$ $\psi(0) = |g\rangle$, so that

$$\begin{cases} \tilde{a}_g(t=0) = 1 \\ \tilde{a}_e(t=0) = 0. \end{cases} \tag{4.23}$$

It is easy to verify that the population of the ground and excited levels will evolve according with

$$\begin{cases} |\tilde{a}_g|^2 = |a_g^2| = 1 - \frac{|\Omega|^2}{\Omega'^2}\sin^2\left(\frac{\Omega'}{2}t\right) \\ |\tilde{a}_e|^2 = |a_e^2| = \frac{|\Omega|^2}{\Omega'^2}\sin^2\left(\frac{\Omega'}{2}t\right). \end{cases} \tag{4.24}$$

Here I have defined $\Omega' = \sqrt{\delta^2 + |\Omega|^2}$ as the generalized Rabi frequency. Hence, the probability $|a_e|^2$ to have the atom in the excited state oscillates in time with frequency $\Omega'$, performing *Rabi oscillation*, shown in Fig. 4.2 for different values of detunings, see legend. The green and orange lines represent two examples of off-resonance oscillations. When the radiation field is resonant with the atomic transition, the detuning is zero, and from Eq. (4.24) one obtains

$$|a_e|^2 = \sin^2\left(\frac{\Omega}{2}t\right). \tag{4.25}$$

This case is illustrated in Fig. 4.2 by the blue curve. Red dots in the Figure mark peculiar times of the oscillation at $\delta = 0$ explained below:

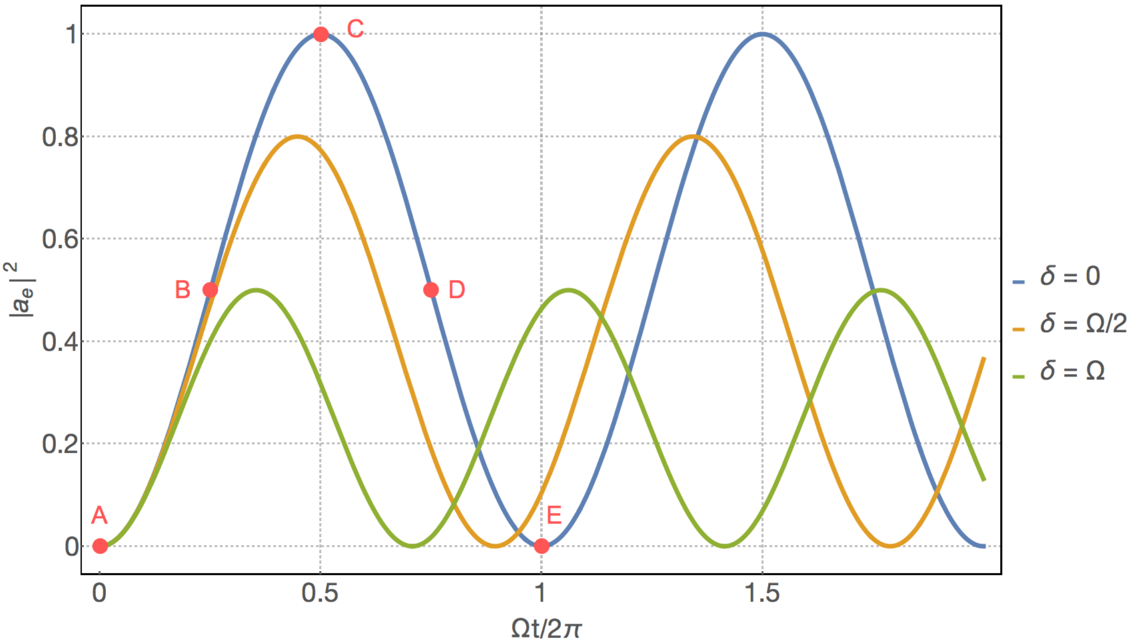

**Figure 4.2.** Rabi oscillations. The probability of the excited state population $|a_e|^2$ is shown as a function of time normalized to the on-resonance Rabi period $T = 2\pi/\Omega$. Blue line is relative to zero detuning. Green and orange lines are for $\delta = \Omega$ and $\delta = \Omega/2$ respectively. A and E points indicate atoms in the ground state. The point C identifies when the atoms are in the exited state, while in B and D the atoms are in a balanced superposition state between $|g\rangle$ and $|e\rangle$.

- A) At $t = 0$, the system is in the ground state $|\psi\rangle = |g\rangle$.
- B) At $t = \frac{\pi}{2\Omega}$, the system is in a superposition state $|\psi\rangle = \frac{1}{\sqrt{2}}(|g\rangle - i\,|e\rangle)$. This transfer time is named $\pi/2$-*pulse* time.
- C) At $t = \frac{\pi}{\Omega}$, $\pi$-*pulse*, the population inversion is complete, $|a_e|^2(\pi/\Omega) = 1$
- D) At $t = \frac{3\pi}{2\Omega}$, $|\psi\rangle = \frac{1}{\sqrt{2}}(-\,|g\rangle - i\,|e\rangle)$
- E) At $t = \frac{2\pi}{\Omega}$, the atoms are transferred back to the initial state, $|a_e|^2(2\pi/\Omega) = 0$.

In the out-of-resonance cases (green and orange lines), the excited state population oscillates at faster frequencies $\Omega'(\delta) > \Omega$, and the maximum possible transfer is given in this case by

$$|a_e|^2_{max} = \frac{|\Omega|^2}{\Omega'^2} = \frac{1}{1 + \frac{\delta^2}{|\Omega|^2}}. \tag{4.26}$$

For our case, the two atomic levels of chromium Cr$|1\rangle$ and Cr$|2\rangle$ are coupled by a magnetic dipole transition. The theoretical treatment leads to the same results, with few differences, explained below.

The electric dipole interaction term in Eq. (4.10) was derived from the approximation in Eq. (4.8), which involves neglecting the phase variation of the electromagnetic field across the atomic orbitals. By retaining additional terms in the expansion, higher-order interaction processes can occur, which have associated different selection rules

$$e^{ikz} \simeq 1 + ikz + ... \tag{4.27}$$

The effect of the first-order $ikz$ term is now being considered using the same approach as above, with technical details omitted. With this approximation, the electromagnetic potentials in the radiation gauge can be expressed as

$$\begin{aligned} \boldsymbol{A}(z,t) &= \frac{E_0}{2}\left[(1+ikz)\,e^{-i\omega t} + h.c.\right]\hat{x} \\ V(z,t) &= 0 \end{aligned} \tag{4.28}$$

and the resulting electric and magnetic fields, defined by Eq. (4.4), are

$$\begin{aligned} \boldsymbol{E}(z,t) &= \frac{E_0}{2}\left[(1+ikz)\,e^{-i\omega t} + h.c.\right]\hat{x} \\ \boldsymbol{B}(z,t) &= \frac{B_0}{2}\left[e^{-i\omega t} + h.c.\right]\hat{y}. \end{aligned} \tag{4.29}$$

Performing the gauge transformation in Eq. (4.6) with the function $\chi = -\boldsymbol{r}\cdot\boldsymbol{A}(0,t)$, one finds the new electromagnetic potentials, and a new interacting Hamiltonian

$$H_{int} = -\boldsymbol{\mu}\cdot\boldsymbol{B}(t) - \frac{1}{6}Q_{zx}\frac{\partial E_x}{\partial z}. \tag{4.30}$$

The first term represents a *magnetic dipole* interaction between the magnetic dipole moment $\boldsymbol{\mu}$ associated to the orbital angular momentum $L$ and the oscillating magnetic field $\boldsymbol{B}(t)$. The second one is relative to the *electric quadrupole* moment, that can be neglected in our case.

To obtain the complete description the spin angular momentum will have to be accounted for in the theory. Quite generally, the magnetic dipole moment is expressed as $\boldsymbol{\mu} = g\mu_B\boldsymbol{J}/\hbar$, where $\boldsymbol{J}$ is the relevant angular momentum operator and $g$ is the corresponding gyromagnetic factor, which is -1 for the electron orbital moment. $\mu_B = e\hbar/2m_e$ represent the Bohr magneton. For details of this calculation see [98]. In this case the Rabi frequency definition becomes

$$\Omega_{mag} \equiv \frac{\boldsymbol{\mu}_{eg}\cdot\boldsymbol{B}_0}{\hbar}, \tag{4.31}$$

in analogy with Eq. (4.13), with $\boldsymbol{\mu}_{eg} = \langle e|\boldsymbol{\mu}|g\rangle$ being the magnetic dipole moment of the transition between state $|g\rangle$ and $|e\rangle$. In the following we will refer to the transition dipole moment with $\boldsymbol{\mu}_{eg}$, and to the Zeeman shift of the transition frequency with $\delta\mu_{eg} = d/dB(\hbar\omega_0)$. Note here that both $\boldsymbol{\mu}_{eg}$ and $\delta\mu_{eg}$ depend on the magnetic dipole operator. However, while the former is an off-diagonal matrix element of the magnetic dipole operator evaluated between initial and final states, the latter is the difference between the expectation values $\langle e|\boldsymbol{\mu}_{\parallel}|e\rangle - \langle g|\boldsymbol{\mu}_{\parallel}|g\rangle$ of the longitudinal component of the magnetic dipole parallel to the bias Zeeman field. Furthermore, note that the RF transition under study, between Cr$|1\rangle$ and Cr$|2\rangle$, requires a change in the total spin projection onto the quantization axis $M_F$ by one unit, i.e. from -9/2 to -7/2. In this case the component of the magnetic dipole along the quantization axis $\mu_{\parallel}$ is zero, while the transverse component $\mu_{\perp}$ remains finite at all fields. This implies that the transition is only induced by the oscillating B field component perpendicular to the quantization axis.

The Cr$|1\rangle$ to Cr$|2\rangle$ transition at 1414 G has a $\omega_0 = 2\pi \times 240.152\,\mathrm{MHz}$, $\delta\mu_{eg}/h = 6.041\,\mathrm{kHz/G}$, and $\mu_{\perp}/h = 156.402\,\mathrm{kHz/G}$, calculated numerically by A. Ciamei.

## 4.2 Antenna: basic concept

An antenna is basically a conductor that allows electromagnetic energy to be radiated or received. To fully understand the antenna one has to solve the *Maxwell equations* which is not the scope of this thesis. Instead, I will show below in Sec. 4.4 a simple model of the antenna which allows to estimate the magnetic field of the antenna using the *Biot-Savart* law, see Eq. (4.32) below.

A time-varying electric current flowing through a conductor radiates a magnetic field from it, which in turn generates an electric $E$ field according to the Maxwell equations, neglecting feedback onto the source current. Conversely, time-varying electro-magnetic fields can induce a current within an electrical conductor. Although any conductor can behave as an antenna, optimised efficiency and particular directional characteristics can only be achieved with certain geometry and dimension of the conductor. In fact, optimum size and shape vary depending on the design frequency, and for the radiation field required, i.e. besides of the frequency $\nu$ and wavelength $\lambda = c/\nu$ also the polarization and directionality must be considered.

### 4.2.1 Near and far field

The field, generated by the antenna, can be characterized by two distinct regions: the near field and the far field, illustrated in Fig. 4.3. The intensity of the electric $E$ and magnetic $B$ fields in the far field diminishes as $\sim 1/r^2$, with $r$ the distance from the source, while in the near field, the intensity decreases more rapidly, typically following $\sim 1/r^3$.

The distinction between the near and far field is somewhat arbitrary and it depends on the size of the radiating component, and the dominant wavelength $\lambda$ produced by the source.

The near field pertains to regions in the proximity of the antenna conductors, typically within a distance of about one wavelength. Since the conductor is strongly coupled to everything within its near-field environment, also its impedance can be significantly modified compared to the same conductor placed in vacuum. Locally, the $E$- and $B$-field components can fluctuate significantly.

A notable example of a near-field effect is the variation of noise levels received by a pair of “rabbit ear” TV antennas, when a human body part is moved close to them. Similarly, the sound quality of an FM radio tuned to a distant station changes when a person moves around within arm’s length of the radio antenna.

The primary aim of conventional antennas is to facilitate wireless communication over long distances well into their far fields, and for most basic antennas, the intricate effects in the near field can be disregarded in radiation and reception calculations. This is not our case, because we need an antenna performing as good as possible in the closest near field region, also known as *reactive* region. This zone is roughly

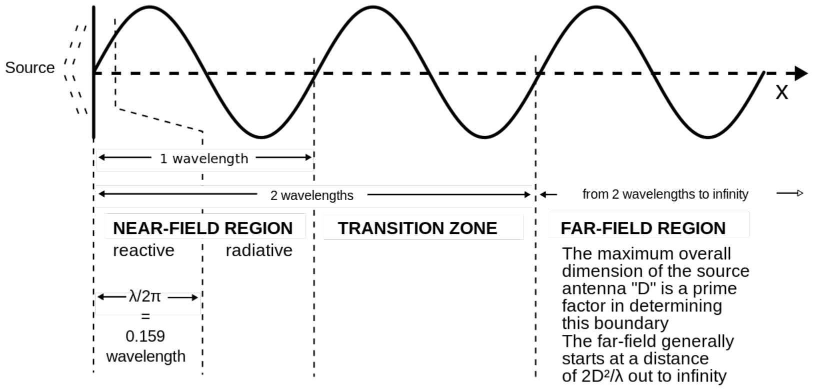

**Figure 4.3.** Field regions for antennas shorter than one-half wavelength of the radiation they emit, divided in *near-field* region (within a distance of $\lambda$) and the *far-field* region, beyond a distance of $2\lambda$. The intermediate zone is called *transition* zone. The near-field region is subdivided in two other sub-regions, named *reactive* and *radiative*, respectively, with a separation zone that is about a $\lambda/(2\pi)$ distance. Figure taken from [99].

within 1/6 of a wavelength of the nearest antenna surface. Our antenna, which needs to operate at 240 MHz, with a corresponding wavelength of $\lambda$ =1.25 m, fits into this classification, as we want to maximize the field at a distance of a few cm. At larger distances, in the *radiative* region, the antenna is not anymore disturbed by the back-action of nearby objects, but the electro-magnetic field is distorted by them. The intermediate region, between near- and far-field, approximately starts at one wavelength from the antenna, where the electric and magnetic parts of the radiated waves first balance out.

The far field of the antenna is characterized by transverse electric and magnetic fields with a constant ratio between the intensities of $E$ and $B$ fields known as the wave impedance of the medium.

## 4.3 Constraints for the antenna design

The task of our antenna is to induce a transition between two Zeeman levels of the hyperfine ground state of $^{53}$Cr. The broadest $s$-wave FB resonances of Li$|1\rangle$ and Cr$|1\rangle$ is at 1414 G. The Cr$|1\rangle$ and Cr$|2\rangle$ levels are separated by $h \times 240\,\mathrm{MHz}$.

Since at that magnetic field the Rabi frequency given by $\mu_\perp/h = 156.402\,\mathrm{kHz/G} \ll \mu_B/h = 1.4\,\mathrm{MHz/G}$ is relative small, the power driven by the antenna has to be sufficiently high in order to allow for sub-ms $\pi$-pulse time. In order to interact with chromium atoms, it is crucial that the field strength felt by the atoms is maximized, and that the antenna is positioned as close as possible to the atomic cloud.

In atomic physics experiments, ultracold gases are produced within an ultra-high vacuum chamber – typically made of glass or stainless steel – equipped with optical viewports that allow to shine in the various laser beams required for laser cooling and trapping. A sketch of the vacuum setup of our experiment is shown in Fig. 4.4, taken from Ref. [60], where many further details regarding our experimental setup can be found. Thermal atoms of lithium and chromium are produced in their respective

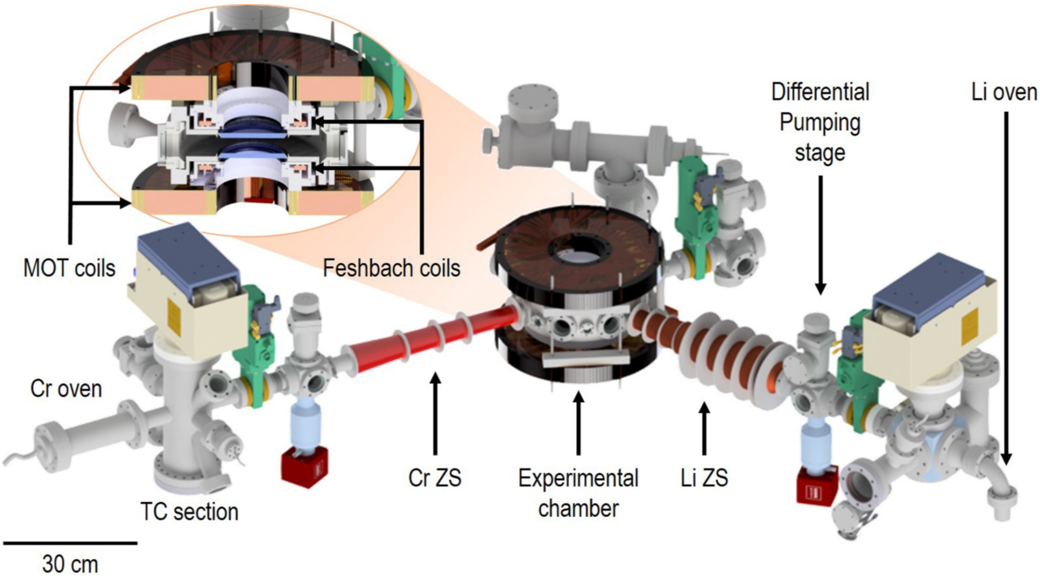

**Figure 4.4.** Overview of our vacuum setup. Two independent Zeeman Slower (ZS) lines connect the Li and Cr effusion cells to a custom spherical octagon chamber of radius 13 cm (manufactured by Kimball Physics, Inc.). In the horizontal x-y plane, the cell has 8 CF DN40 windows, spaced out by CF DN16 windows. Along the vertical z direction, two re-entrant CF DN200 windows with a wide clear aperture (radius 45 mm) ensure large optical access. Two large MOT coils, embedded within a resin structure, are fixed at the top and bottom of the experimental chamber, in a concentric configuration with respect to the smaller Feshbach coils, hosted within the re-entrant part; see section view on the top left. The large radius of our MOT coils ensures the merging of the two ZS field profiles with the MOT quadrupole radial profile (for more details, see Ref. [78]).

ovens and they undergo the initial phase of deceleration through two independent Zeeman slowers. Subsequently, they are collected and trapped in the center of the experimental chamber. Since the metal chamber would shield the RF signal we must place the antenna in front of a glass viewport. There are two options available: either behind the CF40 or CF16 viewports, positioned on the chamber plane, or close to one of the two CF200 re-entrant windows along the vertical axis. Due to the chamber dimensions, given by a diameter of 30 cm in the horizontal plane and by an overall height of 8 cm, the best solution is to exploit the re-entrant windows, along the vertical axis, as they allow for the closest access to the atoms (see scheme in Fig. 4.5). When the antenna is placed on top of the glass viewport, indeed, it is only 22.5 mm away from the atom position. Our re-entrant windows have a clear aperture with a diameter of 90 mm, and both the MOT-$z$ beam and the two ODT crossed beams pass through the viewport center. The MOT beam, which has a diameter of approximately 25 mm, and provides the major constraint for the choice of the physical dimensions of the RF antenna (see Fig. 4.5(a)). We use the banana-shaped antenna design proposed by Scazza *et.al.*, [97], which is a very good solution, both to tackle the physical limits of the antenna and, at the same time, to maximise the magnetic field in the precise area where the atoms are located. Additionally, this

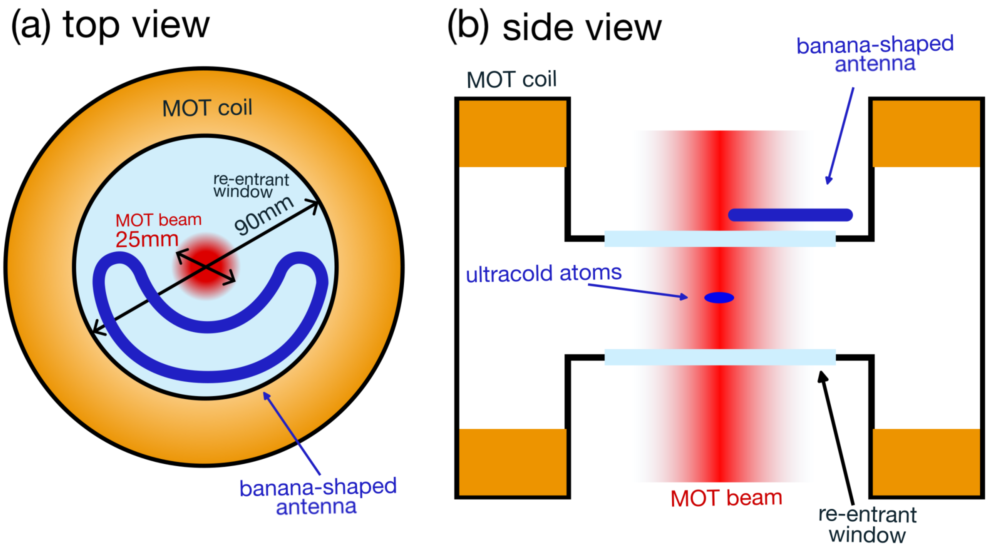

**Figure 4.5.** **(a)** top view of the re-entrant window. MOT-$z$ and crossed beams pass through its center. The crossed BODT beams are smaller than the MOT beams and therefore not shown. The banana-shaped antenna is positioned right next to the laser beams in a free region. **(b)** side view of the vacuum chamber scheme.

design minimizes the vertical field component which does not contribute to the Rabi oscillation frequency but creates unwanted modulations of the offset field.

## 4.4 Antenna magnetic field radiation

In order to simplify the calculation of the magnetic field radiated from the banana-shaped antenna, it is convenient to schematize its geometry as 2 half-loops of inner (outer) radius $R_1$ ($R_2$) connected by two linear wires, see sketch in Fig. 4.6. Furthermore, let's assume the antenna to lay in the $z = 0$ plane, and that the loop center is located at $x = y = 0$. We then evaluate the radiated field at $x = y = 0$, at a vertical distance $z_0 = -22.5\,\mathrm{mm}$ below the plane of the antenna, i.e. at the atom position. To this end, we start by writing the *Biot-Savart law*, where the magnetic field is expressed as a line integral, evaluated over the path $C$ in which the electric current $I$ flows:

$$\mathbf{B}(\mathbf{r}) = \frac{\mu_0}{4\pi} \int_C \frac{I \mathbf{d}\boldsymbol{\ell} \times \mathbf{r}'}{|\mathbf{r}'|^3}. \tag{4.32}$$

where $\mathbf{d}\boldsymbol{\ell}$ is a vector along the path $C$, and its magnitude is the length of the differential element of the wire in the direction of conventional current; $\boldsymbol{\ell}$ is a point on the path $C$; $\mathbf{r}' = \mathbf{r} - \boldsymbol{\ell}$ is the vector from the wire element ($\mathbf{d}\boldsymbol{\ell}$) at point $\boldsymbol{\ell}$, to the position in space at which the field is computed ($\mathbf{r}$), and $\mu_0$ is the vacuum magnetic permeability.

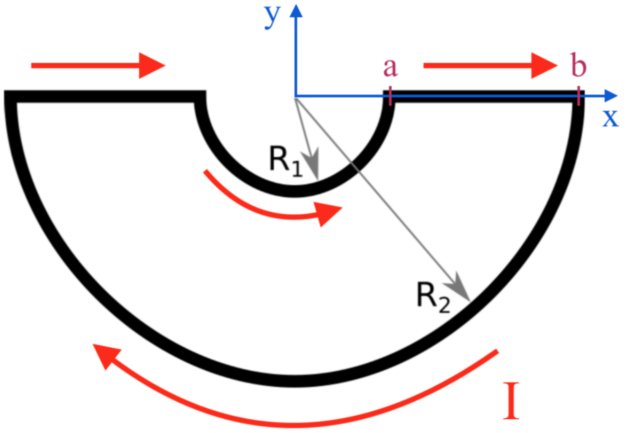

**Figure 4.6.** Schematic view of the banana-shaped antenna coil. $R_1$ and $R_2$ are the inner and the external radius, respectively; $a$ and $b$ denote the extremes on the x-axis of the straight wire segment, useful for calculating the magnetic field; $I$ is the current.

### 4.4.1 B field for a finite straight wire

We assume to have a straight wire along the $x$-axis bounded by $a$ and $b$, as shown in Fig. 4.6. Since the $\mathbf{d}\boldsymbol{\ell}$ element lies on that axis, and since we calculate the field at a point along the $z$-axis, the vector product at the nominator of Eq. (4.32) is non-zero only for the $y$ component of the $B$ field:

$$B_y^{wire}(z) = \frac{\mu_0 I}{4\pi} \int_a^b \frac{r}{(x^2+z^2)^{3/2}} dx = \frac{\mu_0 I}{4\pi r} \left( \frac{b}{\sqrt{b^2+z^2}} - \frac{a}{\sqrt{a^2+z^2}} \right), \tag{4.33}$$

whereas $B_x^{wire} = B_z^{wire} = 0$ for all $z$ values. For the second straight wire on the negative $x$-axis side, replacing $a \to -b$ and $b \to -a$, one finds that the magnitude and direction of the field is the same.

### 4.4.2 B field for a half loop wire

Let us consider now a wire forming a half-loop (HL) of radius $R$ on the $x$-$y$ plane, in which flows a constant current $I$. In this case, only the $x$ component is zero, $B_x^{HL} = 0$. The other two components are instead given by:

$$B_y^{HL}(z) = \frac{\mu_0 I}{2\pi} \frac{R\,z}{(R^2+z^2)^{3/2}} \tag{4.34}$$

$$B_z^{HL}(z) = \frac{\mu_0 I}{4} \frac{R^2}{(R^2+z^2)^{3/2}} \tag{4.35}$$

### 4.4.3 Magnetic field calculation

For our system, the bias magnetic field generated by both pairs of MOT and “Feshbach” coils, see Fig. 4.4, points along the $z$-axis. For this reason, we want the

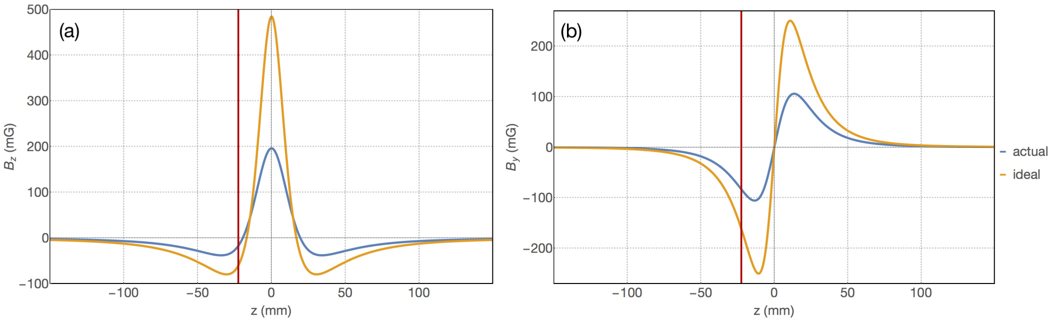

**Figure 4.7.** Vertical **(a)** and transversal **(b)** components of the field generated by the RF antenna as a function of the vertical position $z$. Red lines mark, in each panel, the position of the atoms at z = -22.5 mm. Two configurations of the antenna are plotted: orange (blue) with $R_1 = 15\,\text{mm}$ (22 mm) and $R_2 = 40\,\text{mm}$ (35 mm) corresponding to the ideal (actual used) configurations given the constraints discussed in Sec. 4.3. The curves are calculated with Eqns. (4.33)–(4.35) using a current of 3.75 A.

field component generated by our antenna along $z$ to be 0, so that the RF field does not affect the net bias field value, experienced by the atomic sample, and maximizes the circularly polarized $B$-field component inducing the Rabi frequency of the RF transition. Along the two concentric half-loop wires, one has a current that has equal magnitude, but opposite sign, see Fig. 4.6. This means that there exists a position $z$ where the vertical component of the $B$-field is zero. As already seen, the contribution along the bias field direction $\hat{z}$ from the two straight wires is zero. We thus search for the right configuration of the parameters – i.e. inner and outer radii of the antenna – so that $B_z$ is zero at the position of the atomic cloud, whereas the transverse component $B_y^{tot}$ is maximized. The overall magnetic field is easy to calculate at this point: we need to sum the two concentric half loops with two different radii, and two straight wires as shown in Fig. 4.6. Among all possible solutions, the *ideal* case that best fits our technical constraints, and that simultaneously allows us to maximize the $B_y^{tot}$ field component while minimizing the $B_z$ component at the atom position, is for $R_1^i = 15\,\text{mm}$ and $R_2^i = 40\,\text{mm}$, respectively. However, during the first tests of the antenna we have reduced the overall loop size since we had problems to reach 240 MHz with the ideal dimensions. The final antenna still has the smaller dimensions of $R_1^a = 22\,\text{mm}$ and $R_2^a = 35\,\text{mm}$ and generates about half of the ideal B-field.

The two field components, of the ideal (orange) and actual case (blue), are plotted in Fig. 4.7, assuming a current of 3.7 A. We can focus on the field magnitude at the atom position, which is highlighted on the graphs by the red line. With this ideal (actual) radii configuration, we have a small $B_z$ component of 60 mG (17 mG), and a sufficiently large $B_y$ of 162 mG (83 mG).

## 4.5 Matching circuit

In order to maximize the $B$-field radiated by the RF antenna, one has to maximize the power transferred from the RF generator towards the antenna. If the impedance of the antenna does not match the impedance of the RF amplifier, then a significant

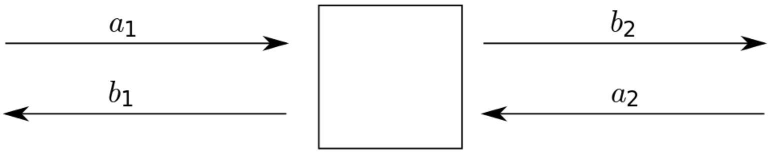

**Figure 4.8.** Scheme of a two-port network.

amount of power can be reflected back, leading to a small signal on the atoms and possible damage to the RF amplifier. Therefore, a matching circuit needs to be inserted between the RF amplifier and the antenna, which helps to minimize these reflections and to ensure efficient transfer of power between the components.

The reflection coefficient $\Gamma$ quantifies the ratio of the reflected root-mean-square (rms) voltage $V_r$ over the rms input voltage $V_i$:

$$\Gamma = \frac{V_r}{V_i}. \tag{4.36}$$

This can be recast in the following forms:

$$\Gamma = \frac{Z_L - Z_0}{Z_L + Z_0} = \frac{z-1}{z+1}. \tag{4.37}$$

with $Z_L$ denoting the load resistance and $Z_0$ the characteristic impedance of the system (for us $Z_0 = 50\,\Omega$), and $z$ is the relative impedance, given by $z = Z_L/Z_0$.

The impedance of the load, $Z_L$, may be a complex number, implying that there could be a phase shift between the reflected signal and the input signal. When $Z_L$ is equal to the characteristic impedance of the system, $Z_0$, then the reflection coefficient $\Gamma$ is zero, meaning that no reflection will occur, and all the power will be transmitted. Therefore, in order to ensure efficient transmission of an RF signal from one network to another, the matching condition, $Z_L = Z_0$, has to be fulfilled.

An alternative way to describe this is through the $S$-matrix [100], typically used in the field of signal processing and communication engineering to describe the relationship between the input and output signals of a linear system. By measuring the $S$-matrix parameters, it is possible to characterize the behavior of a network under different impedance conditions. For a two-port model, shown in Fig. 4.8, the network is described by a 2×2 square matrix of complex numbers: $a_1$ is the input voltage across port 1; $b_1$ is the reflection voltage from port 1; $b_2$ is the output voltage across port 2; $a_2$ represents the incoming reflection voltage from a following circuit.

The relationship between the reflected and incident waves through the $S$-parameter matrix is then given by [101]:

$$\begin{pmatrix} b_1 \\ b_2 \end{pmatrix} = \begin{pmatrix} S_{11} & S_{12} \\ S_{21} & S_{22} \end{pmatrix} \begin{pmatrix} a_1 \\ a_2 \end{pmatrix}, \tag{4.38}$$

yielding

$$b_1 = S_{11}a_1 + S_{12}a_2 \tag{4.39}$$

and

$$b_2 = S_{21}a_1 + S_{22}a_2. \tag{4.40}$$

Each equation establishes the connection between the incident and the reflected waves at the network ports 1 and 2, in terms of the network $S$-parameters. If port 2 is terminated onto a load identical to the system impedance $Z_0$, by the maximum power transfer theorem [102], $b_2$ will be totally absorbed, thus making $a_2 = 0$. In that way is easy to determinate

$$S_{11} = \left.\frac{b_1}{a_1}\right|_{a_2=0} \qquad S_{21} = \left.\frac{b_2}{a_1}\right|_{a_2=0} . \tag{4.41}$$

Similarly, if port 1 is terminated on the system impedance, then $a_1 = 0$, giving

$$S_{12} = \left.\frac{b_1}{a_2}\right|_{a_1=0} \qquad S_{22} = \left.\frac{b_2}{a_2}\right|_{a_1=0} . \tag{4.42}$$

The complex 2-port $S$-parameters have the following generic descriptions: $S_{11}$ is the input port voltage reflection coefficient, $S_{12}$ is the reverse voltage gain, $S_{21}$ is the forward voltage gain, and $S_{22}$ is the output port voltage reflection coefficient. In the characterization of a network $S$-parameters, measuring $S_{11}$ and $S_{22}$ can be accomplished by terminating the circuit with the characteristic impedance $Z_0$, and observing the reflected signal. On the other hand, obtaining $S_{21}$ and $S_{12}$ requires to measure the transmission of the network.

In the field of antenna engineering, it is common practice to use the Smith chart as a graphical tool for analyzing and designing transmission lines and matching circuits. It is a polar plot that allows to easily visualize the complex impedance of a transmission line, or load, at any frequency. The chart provides a way to quickly determine the correct matching network to transform the impedance of the load to the characteristic impedance of the transmission line and, ultimately, to the impedance of the antenna.

The Smith chart has two simultaneous readings, as illustrated in Fig. 4.9. It contains the relative impedance $z$ and, simultaneously, the reflection coefficient $\Gamma$. Knowing a certain impedance load, its normalized value $z$ can be placed as a point on the Smith chart using the circles emphasized in the left panel of Fig. 4.9. The distance between this point and the center of the chart represents the $\Gamma$ value. From here, by adding elements such as resistors, inductors or capacitors, one can move along the curves to reach the centre of the chart, which corresponds to $z = 1$. As shown in Fig. 4.9, these lines can be subdivided in two types. First, in blue, we find the constant resistance circles, in which the real part of the impedance is kept constant. One can move along these circles clockwise, adding a series impedance. Otherwise, one can move counter-clockwise by adding a series capacitor. In green are represented the other kind of lines, namely circumferential arcs with constant reactance. Along these lines one can move by adding a purely resistive component. The matching is achieved when the centre of the chart for a given frequency is reached. We use the Smith chart in Fig. 4.17(c) to display the result of the simulation of the final antenna design.

### 4.5.1 Matching examples

In the following, I illustrate a few examples of impedance matching, useful to understand our strategy to optimize the matching circuit for the RF antenna.

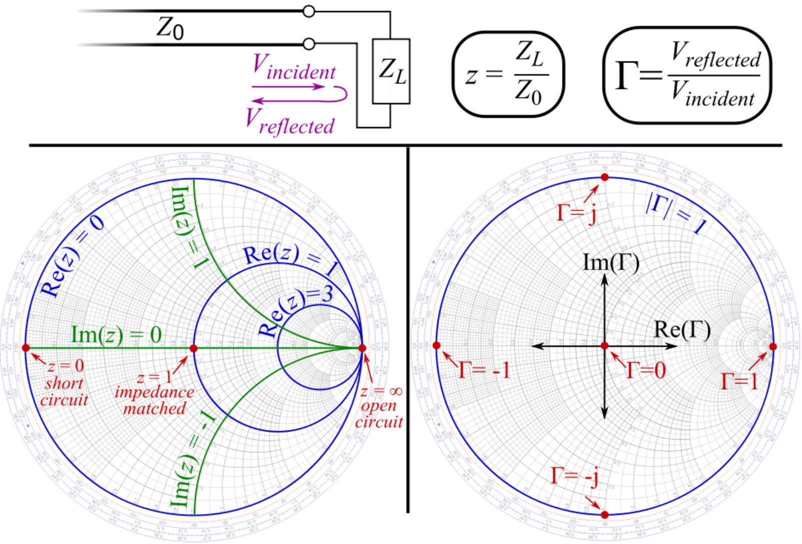

**Figure 4.9.** Smith chart showing the normalized impedance $z = \frac{Z_L}{Z_0}$ (left) with $Z_L$ the load impedance and $Z_0$ the characteristic impedance of the system, and the reflection coefficient Γ (right). See text for details. Figure taken from [103].

### Inductive impedance load

First let's consider the case of a pure inductive load, for which the impedance is purely imaginary $Z_L = j\omega L$, where $j$ is the imaginary number commonly used in the field of electronics. In the complex plane $Z_L$ is represented by the red point on the positive side of the imaginary axis, see Fig. 4.10(a). In order to achieve impedance matching at 50 Ω (yellow point), additional elements must be incorporated, to shift the impedance towards the 50 Ω point on the real axis. A straightforward solution is to insert a capacitor in series with the load, which provides an impedance of $Z_C = 1/(j\omega C)$ and moves the impedance closer to the real axis. To achieve the desired impedance, the condition $j\omega L = j/(\omega C)$ must be satisfied. Finally, a series resistor of 50 Ω can be added to move along the real axis, resulting in a fully matched circuit. Since our antenna is essentially a wire loop, its impedance can be mainly represented as an inductor and we use a capacity to make its impedance real valued.

### Capacitive impedance load

A similar strategy is applied when the load is a capacitor, for which the impedance $Z_C$ is purely imaginary, but with $\mathrm{Im}[Z_C] < 0$, see Fig. 4.10(b). In order to achieve impedance matching in this case, an inductance can be added in series to shift the impedance along the imaginary axis, followed by a resistor to reach the desired 50 Ω impedance point on the real axis.

### Real impedance load

Another standard case of impedance matching arises when the load impedance is real and small, e.g. $Z_L = 8\,\Omega$, like it is typical for a loud speaker, and needs to be matched to the characteristic impedance of the transmission line, $Z_0 = 50\,\Omega$, see

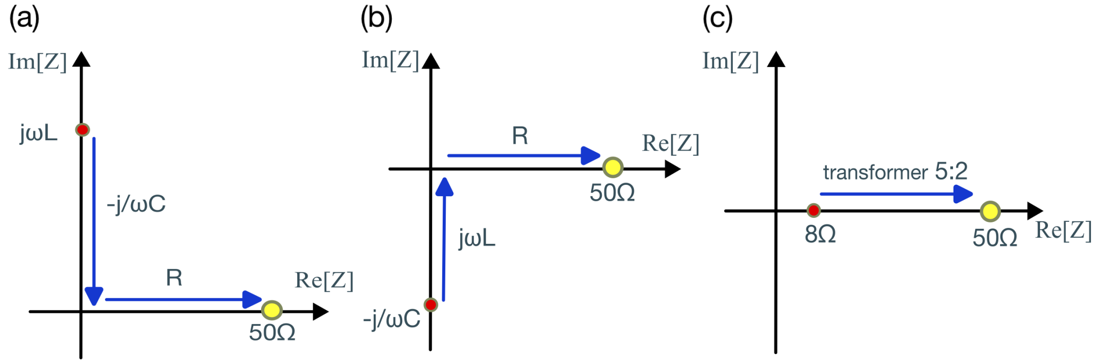

**Figure 4.10.** Three examples of matching on the impedance complex plane. (a) Starting from a purely inductive impedance (red dot), adding a capacitor and a $50\,\Omega$ resistor in series (blue arrows) moves the impedance to $Z_0 = 50\,\Omega$ (yellow point). (b) Similar to (a), starting from a pure capacitive impedance, adding an inductor and resistor in series moves the impedance to $Z_0$. (c) Starting from $8\,\Omega$ adding a resistor of $42\,\Omega$ gives perfect matching but at the cost of reduced power on the load. Adding a $5:2$ transformer in series to the $8\,\Omega$ load does the same but without loss of power.

Fig. 4.10(c). A first option is to add another resistor, with a value of $R_m = 42\,\Omega$, for impedance matching. However, this approach is not ideal, as only a small fraction of the power is delivered to the load. Indeed, denoting the power on the load as $P_L$ and the total power given by the generator as $P_{tot}$, one can easily find that

$$\frac{P_L}{P_{tot}} = \frac{P_2}{P_1} = \frac{V_2\,I_2}{V_1\,I_1} = \frac{V_2}{V_1} = \frac{V_1\,8/50}{V_1} = \frac{8}{50} = 0.16. \tag{4.43}$$

Here $V_{1,2}$ and $I_{1,2}$ are, respectively, the voltage and the current at the input (1) and at the output (2) of the matching network, and in Eq. (4.43) we have used $I_2 = I_1$ and $V_1 = (Z_L + R_m)I_1 = I_1\,50\,\Omega$ and $V_2 = Z_L\,I_1$. When the impedance $Z_L > Z_0$ a resistor in parallel to the load can be employed for matching, but again only a fraction of the power is transmitted to the load. A better method for matching uses a transformer, which in the ideal case allows to transmit the full power to the load, as discussed in the following.

### Transformer

Let's consider the case of an ideal transformer (Fig. 4.11), which consists of two coils wound on a shared magnetic core, ensuring efficient magnetic coupling between them. In this ideal scenario, the output voltage $V_2 = n\,V_1$ and current $I_2 = I_1/n$ of the transformer are functions of the winding ratio $n = N_2/N_1$, where $N_1$ and $N_2$ are the numbers of windings in the primary and secondary coil, respectively. For $n > 1$, the transformer is called a *step-up* transformer, and the voltage is increased while the current is decreased. Conversely, for $n < 1$, the transformer is called a *step-down* transformer, and the voltage is decreased while the current is increased. The input impedance of a transformer is

$$Z_1 = \frac{V_1}{I_1} = \frac{V_2}{I_2\,n^2} = \frac{Z_2}{n^2}, \tag{4.44}$$

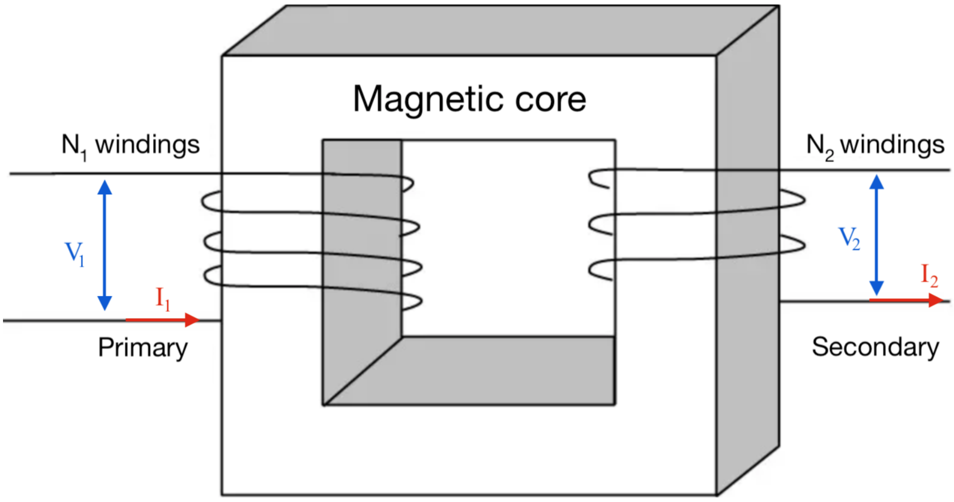

**Figure 4.11.** Sketch of an ideal transformer. Two coils, with $N_1$ and $N_2$ windings respectively, are wound on the same magnetic core. It allows perfect matching without loss of power in resistive elements.

where $Z_1$ and $Z_2$ are the input and output impedances, respectively. Therefore, a transformer can be used to match the impedance between two circuits. A step-up transformer ($n > 1$) can be used to match $Z_L > Z_0$ and a step-down transformer ($n < 1$) can be used to match $Z_L < Z_0$. For our example above in Fig. 4.10(c), to match the $8\,\Omega$ with $50\,\Omega$ we can use a step-down transformer with $n = \sqrt{8/50} = 0.4$. Thus using a 5:2 transformer for impedance matching instead of a resistor, has the clear advantage that the power on the load is the same as on the input, ensuring maximum power transfer efficiency. In the case of our antenna, after we have added a matching capacitor, we use a step-down transformer to bring the small remaining real part to $50\,\Omega$. This has the additional advantage that the current and thus the magnetic field can be further increased. However, a disadvantage of using a classical transformer with magnetic coupling is that, for high frequencies, the spurious impedance of the transformer cannot be neglected, and it can be challenging to have high power transformers operating at high frequencies. One solution is discussed in the following.

### 4.5.2 Quarter-wave transformer

Achieving the required ratio of the number of turns for our low-impedance antenna, of about $1\,\Omega$, with a step-down transformer, $n = \sqrt{1/50} \simeq 1/7$, would require seven times more windings on the primary side than on the secondary one, leading to a large transformer with a significant spurious impedance. Additionally, in order to handle our required power of up to 100 W, the transformer would require thick wires and a sizeable construction, further increasing the spurious impedance. At high frequencies, such magnetically coupled “classical” transformer become impractical. The *quarter-wave transformer*, see Fig. 4.12(a), is a highly effective solution to the aforementioned issue. This design consists of a short section of transmission line, which can be a coaxial cable, that is a quarter of the wavelength at the desired

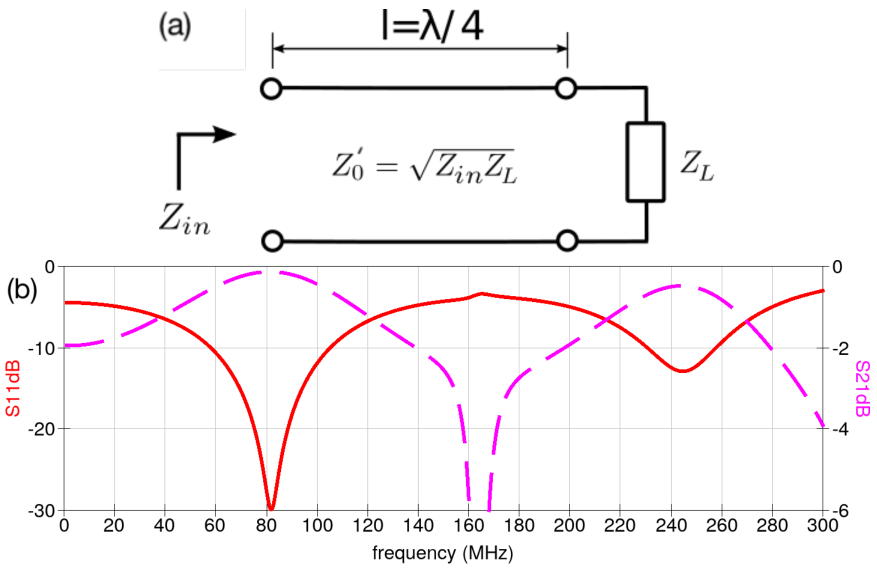

**Figure 4.12.** **(a)** Impedance-matching using a quarter-wavelength transmission line. Figure taken from [104]. **(b)** Simulation with QUCS [105] of $S_{11}$ (red solid, left axis) and $S_{21}$ (magenta dashed, right axis) of a quarter-wavelength transmission line vs. frequency. The quarter-wave condition is fulfilled for 80 MHz and 240 MHz ($Z_0' = 25\,\Omega$, $Z_L = 12.5\,\Omega$, $l = 0.656\,\mathrm{m}$, $v_F = 0.7$).

frequency. This section of the transmission line is connected between the load and the source, and it acts as an impedance transformer. This design is simple, easy to implement, and can handle high power. However, it works only at the design frequency.

Let's consider a certain transmission line with a characteristic impedance of $Z_0'$ connected to an impedance load $Z_L$. The general expression for the input impedance of a lossless transmission line is [104]

$$Z_{in}(l) = Z_0' \frac{1 + \Gamma e^{-i2kl}}{1 - \Gamma e^{-i2kl}} \tag{4.45}$$

where $k = 2\pi/\lambda$ and $l$ is the length of the transmission line. When $l = \lambda/4$

$$2\,k\,l = 2\,\frac{2\pi}{\lambda}\,\frac{\lambda}{4} = \pi \tag{4.46}$$

Subsequently,

$$Z_{in}\left(\frac{\lambda}{4}\right) = Z_0' \frac{1 + \Gamma e^{-i\pi}}{1 - \Gamma e^{-i\pi}} = Z_0' \frac{1 - \Gamma}{1 + \Gamma} = \frac{(Z_0')^2}{Z_L}, \tag{4.47}$$

where we have used the definition of the reflection coefficient Γ.

This means that, similar to the classical transformer, the load impedance $Z_L$ can be adjusted to match $Z_{in} = Z_0$ by selecting the suitable length and characteristic impedance $Z_0'$ of a transmission line. Since the speed of light in the transmission line $c_{line}$ is reduced with respect to the speed of light in vacuum $c_{vac}$ by the velocity factor $v_F = c_{line}/c_{vac} \approx 1/\sqrt{\varepsilon_r}$ with $\varepsilon_r$ the dielectric constant of the medium, the calculation of the length of the quarter-wavelength transformer must take this into

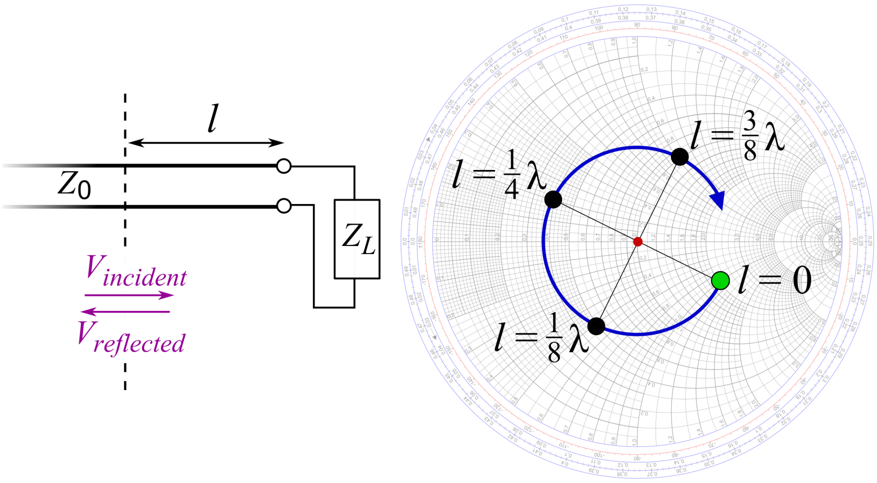

**Figure 4.13.** Quarter-wave transformers illustrated in an impedance Smith chart. When observing a load through a lossless transmission line with a certain length $l$, the normalized impedance undergoes changes as $l$ increases, which can be represented as a blue circle on the chart. When $l = \lambda/4$, the normalized impedance is mirrored around the center of the chart. Figure taken from [103].

account. Note that the quarter wavelength condition is even fulfilled for any odd multiple of $\lambda/4$, i.e. $l = (2N + 1)\lambda/4$ with $N$ a positive integer, see Fig. 4.12(b).

A coaxial cable can be considered as a transmission line, with a characteristic impedance $Z_0'$, approximately equal to $Z_0' \sim \sqrt{L/C}$ where $L$ is the series impedance and $C$ the parallel impedance of an infinitely small section of the cable [106]. By selecting appropriate materials and inner diameter $d$ and outer diameter $D$ for the coaxial cable, the characteristic impedance $Z_0'$ can be adjusted to the required value, according to the following formula [107].

$$Z_0' \sim \frac{138\Omega}{\sqrt{\varepsilon_r}} \log_{10}\left(\frac{D}{d}\right). \tag{4.48}$$

Neglecting any losses, the current on the load can be determined from the power $P$, which is related to the current $I_1$, and characteristic impedance $Z_0$, by $P = Z_0 I_1^2$. Similarly, the current $I_2$, and load impedance $Z_L$, are related by $P = Z_L I_2^2$. It follows that the ratio $I_2/I_1 = \sqrt{(Z_0/Z_L)} = Z_0/Z_0'$. This implies that, for $Z_0 > Z_0'$, the current is increased while the voltage, calculated in the same way, is decreased by the same factor. This behavior is reminiscent of the transformer described earlier, and is the reason why this device is known as a quarter wave impedance transformer.

The quarter-wave impedance transformer is a highly effective solution for high-frequency applications, characterized by low losses and the ability to handle high power. However, the length of the transformer must be carefully chosen to match the design frequency (see Fig. 4.13).

To match the low-impedance antenna and to enhance the current flowing through the antenna, we implemented a quarter-wave transformer as a step-down transformer. In order to determine the appropriate length and characteristic impedance of the transformer, we performed a simulation considering also the matching circuit and antenna parameters.

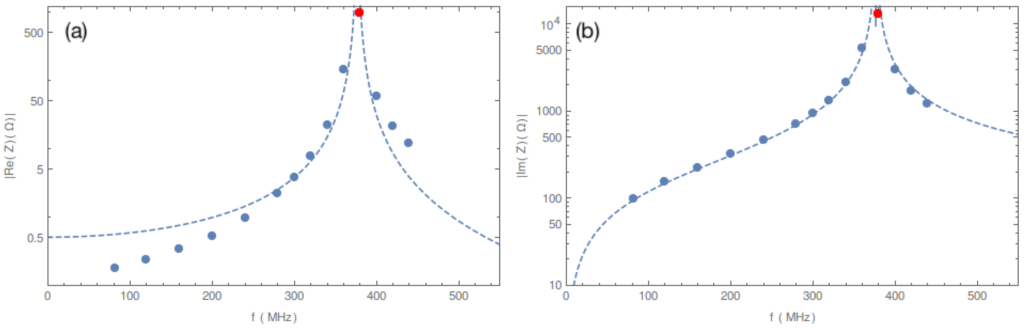

**Figure 4.14.** Numerical simulation (performed by A. Trenkwalder with *COMSOL Multiphysics*) of the real part **(a)** and imaginary part **(b)** of the impedance (blue dots) of a realistic banana-shaped antenna vs. frequency. The result is fitted with a simple resonance model containing a resistor of $R = 0.5\,\Omega$ in series to an inductor $L = 180\,\mathrm{nH}$ and parallel to both a capacitor of 1 pF. The resonance frequency is about 375 MHz. Antenna dimensions are $R_1 = 15\,\mathrm{mm}$, $R_2 = 42.5\,\mathrm{mm}$, wire diameter = 1 mm, input wire connection radius = 3 mm. Wire material is copper and the antenna is immersed in a sphere of radius R = 1.5 m filled with air bounded by a 0.5 m thick perfectly matched layer which avoids reflections and simulates the far field region. The red data point close to the center of the resonance was excluded from the fit.

### 4.5.3 Impedance of the antenna and its self-resonance

In the low-frequency regime, our antenna can be approximated as a *RLC* circuit, with a resistor and an impedance in series, and a capacitor in parallel. Using numerical simulation results of the antenna provided by *COMSOL Multiphysics*, my colleague A. Trenkwalder has fitted the characteristic parameters of a realistic banana-shaped antenna with the ideal dimensions and has obtained a low ohmic resistance of $0.5\,\Omega$, an inductance of 180 nH, and a capacitance of 1 pF, see Fig. 4.14.

Exploiting the equation [102]

$$\nu = \frac{1}{2\pi\sqrt{LC}}, \tag{4.49}$$

we get the resonance frequency of 375 MHz. At this frequency, the antenna radiates strongly, and the real and imaginary parts of its impedance approach infinity. This makes it difficult to match the antenna and one has to work below the resonance. Additionally, small stray capacitances and changes in the environment can shift the resonance, limiting how close one can work to the resonance. At 240 MHz, the impedance of the antenna is approximately $1\,\Omega + j\,500\,\Omega$.

Before discussing further details, we summarize the applied matching concept for our antenna: a matching capacitor is added to compensate for the inductive part, following the concepts illustrated in Sec. 4.5.1. A quarter-wave impedance tranformer is used as step-down transformer to match to $50\,\Omega$ and to transmit all power into the antenna, as previously shown in Sec. 4.5.1. By doing so, the magnetic field generated by the antenna is directly increased.

There are several problematic details that need to be addressed for the design of the antenna. First, the matching capacitor would need to be very small to reach the relatively high frequency of 240 MHz. Second, it is important to ensure that the

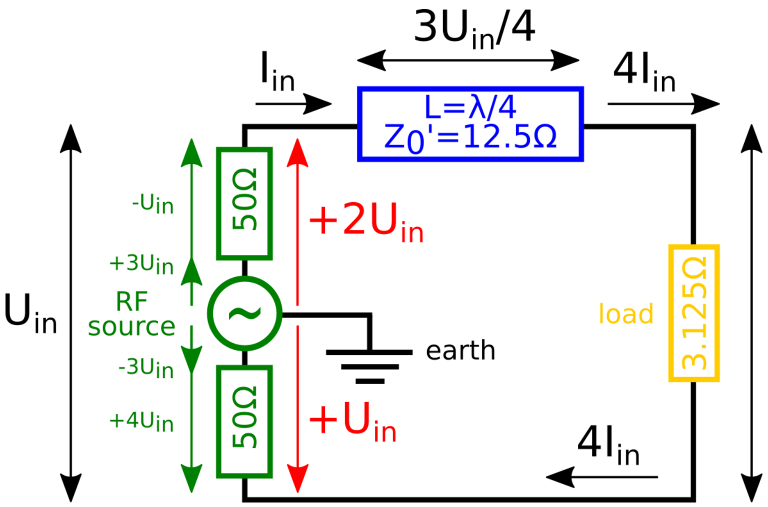

**Figure 4.15.** A common mode voltage (sum of red voltages) is generated when a quater-wave transformer (blue) and the load (orange) are directly connected to the RF source (green).

antenna is radiating and not the entire circuit, which can be challenging to achieve. These issues need to be resolved to optimize the performance of the antenna and achieve the desired results.

### 4.5.4 Symmetric matching design

Fig. 4.15 schematically shows what happens when one connects the load (idealized antenna as $3.25\,\Omega$ resistor, orange), and the quarter-wave transformer (blue) directly to the RF source (green). Since in the Fig. 4.15 we have $Z_0' = Z_0/4$, the transformer increases the input current $I_{in}$ by a factor of 4 and the input voltage $U_{in}$ is reduced by a factor of 4 over the load, see Sec. 4.5.2. This circuit is problematic since the current going out of the source is not the same as coming back into the source. Assuming that the RF source gives a symmetric voltage before the $50\,\Omega$ internal source resistances, it is easy to show, that the voltages on the input ($+2\,U_{in}$, red) and output ($+\,U_{in}$, red) of our circuit are not symmetric around earth. The sum of the two voltages is referred to the “common-mode voltage” ($+3\,U_{in}$ here) and when it is non-zero causes that the entire circuit starts to radiate. This “electromagnetic interference” (EMI) has to be avoided to prevent other electronic devices to pick up noise and to protect humans – and other living beings – from harmful radiation. In the balanced case, the source requires only $3 \times U_{in}$ to drive the circuit, while in the shown case it requires twice the voltage and thus twice the power to provide the same current. To avoid EMI and for better efficiency, a symmetric – also called “balanced” – design must be employed such that the currents going out of the source and returning are the same. To achieve this, a second matching circuit is placed after the antenna. It includes a step-up transformer that decreases the current and increases the voltage. In addition, a high-power $50\,\Omega$ resistor is positioned near the RF source to act as a dummy load and absorb most of the power. Note that even in the balanced case stray capacities, or an improper connection to ground on

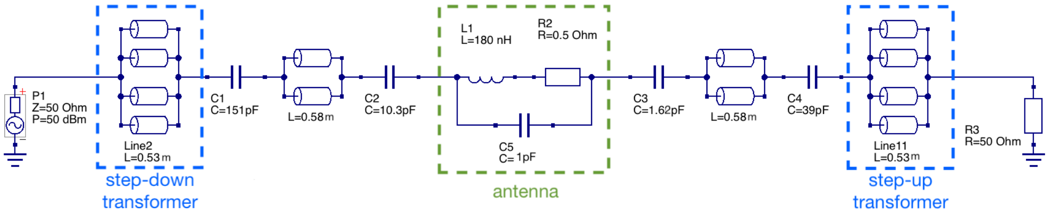

**Figure 4.16.** Scheme of the antenna matching circuit.

the antenna, can cause unwanted currents going back to the source avoiding the second matching circuit. This leads in a similar way to imbalanced currents and a common-mode voltage causing EMI. Special designs exist to avoid such problems (for example see Ref. [108]).

### 4.5.5 QUCS simulation

Once the design of the whole circuit was conceptually devised, and rough estimates for the various components were made, we used the *QUCS* software [105] to simulate the specific details of the antenna setup.

To solve the issue of the small matching capacity, we split the capacitor into 2 larger capacities in series with a second coaxial cable transmission line in-between. Varying the length of this transmission line the impedance of the antenna is rotated into a more favorable regime around the center of the Smith chart, see right panel in Fig. 4.13. This gives another degree of freedom which we numerically optimize for perfect matching.

Fig. 4.16 shows a schematic representation of the final setup I implemented. Using QUCS, I varied the cable lengths and capacitance values in order to have a good matching for our frequency of interest, 240 MHz. The results of the simulations are displayed in Fig. 4.17. Panel (a) shows the reflection coefficient $S_{11}$, represented by the solid red line, and the transmission coefficient $S_{21}$, represented by a dashed magenta line, as a function of the RF frequency. Fig. 4.17(b) shows the current flowing into the antenna (blue line) and the voltage across the antenna (magenta line). Panel (c) shows the reflection coefficient $S_{11}$ in the Smith chart.

The data presented in all panels unambiguously indicate that the design is optimized for a good impedance matching and high current delivery to the antenna at a frequency of 240 MHz.

## 4.6 Realization

Once the entire setup was planned, and its performance was optimized with *QUCS*, I proceeded to realize both RF antenna and the whole matching circuit.

Figure 4.18 displays a photo of the antenna. It is mounted on a Polypropylene tube (80 mm diameter, 2.4 mm wall thickness). On the mid-top of the photo one can see the prototyping board (green) which we used to place the adjustable capacitor and which connects to the second transformer.

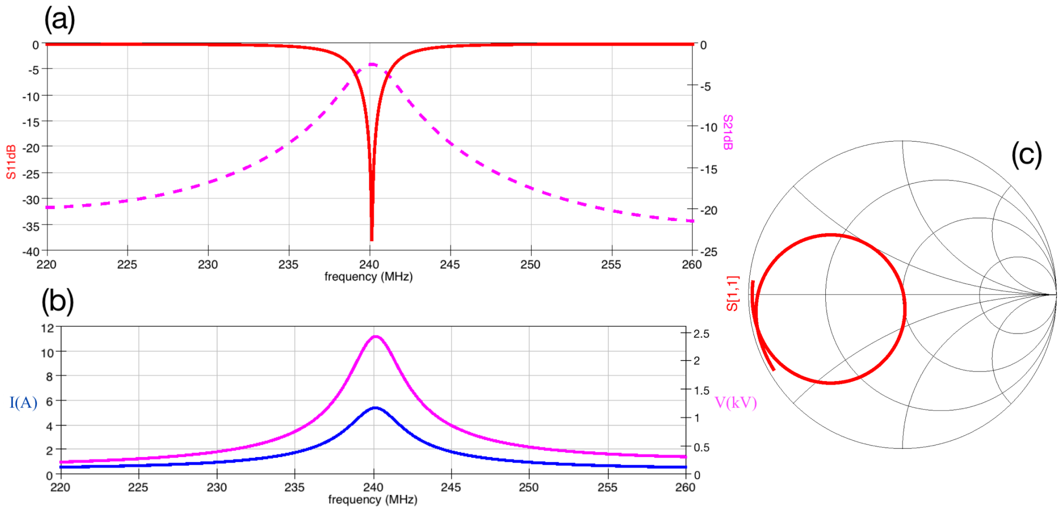

**Figure 4.17.** Results of the simulation of the antenna circuit made with the *QUCS* software: **(a)** solid red line and dashed magenta line represent the reflection coefficient $S_{11}$ and the transmission coefficient $S_{21}$ respectively, as function of frequency; **(b)** current (blue line) and voltage (magenta line) on the antenna as function of the frequency; **(c)** reflection coefficient $S_{11}$ plotted in the Smith chart. For this simulation was used the circuit in Fig. 4.16, with a RF power of 100 W.

For the antenna body we use a rectangular copper wire with cross section of 3.2 mm × 1.5 mm. A thick wire and short feeding connections are essential to keep the inductance low to reach high frequencies and to be able to use not too small capacitors. The antenna is fixed and soldered to an electrical prototyping board on which the capacities $C_2$ and $C_3$ are placed with $C_3$ adjustable from 4-20 pF. As already mentioned, the second transmission line (length 0.58 m, $Z_0' = 25\,\Omega$ created by two parallel coaxial cables of the same type as for the quarter-wave transformer) is placed between the two matching capacitors: $C_1$ and $C_2$ on one side and $C_3$ and $C_4$ on the other side of the antenna. For the quarter-wave transformer we wanted to have the possibility to use it at 240 MHz and also at 80 MHz for lithium. Therefore, we have selected the length to be $3\lambda/4 \approx 0.6\,\mathrm{m}$ (at 240 MHz with a velocity factor of 0.7). We have chosen to use 4 standard 50 Ω coaxial cables in parallel (QAXIAL RG316/50-FLEX, non-magnetic), which gives an effective $Z_0' = 50\,\Omega/4 = 12.5\,\Omega$. With this choice the load impedance is

$$Z_L = \frac{Z_0'^2}{50\,\Omega} = \frac{50\,\Omega}{16} = 3.125\,\Omega \tag{4.50}$$

and the increase in current is $Z_0/Z_0' = 50/12.5 = 4$. Although the real part of the impedance of the antenna is smaller than the one calculated, the simulation shows that with the sum of all components a good matching is possible (see previous section). All non-tunable capacitors are non-magnetic, high-voltage (1 kV) porcelain multilayer SMD from American Technical Ceramics (ATC 100B series).

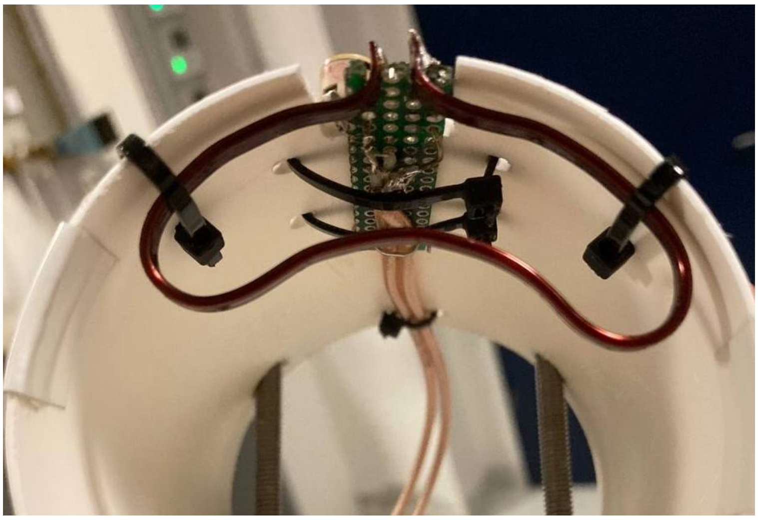

**Figure 4.18.** Photo of the banana-shaped antenna in its mounting system.

## 4.7 Measurement of the coupling efficiency

After I have designed and built the antenna and the matching circuit, I moved to fine tune the parameters – trimmer capacitor and eventually the cable lengths – and to optimize its performance at the desired frequency. When the antenna is tuned correctly, one expects that the reflection is minimum and the transmission is maximum (see Fig. 4.17). In order to measure the reflection I used a directional coupler (Mini-Circuits ZFDC-15-8) as schematically illustrated in Fig. 4.19. This device allows signals to flow from *input* to *output*, with a small fraction (-15 dB) of the input power being sent to the *coupling* output. When the signal flows in the opposite direction, instead, a much smaller fraction (-45 dB) is delivered at the *coupling* output. Therefore, by connecting the RF source on the *output* and the matching circuit with the *input*, I could measure – connecting the spectrum analyzer on the *coupling* output – how much power is reflected back from the matching circuit.

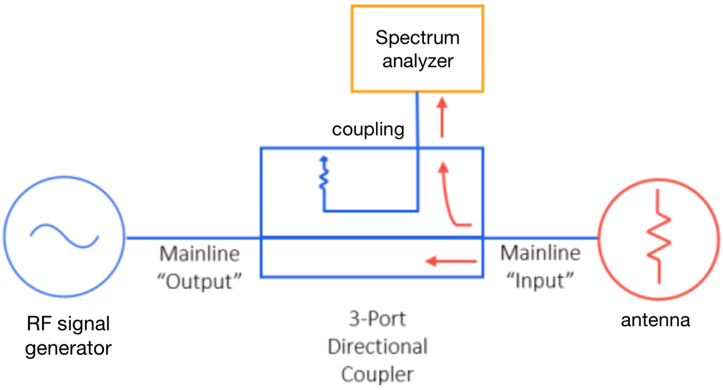

**Figure 4.19.** Schematic of a 3-port directional coupler in a simple reflectometer setup. Figure adapted from [109].

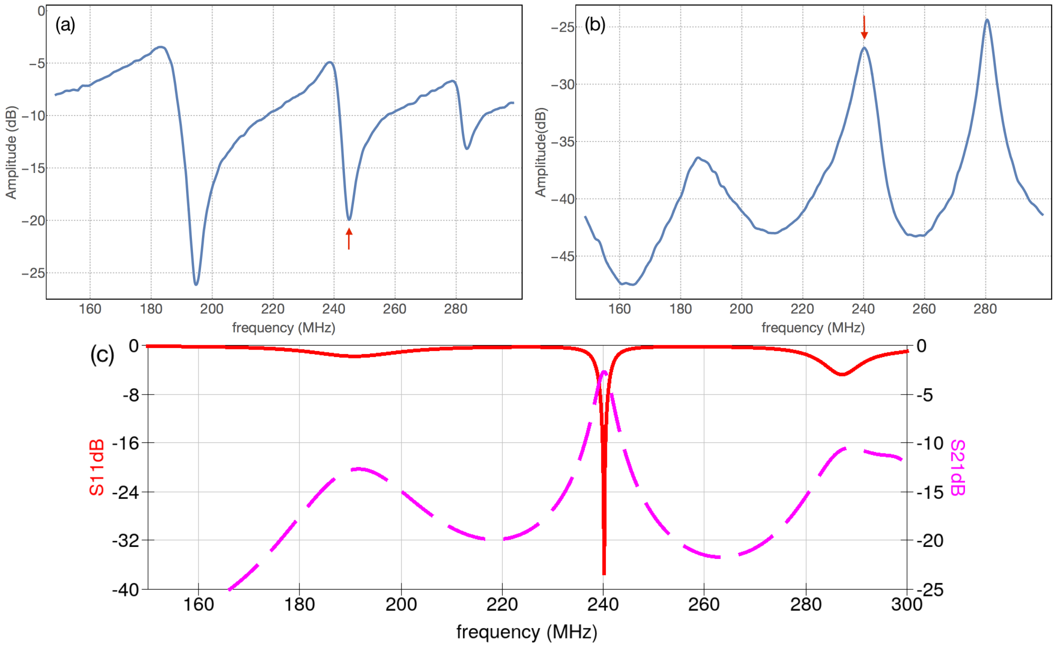

**Figure 4.20.** Reflection **(a)** and emission **(b)** from the antenna, measured by scanning the frequency from 150 MHz to 300 MHz. Red arrows identify the dip (in the reflection) and the peak (in the emission) at 240 MHz. **(c)** Simulation with *QUCS* of the reflected ($S_{11}$, red) and the transmitted signals ($S_{21}$, magenta dashed) as in Fig. 4.17(a), but a wider range of frequencies is plotted.

Fig. 4.20(a) shows the reflected signal from 150 MHz to 300 MHz, performing a frequency sweep with the generator, and monitoring with a spectrum analyzer (using the “max hold” option to display the maximum reflected signal during scanning of the frequency).

We are looking for a dip – identified by a red arrow in Fig. 4.20(a) – in the reflected signal of the antenna, for which most of the power is transmitted to the antenna. Tuning the trimmer capacitor $C_3$ we can move this dip in a range of a few tens of MHz. But we usually find three dips in the reflection where the one at lower frequency (around 195 MHz) is not affected much by $C_3$, while the other two dips (245 MHz and 285 MHz) shift with $C_3$. To understand at which frequency the radiation of the antenna is truly maximized, we are using another antenna, called pick-up antenna, which is a very small single-loop antenna without matching circuit placed close to our matched antenna. This pick-up antenna must have a small size so that its inductance is small enough that its self-resonance frequency is at much higher frequency than our measurement frequency range such that the pick-up antenna is operated in the flat gain region. Panel (b) in Fig. 4.20 shows the signal of the pick-up antenna connected directly to the spectrum analyzer (again taken with the “max hold” function). We find still three peaks corresponding to the three dips but shifted by about 5 MHz towards lower frequencies.

The simulation with QUCS confirms the presence of three features roughly at the observed frequencies, but the center one should be more pronounced, see Fig. 4.20(c). Adding a coupler to the simulation better matches the observation and

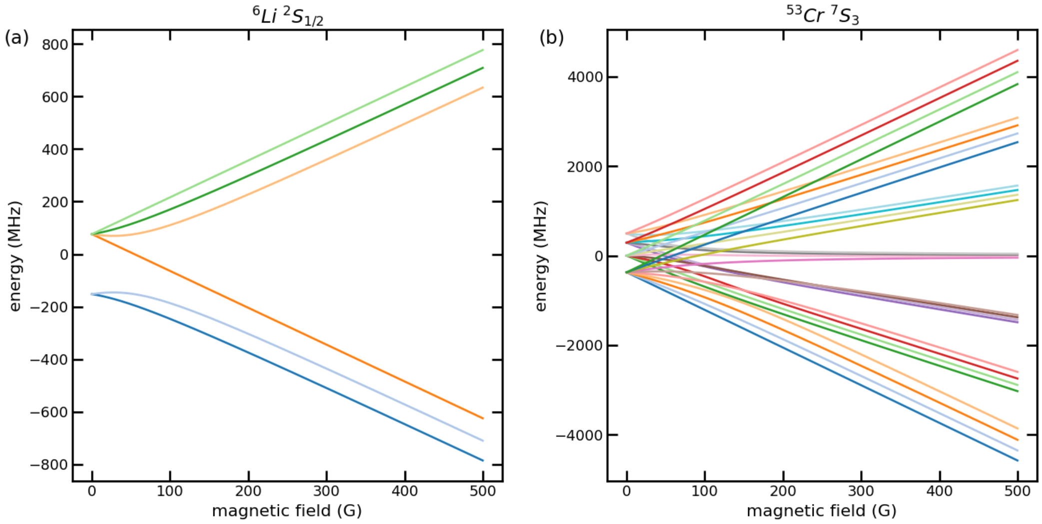

**Figure 4.21.** Energy of the hyperfine levels of ground-state $^6$Li **(a)** and $^{53}$Cr **(b)** atoms as function of the magnetic field. Energy levels calculated and plotted by A. Trenkwalder.

shows also small frequency shifts but the details depend strongly on the configuration. Additionally, the self-resonance of the antenna and that of the pick-up coil can modify significantly the observations.

Therefore, our interpretation is that only the center peak of the pick-up antenna around 240 MHz is the correct peak and we adjust it with the trimmer $C_3$ to the desired chromium transition frequency. This interpretation has been confirmed by the measurement on the atoms which will be presented next.

## 4.8 Test on atoms

We tested the new antenna on the experiment with ultracold chromium atoms. Our goal is to address the transition between the first and the second lowest Zeeman levels of atomic $^{53}$Cr in the ground state, labeled as Cr$|1\rangle$ and Cr$|2\rangle$. Fig. 4.21 depicts the magnetic field dependence of the hyperfine levels of the electronic ground-state of Li on the left, and Cr on the right. The two lowest levels of interest for chromium are colored in blue and light blue, respectively. The Zeeman energy, as a function of magnetic field, for alkali-like atoms – as lithium – with a total electron spin of 1/2, can be calculated with the formula by Breit and Rabi [110]. However, for chromium, which has a total electron spin of 3, a numerical solution is required. This means, the Hamiltonian with the Zeeman and Hyperfine contributions needs to be diagonalized numerically for each relevant magnetic field. The results of this calculation, made by A. Trenkwalder, are plotted in Fig. 4.21. At our magnetic field of interest of 1414 G, the two ground state levels of chromium are separated by an energy of $h \times 240.152$ MHz.

In order to characterize the antenna performance, we conducted a spectroscopic measurement and we observed Rabi oscillations of the atomic population. We prepare a spin polarized sample of chromium atoms in the ground state as follows. After the evaporative cooling, we are left with an ultracold mixture of Li$|1\rangle$, Li$|2\rangle$,

$\mathrm{Cr}|1\rangle$ and $\mathrm{Cr}|2\rangle$. The last one, being only a small fraction, is completely removed by waiting a certain time on the nearby $\mathrm{Li}|1\rangle$-$\mathrm{Cr}|2\rangle$ Feshbach resonance at 1418 G. Instead, the two lithium species are removed by applying resonant light.

In order to improve the accuracy on the atomic populations and minimize the systematics arising from atom number fluctuations, it is desirable to normalize the number of transferred atoms by the total number. This requires counting atoms in both states $\mathrm{Cr}|1\rangle$ and $\mathrm{Cr}|2\rangle$. Since at this field we have only laser light available for imaging of $\mathrm{Cr}|1\rangle$, we employ following strategy to obtain the number of $\mathrm{Cr}|1\rangle$ and $\mathrm{Cr}|2\rangle$. After the spectroscopy RF pulse, we shine the imaging pulse to detect the remaining atoms in the $\mathrm{Cr}|1\rangle$ state. A second (strong) RF $\pi$-pulse on resonance is applied so that all atoms are transferred from the $\mathrm{Cr}|2\rangle$ state back to the $\mathrm{Cr}|1\rangle$ state, where the atoms are imaged with a second optical pulse onto the same camera. This second RF pulse is with 200 μs relative short such that $B$-field fluctuations do not matter and 100% of the atoms are transferred.

Hence, for each experimental cycle, we get informations about the population of the two levels, $N_{Cr|1\rangle}$ and $N_{Cr|2\rangle}$ respectively, with which we can define the relative transferred population of chromium as

$$S = \frac{N_{Cr|2\rangle}}{N_{Cr|1\rangle} + N_{Cr|2\rangle}}. \tag{4.51}$$

We first study the frequency spectrum measured as the transition probability as function of the frequency detuning from resonance. Before starting to acquire the spectroscopy measurement, we find the right parameters – RF power at a given pulse length – in order to have a $\pi$-pulse, which at resonance allows a complete transfer of the atoms from $\mathrm{Cr}|1\rangle$ to $\mathrm{Cr}|2\rangle$. For this measurement, these parameters are fixed at $P = 40\,\mathrm{mW}$ and $\tau = 1.8\,\mathrm{ms}$. By varying the frequency of the RF pulse around the resonance, we get a distribution of data as shown in Fig. 4.22.

The spectroscopy signal follows Eq. (4.24) which I repeat here:

$$S(\delta) = \frac{\Omega^2}{\delta^2 + \Omega^2} \sin^2\left(\frac{\tau}{2}\sqrt{\delta^2 + \Omega^2}\right), \tag{4.52}$$

where $\tau$ is the pulse duration – fixed at 1.8 ms – and $\delta$ the detuning. Note that for a $\pi$-pulse with $\tau = \pi/\Omega$, Eq. (4.52) can be recast into a $sinc^2$ function, which is reminiscent of the Fourier transform of a square pulse but with the detuning scaling as $\sqrt{\delta^2 + \Omega^2}$. $S(\delta)$ well fits the chromium data, from which we get the central frequency of 240.424938(6) MHz, and the Rabi frequency $\Omega = 2\pi \times 267(7)\,\mathrm{Hz}$.

As a second experiment, we study the time evolution of the atomic populations in states $|1\rangle$ and $|2\rangle$ resonantly coupled by the oscillating magnetic field. Starting again from a spin polarized sample in the $\mathrm{Cr}|1\rangle$ state, we measure the transition probability as function of the time duration of a resonant RF pulse for $P = 40\,\mathrm{mW}$. The population of state $|2\rangle$ as function of the pulse duration is shown in Fig. 4.23. The data show clear Rabi flopping and are well fit by the analytic function:

$$S(t) = A \sin^2\left(\frac{\Omega}{2}t + \varphi\right) \tag{4.53}$$

with $A$ the amplitude, $\varphi$ a phase factor and $\Omega$ the Rabi frequency. From the fit I get the following parameters and errors: $A$ = 1.000(5); $\varphi$ = -0.053(7); $\Omega = 2\,\pi \times 264.6(3)\,\mathrm{Hz}$.

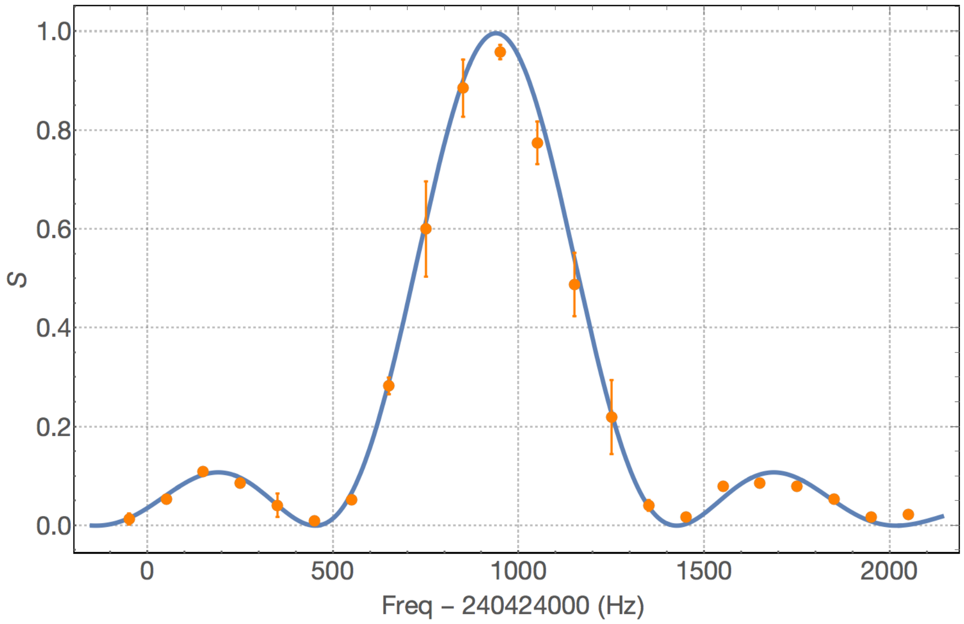

**Figure 4.22.** Chromium spectrum of the transition Cr$|1\rangle \rightarrow$Cr$|2\rangle$, with a pulse power of 40 mW and a pulse length of 1.8 ms. Orange dots are the data with their error bar. Solid blue line represents the fit with Eq. (4.52).

The Rabi frequency obtained from the two measurements are perfectly consistent.

### Comparison of the Rabi frequency

Now, it is useful to compare the Rabi frequency measured, with that expected from the theoretical calculation. We scale the measured Rabi frequency in Fig. 4.23 from 40 mW to 100 W which was used in the simulation in Fig. 4.17.

$$\Omega_{100\,\mathrm{W}} = \Omega_{40\,\mathrm{mW}} \sqrt{\frac{100}{0.04}} = 2\pi \times 13.23\,\mathrm{kHz}. \tag{4.54}$$

Recalling Eq. (4.31), to calculate the Rabi frequency we use $\mu_{\perp}/h = 156.402\,\mathrm{kHz/G}$ calculated by A. Ciamei and the magnetic field amplitude $B_0$. In order to calculate the magnetic field (Sec. 4.4.3) generated at the atoms position we need the current that flows in the coil. From the *QUCS* simulation we get that current (Fig. 4.17) with a RF power of 100 W, i.e. $I_{max} = 5.30\,\mathrm{A}$. This is the current oscillation amplitude but for the effective $B$-field we have to use the root-mean-square value (rms), namely $I_{rms} = 3.75\,\mathrm{A}$. The distance between antenna and atoms we estimate to be 22.5(2.5) mm (see Ref. [78]). Using $B_0 = 83(10)\,\mathrm{mG}$, see Fig. 4.7, we obtain a calculated Rabi frequency of 13(1) kHz which is within 2% of the measured one.

In this chapter I have described how I designed a high-power RF antenna at 240 MHz for efficient RF transfer of chromium atoms between the two lowest hyperfine states around 1414 G. The antenna is optimized to maximize in the near-field regime the transversal magnetic field produced at the position of the atoms, while unwanted magnetic fields in the vertical direction are suppressed. I have presented the basic

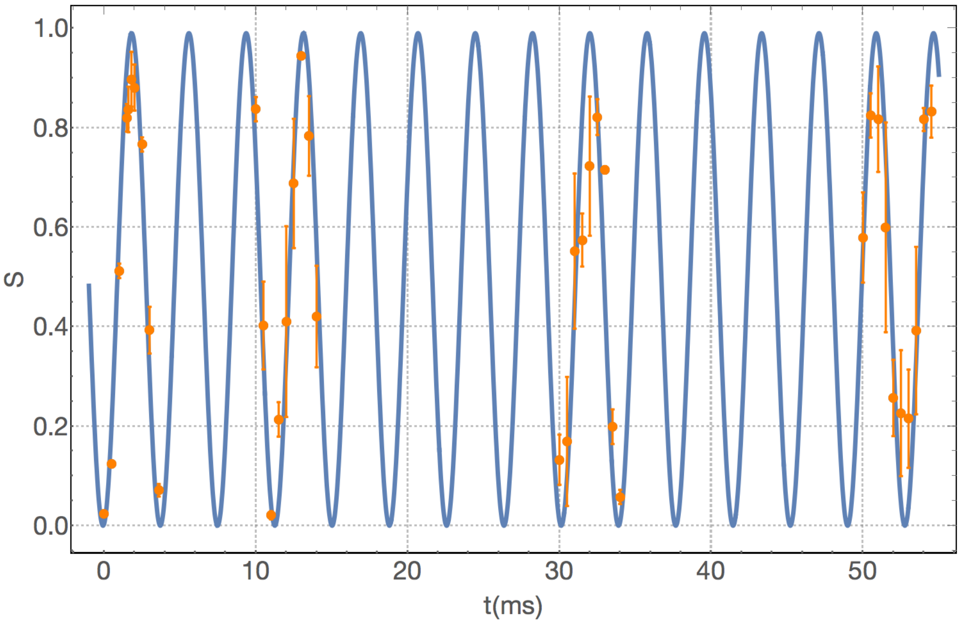

**Figure 4.23.** Rabi oscillation at the resonance between states Cr$|1\rangle$ and Cr$|2\rangle$, for an RF pulse of 40 mW. Orange dots are the data with their error bar. Solid blue line represents the fit result using Eq. (4.53) which gives $\Omega = 2\,\pi \times 264.6(3)\,\mathrm{Hz}$.

theoretical concepts of the antenna and a simple model to analytically calculate the magnetic field produced by the antenna. I have designed and simulated the matching circuit for the realistic antenna. After I have built the antenna and matching circuit I present how the matching was optimized for the design frequency. Finally, I have presented measurements on chromium atoms showing the performance of the antenna and that it perfectly matches with the expectations. In the next Chapter I will present the application of the antenna for the characterization and improvement of the magnetic field stability at 1.4 kG.

# Chapter 5

# Magnetic field stabilization

In order to experimentally explore the rich physics mentioned in the Introduction, fine tuning of interactions close to a Feshbach resonance is needed. As I already discussed in Chapter 3, our Li-Cr mixture exhibits only narrow Feshbach resonances, with a magnetic width of about 0.5 G at rather high magnetic fields, above 1400 G. In order to scan the value of the inter-species scattering length and probe the region of strong interactions, i.e. $k_F\,|a| > 1$, one has to tune the magnetic field by a small fraction of the resonance width. Given our sample conditions, we aim for a resolution better than 5 mG and a corresponding fractional stability of about $5\,\text{mG}/1400\,\text{G} = 4\,\text{ppm}$. ($1\,\text{ppm} = 1$ part per million $= 10^{-6}$) has to be achieved. In this Chapter I will describe how this could be achieved through a combined active field stabilization of the offset magnetic field, and compensation for the residual 50 Hz line noise by giving a feed-forward signal on a dedicated set of AC compensation coils. The detection, characterization, and reduction of magnetic field noise required extensive use of the Cr RF antenna described in the previous Chapter. Finally, I will show how these hardware upgrades significantly improved our accuracy in the experimental determination of the Feshbach molecule magnetic moment as function of the detuning from resonance.

## 5.1 Active current stabilization

The first method we employ in the experiment to stabilize the magnetic field involves an active approach, utilizing a proportional-integral-derivative feedback circuit (PID) to stabilize the current responsible for generating the high offset field of more than 1400 G. The current is monitored by a current transducer (ITN-600S Ultrastab by LEM), which has an offset drift of ±0.8 ppm/month, linearity error of ±1.5 ppm, and temperature coefficient of ±0.5 ppm/K. This transducer provides a secondary current output, that is proportional to the primary current through the $B$-field generating coil. With a current slightly below 200 A (our offset field coils setup being characterized by a field-to-current ratio of about 7.7 G/A), the current-carrying cables were wound three times around the transducer, to fully exploit its maximum primary current of 600 A, see Fig. 5.1. In order to convert the secondary current output into the appropriate input voltage required by the PID, an ultra-high-precision resistor with a nominal value of 5 Ω was utilized. The resistor (Y14675R00000B9L from Vishay) is

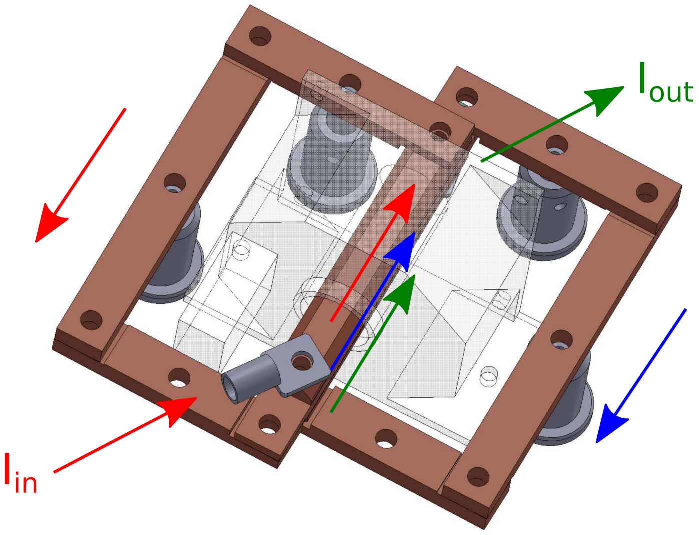

**Figure 5.1.** Design of the copper bars used to feed the same current three times through the current transducer (grey, hole diameter 30 mm). The current of up to 200 A (DC) is entering on the top crimp terminal and passes on the top copper bar (red) through the transducer, is fed on the left side back to the input of the transducer and passes through the middle copper bar (blue), is fed on the right side back to the input of the transducer and passes the third time (green) and exits through the bottom crimp terminal on the bottom side. The three 8 mm thick copper bars passing though the transducer are isolated with 0.5 mm thick plastic from each other and all bars are connected with M8 screws.

designed to handle a maximum power of 10 W, and it has a temperature coefficient of 0.2 ppm/K. This ensures that any change in temperature does not significantly affect the performance and accuracy of the overall system. The output voltage of the PID is transmitted to the analog programming input of the power supply (GSP80-195 from TDK-Lambda), in the range of 0-10 V, to maintain a constant output current through the system. In order to prevent any external radiation to couple into the control electronic circuit, both the PID and the ultra-high-precision resistor are enclosed within a metal box. Furthermore, as anticipated in Sec. 3.4, in order to enable fine-tuning of the magnetic field, and to allow for fast changes in the field, a smaller additional pair of coils (DC comp coils) was utilized. These coils are capable of handling a maximum current of 5 A (0.51 G/A) and their output is independently stabilized via another transducer combined with a PID (*Stanford Research*). Finally, a third pair of coils is used to generate a magnetic field gradient in order to levitate the atoms. This is however not stabilized.

## 5.2 Measurement of the $B$-field noise

Long-term magnetic field fluctuations are determined by the sum of two different contributions. One is random fluctuations of the background magnetic field due to the unpredictable influence of the environment. The other contribution is synchronous with the 50Hz line and can either originate from residual current noise on

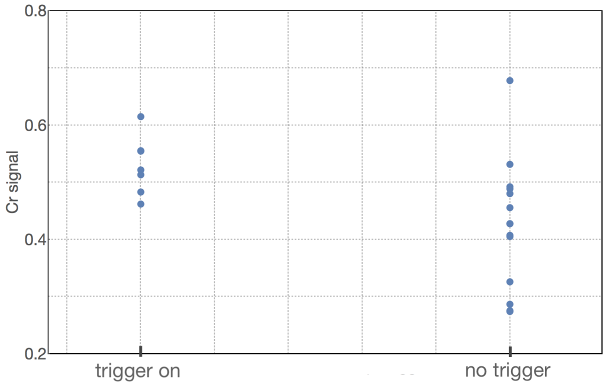

**Figure 5.2.** Transferred chromium atom fraction with (Left) and without (Right) "stop-trigger" at fixed time in the experimental sequence.

the MOT coils or unwanted periodic magnetic fields induced by the surrounding instrumentation. Different dedicated strategies are used to cancel random and 50Hz noise. The former requires a feed-back control based on magnetic field sensors, while the latter can be achieved with a feed-forward.

We characterized the $B$-field noise in the vicinity of one of the Feshbach resonances at 1414-1461 G, probing the radio-frequency transition $\mathrm{Cr}|1\rangle \rightarrow \mathrm{Cr}|2\rangle$ between the lowest two Zeeman levels of atomic Cr. By determining the frequency of maximum transfer, we could calibrate the absolute magnetic field, see Fig. 4.21. At these high fields, the electron and nuclear spin angular momenta decouple, resulting in nearly parallel Zeeman lines, thereby reducing the sensitivity of RF transitions to the magnetic field. The lithium Zeeman shift of the transition is $< 0.8\,\mathrm{kHz/G}$, while that of chromium is $6.041\,\mathrm{kHz/G}$, making chromium 7.5 times more sensitive to the magnetic field fluctuations than lithium. For this reason, we specifically designed the RF antenna to address the $\mathrm{Cr}|1\rangle \rightarrow \mathrm{Cr}|2\rangle$ transition.

We start the measurement with a spin polarized sample of chromium in the $\mathrm{Cr}|1\rangle$ state after the end of the evaporation stage. Lithium atoms are removed with a strong resonant light pulse. We set the RF pulse intensity and length to make a properly detuned $\pi$-pulse, such that 50% of the atoms are transferred into the $\mathrm{Cr}|2\rangle$ state. From any noise seen on the transferred number of atoms, we can infer the magnetic field fluctuation using Eq. (4.52), which is a $sinc^2$ function for a $\pi$-pulse as discussed in Sec. 4.8. On the one hand, the length of the RF pulse should be long to have a high spectral resolution, hence high magnetic field sensitivity. On the other hand, the length is limited by the $B$-field noise level: given a fluctuation amplitude there exists a maximum pulse time for which the binary relation between transfer efficiency and $B$-field detuning is unique. Since this is of order of the *FWHM* of the $sinc^2$ function, we get that $\mathrm{Max}[T] = (\delta\mu\Delta B)^{-1}$. In the experiment we set the longest pulse time for which the transfer efficiency falls into the 20%-80% region, and find it to be 1.8 ms. So, moving the time in which the RF pulse occurs, we acquire the magnetic field behavior versus time.

Despite the presence of noise, we clearly observe 50 Hz fluctuations of the bias field out of statistical noise. Our analysis revealed that the dominant contribution to $B$-field fluctuations is synchronous with the AC line and shows a 50 Hz carrier

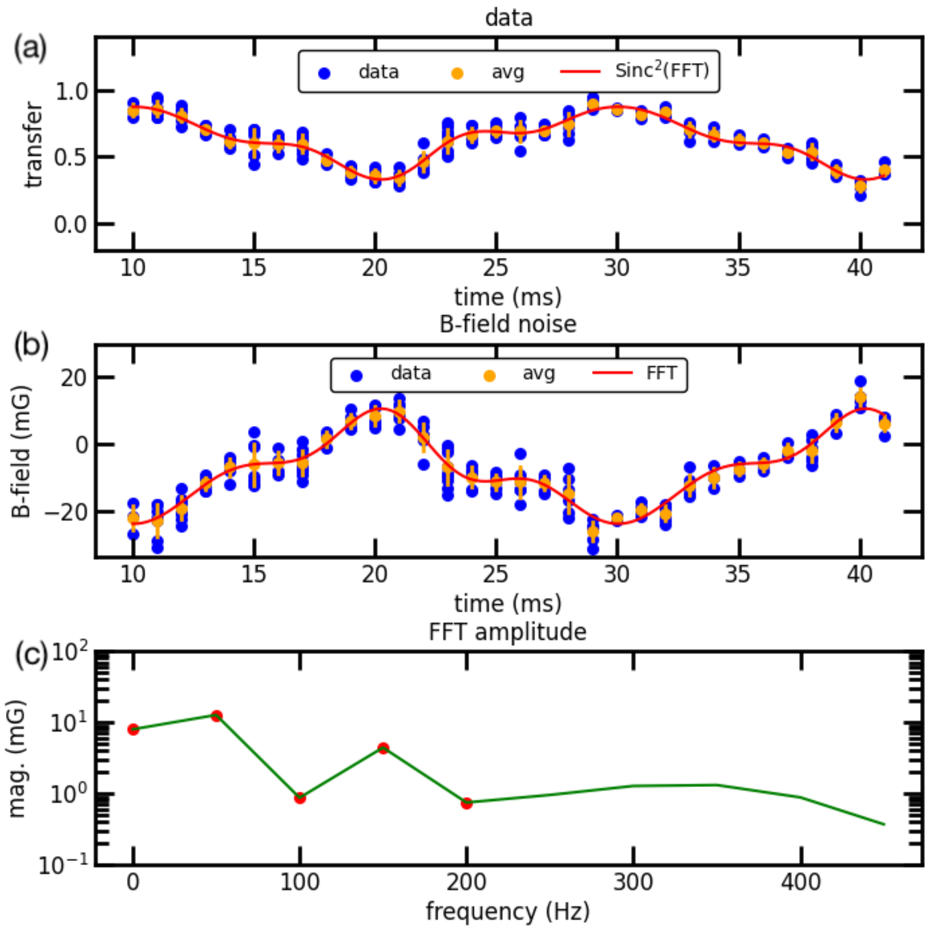

**Figure 5.3.** **(a)** Measurement of the magnetic field fluctuation seen through variation in the the transferred atom fraction. A $\pi$-pulse is applied with detuning to have 50% transfer. The time of the RF pulse is varied with respect to the second line trigger; **(b)** data of plot in (a) with the transferred fraction converted in mG; **(c)** FFT of the signal noise, with red dots highlighting the main frequency components.

frequency with additional higher harmonics at 100 Hz and 150 Hz. To measure better this noise, we have two options: (a) measure the phase of the power line at the start of each RF pulse, or (b) synchronize the experiment to ensure the same phase for each repetition. We choose the second option, as it enables us to later compensate for the AC power line noise (see next Section).

In our laboratory, we utilize a 10 Hz signal which provides a TTL pulse in synchronization with the AC power line. This “line-trigger” signal marks the beginning of each experiment. The control system waits for the line-trigger to start the experimental sequence, which guarantees a fixed phase of the power line at the beginning of the experiment. However, as the line frequency deviates from 50 Hz by up to ±0.2 Hz over extended periods of time [111], the typical jitter after one second can be up to ±4 ms. After 10 seconds of experiment time, this jitter can increase up to ±40 ms, making it unacceptable for measuring a 50 Hz signal with a period of 20 ms.

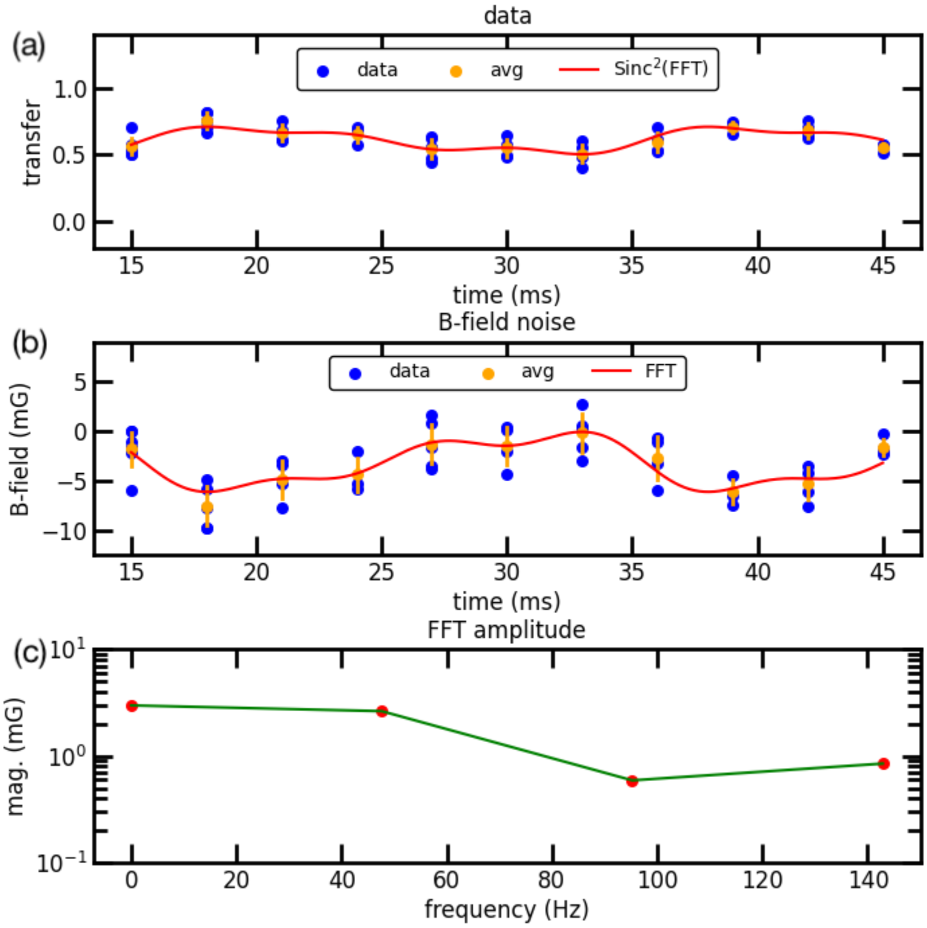

**Figure 5.4.** The same measurement of Fig. 5.3 with the first AC line compensation implemented. **(a)** Measurement of the residual magnetic field fluctuations after the first compensation; **(b)** data of plot in (a) with the transferred fraction converted in mG; **(c)** FFT of the signal noise, with red dots highlighting the main frequency components.

In order to reduce the jitter caused by the AC line frequency, we program the control system to stop the experiment at a given time via a “stop-trigger”, and only continue the experimental sequence at the arrival of the next line trigger. This allows us to minimize the jitter to order of ±0.1 ms, making the phase jitter negligible.

A comparison of the jitter with and without the second line trigger is presented in Fig. 5.2, which shows the fluctuation of the transferred chromium fraction from shot-to-shot, once the RF frequency detuning is set to – ideally – yield a 50% transfer. This method ensures accurate and reliable measurement of the line induced noise, which is crucial for our experimental setup.

By using an optimal 1.8 ms-long RF pulse, Fig. 5.3(a) shows the transferred number of chromium atoms as a function of the time between the line trigger and the start of the RF pulse. Fig. 5.3(b) shows the calculated magnetic field fluctuations $\delta B$ obtained from $S(\delta)$ by numerical inversion of Eq. (4.52) using a perfect $\pi$-pulse with $\tau = \pi/\Omega$. In order to convert the frequency detuning $\delta$ into a magnetic field

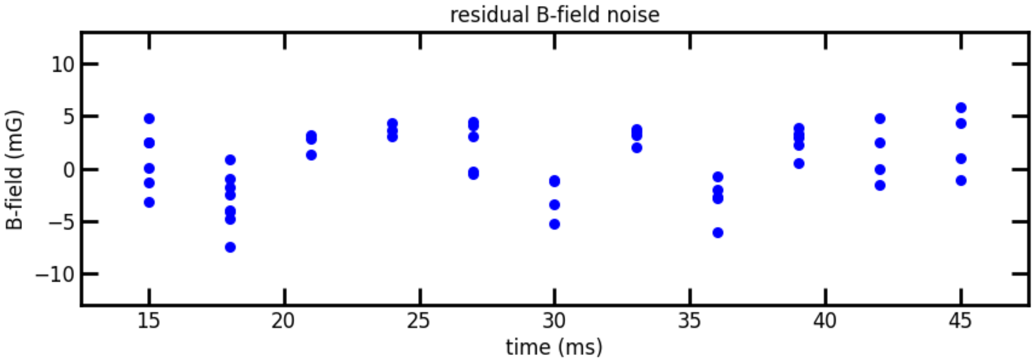

**Figure 5.5.** Residual magnetic field noise after two compensations implemented.

detuning $\delta B$, we use the relation

$$\delta = 2\pi \cdot 6.041 \left(\frac{\text{kHz}}{\text{G}}\right) \cdot \delta B(\text{G}) = 2\pi \cdot 6.041 \left(\frac{\text{Hz}}{\text{mG}}\right) \cdot \delta B(\text{mG}). \tag{5.1}$$

We find that the magnetic field fluctuations are of order of 30-40 mG peak-to-peak, and the Fourier transform of the noise presented in Fig. 5.3(c) shows clear peaks at 50 Hz, 100 Hz and 150 Hz, respectively. The source of the noise was not investigated thoroughly, but we suspect that the main component is due to the current producing the offset field, possibly created by ground loops between the control computer, the PID and the power supply.

## 5.3 AC line noise compensation

In order to mitigate the AC line noise, we employ the measured $B$-field fluctuations in Sec. 5.2 and feed a typical 60 mA AC current into a third coil, wound around the resin support of the top MOT coil, and featuring a field-to-current ratio of about 0.5 G/A. Each current value – extrapolated from the FFT parameters – is sent every 10 µs. This method allowed us to nearly cancel out the AC line noise.

After that, we took a further measurement of the residual noise as in Sec. 5.2, but now with the compensation applied, and with a longer RF pulse of 3.6 ms, which correspondingly increased our sensitivity by a factor 2. This measurement allows us to evaluate the effectiveness of the compensation, and to verify that the residual noise was indeed significantly reduced. By comparing the results of this measurement, shown in Fig. 5.4, with the ones obtained without compensation, a significant reduction in noise was observable, even if not completely eliminated. In particular, a non-zero contribution at the line frequency component was still evident. We thus added the measured remaining noise to the previously measured one and feed the combined signal into the AC compensation coil. With this applied we verify in a third measurement the residual noise, again with the 3.6 ms-long pulse, see Fig. 5.5. We see that all datapoints remain within about 13 mG peak-to-peak and no significant AC line contribution is visible, meaning that only random noise remains. The standard deviation of this data is 3.2 mG and fitting a Gaussian into the histogram of the data gives a sigma of 3.6(6) mG. Note that this result includes

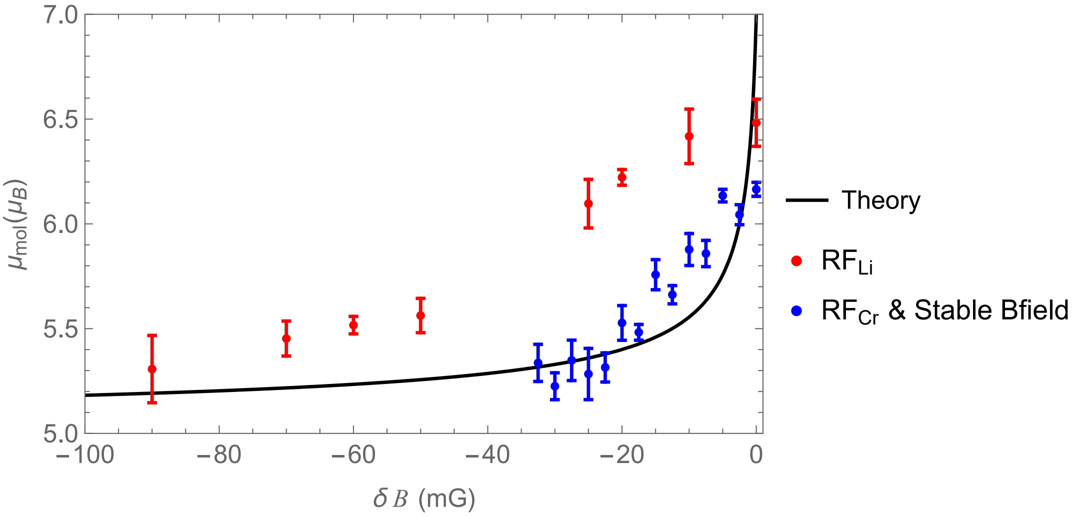

**Figure 5.6.** Magnetic moment of LiCr Feshbach dimers as function of magnetic field detuning ($\delta B$) from the resonance pole. Red circles show the measurement results before $B$-field stabilization and with RF cleaning on Li, while blue circles show the results after $B$-field stabilization and with the RF cleaning on Cr. The solid line is the theoretical expectation, neglecting $B$-field noise and inhomogeneities, obtained from Eq. (1.26), using the open-channel fraction in Eq. (1.25) to interpolate between the atomic ($7\,\mu_B$) and molecule ($5\,\mu_B$) magnetic moments.

also noise coming from imaging and fitting of the atom number. Therefore this is an upper boundary.

This is an impressive result, given the relatively simple scheme followed to implement the stabilization, and considering that no extreme care was taken, so far, to physically remove from the experimental table several possible sources of $B$-field noise (such as low-power power supplies, etc.).

At 1414 G offset field the remaining noise corresponds to 2.5(4) ppm relative magnetic field stability which is even better than what was our defined goal at the beginning of this chapter. Moreover, it will allow us to finely control the Li-Cr interactions near the 1414 G and 1461 G Feshbach resonances.

Finally, I show how the $B$-field stabilization, and the use of the Cr RF antenna instead of the Li antenna, have impacted on the experimental investigation of the magnetic moment of LiCr Feshbach dimers. The measured magnetic moment as function of detuning from the Feshbach resonance pole is shown in Fig. 5.6 both after these hardware upgrades (blue circles) and before (red circles) as reported earlier in Fig. 3.8.

With this improvement, there is now a significant enhancement in the quality of the measurement: the experimental data now shows a much better agreement with the theoretical curve, allowing for a more accurate and precise determination of the physical parameters of interest. Additionally, the field stability achieved allows us to reduce the step size with which the field can be adjusted, resulting in more detailed and refined data. Overall, the magnetic field stabilization has significantly increased the reliability and accuracy of the measurements.

# Conclusions

In conclusion, during my master thesis I contributed to provide a substantial upgrade in the Lab. 9 experimental setup, allowing to significantly boost the investigation of resonantly-interacting Fermi mixtures of ultracold lithium and chromium atoms.

On the one hand, I actively participated to the optimization of the experimental routine, that allowed us to produce, on a 12 s-long duty cycle, highly-degenerate $^6$Li-$^{53}$Cr Fermi mixtures of more than $2 \times 10^5$ and $10^5$ atoms per species, at reduced temperatures of $T/T_F \sim 0.25$, for both components simultaneously.

On the other hand, the design, realization and successful test of a new RF setup for the controlled manipulation of the spin-state of chromium atoms, enabled us to efficiently transfer the atomic mixture in and out of the resonantly-interacting regime, as well as to precisely characterize the magnetic field stability in the experiment. In turn, this latter characterization was crucial to devise a simple but efficient scheme to actively stabilize the magnetic-field bias. This allowed me to achieve a rather impressive compensation of the $B$-field noise, reducing it, over several tens of ms, down to a few mG at bias values of more than 1400 G, i.e. down to a few ppm.

The successful implementation of these important technical upgrades on the main experimental machine, and their integration within the experimental cycle, has already opened the possibility to controllably produce, and to precisely characterize, ultracold lithium-chromium mixtures under resonantly-interacting conditions.

Besides the characterization of LiCr dimer formation near the high-field Feshbach resonance above 1.4 kG, currently still ongoing, my thesis paves the way to a wealth of exciting studies in the near future. In fact, the possibility to controllably access the strongly-interacting region with an accuracy of a few mG over about 100 ms, will allow us to perform investigation of the rich few- and many-body phenomena mentioned in the Introduction of my thesis. For instance, if the collisional stability of Feshbach dimers – at present ongoing research in the lab – will enable to achieve molecule lifetimes of a few tens of ms, realization of molecular Bose-Einstein condensates of weakly-bound LiCr dimers could be within experimental reach in the forthcoming months. This would not only represent the first step towards the experimental study of the BCS-BEC crossover within a mass-imbalanced fermionic system, but it would also represent a pristine starting point towards the realization – through coherent optical transfer – of degenerate Bose gases of LiCr ground-state, paramagnetic polar molecules.

Finally, the design of the RF setup, that I implemented here to efficiently control the internal state of chromium atoms, could be rather straightforwardly adapted also to the spin manipulation of the lithium component. In turn, the experimental ability to reliably drive RF transitions on both fermionic species, would represent an excellent possibility to perform investigation of both heavy and light impurity problems within the same experimental setup and physical system, as well as to disclose, through state-of-the-art RF spectroscopy schemes, elusive few-body cluster states, or non-trivial resonant processes in the atom-dimer scattering.

# Acknowledgments

*Ed eccoci qui, giunti per davvero a tirar le somme di questo impegnativo e meraviglioso percorso universitario. Ricordo bene quando ho maturato la decisione di studiare fisica per davvero, e ripensandoci ora non posso fare altro che ringraziare il me di allora che, con coraggio, passione e determinazione, scelse di intraprendere questo viaggio. Sono davvero felice di aver realizzato qui, nella vita reale, quello che all'epoca era solo un magico sogno di un ragazzo che leggeva libri di fisica in autobus mentre andava al liceo. Ammetto che questo percorso non è stato affatto semplice, e se sono arrivato fin qui è solo grazie alle persone qui di seguito raccontate.*

*Un primo grazie lo devo al professore Giovanni Modugno che mi ha indirizzato verso un'ambito della fisica sperimentale talmente affascinante da avermi coinvolto appieno. La sua passione, la sua competenza e la sua dedizione nell'insegnamento mi hanno ispirato profondamente e hanno contribuito in modo significativo alla mia crescita accademica e personale. Grazie per avermi indirizzato verso il Lab 9, lì dentro ho trovato fisica a livelli altissimi e soprattutto persone meravigliose.*

*Un grazie è per Matteo, che sin dall'inizio ha dimostrato un sostegno costante e un impegno instancabile nel seguirmi lungo tutto il percorso. La sua presenza attenta e i suoi preziosi consigli sono stati fondamentali per affrontare le sfide che ho incontrato lungo il cammino. La sua disponibilità nel discutere idee, rispondere alle mie domande e fornire feedback tempestivi è stata di inestimabile valore. Sono grato per la sua fiducia in me e per l'entusiasmo che ha dimostrato nei confronti del mio lavoro e delle mie capacità.*

*Un grazie ad Andreas, che con la sua conoscenza smisurata e col suo costante supporto, mi ha insegnato davvero tanto riguardo gli aspetti tecnici di laboratorio che amo profondamente. Con la sua pazienza mi ha supportato e sostenuto sin dall'inizio del mio percorso, trasmettendomi la sua grande passione per la scienza.*

*Un grazie ad Alessio per avermi fatto vedere con occhi diversi e comprendere meglio aspetti fondamentali della fisica atomica, sia a livello teorico che sperimentale, e per le piacevoli chiacchierate mentre allineavamo il setup ottico che spaziavano dalla fisica alla storia romana, con tanto di aneddoti e curiosità.*

*Un grazie a Stefano che mi ha guidato da molto vicino lungo quest'avventura, insegnandomi a capire, controllare, e manovrare il complesso setup sperimentale del Lab 9. La sua precisione nel trasmettere le informazioni e la sua dedizione nel rendere concetti complessi accessibili sono stati di inestimabile valore.*

*Un grazie anche ai nuovi arrivati Beatrice e Max per le piacevoli conversazioni e i consigli utili tra i lunch time sul prato e le pause caffè. Grazie Lab 9 per essere stato un punto di riferimento affidabile di amici preziosi durante questo percorso accademico.*

*Un enorme grazie è per la mia famiglia, che ha sostenuto e incoraggiato in ogni modo il mio percorso universitario con pazienza e comprensione. Il vostro sostegno incondizionato è stato fondamentale per superare gli ostacoli e inseguire i miei sogni. Grazie per avermi spronato a dare il massimo e per aver sempre creduto in me.*

*Un gigantesco grazie è per Ilaria, che è stata un pilastro di supporto e un'ancora di stabilità in tutti questi anni. Grazie per il tuo incoraggiamento e la tua comprensione mentre dedicavo lunghissime giornate allo studio. Il tuo amore e il tuo sostegno mi*

*hanno dato la forza necessaria per affrontare le sfide e mi hanno reso consapevole della fortuna di avere qualcuno come te al mio fianco.*
*Un immenso grazie è per tutti gli amici, quelli da sempre al mio fianco, quelli trovati lungo il percorso, quelli con cui ho condiviso mille emozioni, quelli che credono in me e mi aiutano a crescere, quelli che mi fanno sorridere, quelli che mi fanno fare l'alba e quelli sempre pronti per una nuova avventura.*

# Bibliography

[1] R. Casalbuoni and G. Nardulli, “Inhomogeneous superconductivity in condensed matter and qcd,” *Rev. Mod. Phys.*, vol. 76, pp. 263–320, Feb 2004.

[2] O. Andersen and L. Boeri, “On the multi-orbital band structure and itinerant magnetism of iron-based superconductors,” *Annalen der Physik*, vol. 523, no. 1-2, pp. 8–50, 2011.

[3] H.-W. Hammer, A. Nogga, and A. Schwenk, “Colloquium: Three-body forces: From cold atoms to nuclei,” *Rev. Mod. Phys.*, vol. 85, pp. 197–217, Jan 2013.

[4] M. Yi, Y. Zhang, Z.-X. Shen, and D. Lu, “Role of the orbital degree of freedom in iron-based superconductors,” *npj Quantum Materials*, vol. 2, p. 57, Oct 2017.

[5] G. Wang, A. Chernikov, M. M. Glazov, T. F. Heinz, X. Marie, T. Amand, and B. Urbaszek, “Colloquium: Excitons in atomically thin transition metal dichalcogenides,” *Rev. Mod. Phys.*, vol. 90, p. 021001, Apr 2018.

[6] Y. Jiang, S. Chen, W. Zheng, B. Zheng, and A. Pan, “Interlayer exciton formation, relaxation, and transport in tmd van der waals heterostructures,” *Light: Science & Applications*, vol. 10, p. 72, Apr 2021.

[7] C. Chin, R. Grimm, P. Julienne, and E. Tiesinga, “Feshbach resonances in ultracold gases,” *Rev. Mod. Phys.*, vol. 82, pp. 1225–1286, Apr 2010.

[8] V. Efimov, “Energy levels of three resonantly interacting particles,” *Nuclear Physics A*, vol. 210, no. 1, pp. 157–188, 1973.

[9] O. I. Kartavtsev and A. V. Malykh, “Low-energy three-body dynamics in binary quantum gases,” *Journal of Physics B: Atomic, Molecular and Optical Physics*, vol. 40, pp. 1429–1441, mar 2007.

[10] Y. Nishida and S. Tan, “Universal fermi gases in mixed dimensions,” *Phys. Rev. Lett.*, vol. 101, p. 170401, Oct 2008.

[11] J. Levinsen, T. G. Tiecke, J. T. M. Walraven, and D. S. Petrov, “Atom-dimer scattering and long-lived trimers in fermionic mixtures,” *Phys. Rev. Lett.*, vol. 103, p. 153202, Oct 2009.

[12] Y. Castin, C. Mora, and L. Pricoupenko, “Four-body efimov effect for three fermions and a lighter particle,” *Phys. Rev. Lett.*, vol. 105, p. 223201, Nov 2010.

[13] S. Endo, P. Naidon, and M. Ueda, “Universal physics of 2+1 particles with non-zero angular momentum,” *Few-Body Systems*, vol. 51, pp. 207–217, Nov 2011.

[14] D. Blume, “Few-body physics with ultracold atomic and molecular systems in traps,” *Reports on Progress in Physics*, vol. 75, p. 046401, mar 2012.

[15] S. Endo, P. Naidon, and M. Ueda, “Crossover trimers connecting continuous and discrete scaling regimes,” *Phys. Rev. A*, vol. 86, p. 062703, Dec 2012.

[16] V. Ngampruetikorn, M. M. Parish, and J. Levinsen, “Three-body problem in a two-dimensional fermi gas,” *EPL (Europhysics Letters)*, vol. 102, p. 13001, apr 2013.

[17] J. Levinsen and M. M. Parish, “Bound states in a quasi-two-dimensional fermi gas,” *Phys. Rev. Lett.*, vol. 110, p. 055304, Jan 2013.

[18] B. Bazak and D. S. Petrov, “Five-body efimov effect and universal pentamer in fermionic mixtures,” *Phys. Rev. Lett.*, vol. 118, p. 083002, Feb 2017.

[19] B. Bazak, “Mass-imbalanced fermionic mixture in a harmonic trap,” *Phys. Rev. A*, vol. 96, p. 022708, Aug 2017.

[20] R. Liu, C. Peng, and X. Cui, “Universal tetramer and pentamer in two-dimensional fermionic mixtures,” 2022.

[21] W. V. Liu and F. Wilczek, “Interior gap superfluidity,” *Phys. Rev. Lett.*, vol. 90, p. 047002, Jan 2003.

[22] M. M. Forbes, E. Gubankova, W. V. Liu, and F. Wilczek, “Stability criteria for breached-pair superfluidity,” *Phys. Rev. Lett.*, vol. 94, p. 017001, Jan 2005.

[23] M. Iskin and C. A. R. Sá de Melo, “Two-species fermion mixtures with population imbalance,” *Phys. Rev. Lett.*, vol. 97, p. 100404, Sep 2006.

[24] M. M. Parish, F. M. Marchetti, A. Lamacraft, and B. D. Simons, “Finite-temperature phase diagram of a polarized fermi condensate,” *Nature Phys.*, vol. 3, pp. 124–128, 02 2007.

[25] M. A. Baranov, C. Lobo, and G. V. Shlyapnikov, “Superfluid pairing between fermions with unequal masses,” *Phys. Rev. A*, vol. 78, p. 033620, Sep 2008.

[26] K. B. Gubbels, J. E. Baarsma, and H. T. C. Stoof, “Lifshitz point in the phase diagram of resonantly interacting $^6$Li$-^{40}\mathbf{K}$ mixtures,” *Phys. Rev. Lett.*, vol. 103, p. 195301, Nov 2009.

[27] A. Gezerlis, S. Gandolfi, K. E. Schmidt, and J. Carlson, “Heavy-light fermion mixtures at unitarity,” *Phys. Rev. Lett.*, vol. 103, p. 060403, Aug 2009.

[28] J. E. Baarsma, K. B. Gubbels, and H. T. C. Stoof, “Population and mass imbalance in atomic fermi gases,” *Phys. Rev. A*, vol. 82, p. 013624, Jul 2010.

[29] K. Gubbels and H. Stoof, "Imbalanced fermi gases at unitarity," *Physics Reports*, vol. 525, no. 4, pp. 255–313, 2013.

[30] J. Wang, Y. Che, L. Zhang, and Q. Chen, "Enhancement effect of mass imbalance on fulde-ferrell-larkin-ovchinnikov type of pairing in fermi-fermi mixtures of ultracold quantum gases," *Scientific Reports*, vol. 7, p. 39783, Jan 2017.

[31] M. Pini, P. Pieri, R. Grimm, and G. C. Strinati, "Beyond-mean-field description of a trapped unitary fermi gas with mass and population imbalance," *Phys. Rev. A*, vol. 103, p. 023314, Feb 2021.

[32] C. W. von Keyserlingk and G. J. Conduit, "Itinerant ferromagnetism in an interacting fermi gas with mass imbalance," *Phys. Rev. A*, vol. 83, p. 053625, May 2011.

[33] A. Sotnikov, D. Cocks, and W. Hofstetter, "Advantages of mass-imbalanced ultracold fermionic mixtures for approaching quantum magnetism in optical lattices," *Phys. Rev. Lett.*, vol. 109, p. 065301, Aug 2012.

[34] A. Sotnikov, M. Snoek, and W. Hofstetter, "Magnetic phases of mass- and population-imbalanced ultracold fermionic mixtures in optical lattices," *Phys. Rev. A*, vol. 87, p. 053602, May 2013.

[35] P. Massignan, Z. Yu, and G. M. Bruun, "Itinerant ferromagnetism in a polarized two-component fermi gas," *Phys. Rev. Lett.*, vol. 110, p. 230401, Jun 2013.

[36] X. Cui and T.-L. Ho, "Phase separation in mixtures of repulsive fermi gases driven by mass difference," *Phys. Rev. Lett.*, vol. 110, p. 165302, Apr 2013.

[37] D. Blume, "Universal four-body states in heavy-light mixtures with a positive scattering length," *Phys. Rev. Lett.*, vol. 109, p. 230404, Dec 2012.

[38] J. Levinsen and D. S. Petrov, "Atom-dimer and dimer-dimer scattering in fermionic mixtures near a narrow feshbach resonance," *The European Physical Journal D*, vol. 65, pp. 67–82, Nov 2011.

[39] P. Naidon and S. Endo, "Efimov physics: a review," *Reports on Progress in Physics*, vol. 80, p. 056001, mar 2017.

[40] E. Wille, F. M. Spiegelhalder, G. Kerner, D. Naik, A. Trenkwalder, G. Hendl, F. Schreck, R. Grimm, T. G. Tiecke, J. T. M. Walraven, S. J. J. M. F. Kokkelmans, E. Tiesinga, and P. S. Julienne, "Exploring an ultracold fermi-fermi mixture: Interspecies feshbach resonances and scattering properties of $^6$Li and $^{40}$K," *Phys. Rev. Lett.*, vol. 100, p. 053201, Feb 2008.

[41] A.-C. Voigt, M. Taglieber, L. Costa, T. Aoki, W. Wieser, T. W. Hänsch, and K. Dieckmann, "Ultracold heteronuclear fermi-fermi molecules," *Phys. Rev. Lett.*, vol. 102, p. 020405, Jan 2009.

[42] L. Costa, J. Brachmann, A.-C. Voigt, C. Hahn, M. Taglieber, T. W. Hänsch, and K. Dieckmann, "$s$-wave interaction in a two-species fermi-fermi mixture at a narrow feshbach resonance," *Phys. Rev. Lett.*, vol. 105, p. 123201, Sep 2010.

[43] C. Ravensbergen, V. Corre, E. Soave, M. Kreyer, E. Kirilov, and R. Grimm, "Production of a degenerate fermi-fermi mixture of dysprosium and potassium atoms," *Phys. Rev. A*, vol. 98, p. 063624, Dec 2018.

[44] C. Ravensbergen, E. Soave, V. Corre, M. Kreyer, B. Huang, E. Kirilov, and R. Grimm, "Resonantly interacting fermi-fermi mixture of $^{161}$Dy and $^{40}$K," *Phys. Rev. Lett.*, vol. 124, p. 203402, May 2020.

[45] H. Hara, Y. Takasu, Y. Yamaoka, J. M. Doyle, and Y. Takahashi, "Quantum degenerate mixtures of alkali and alkaline-earth-like atoms," *Phys. Rev. Lett.*, vol. 106, p. 205304, May 2011.

[46] A. Green, H. Li, J. H. See Toh, X. Tang, K. C. McCormick, M. Li, E. Tiesinga, S. Kotochigova, and S. Gupta, "Feshbach resonances in $p$-wave three-body recombination within fermi-fermi mixtures of open-shell $^6$Li and closed-shell $^{173}$Yb atoms," *Phys. Rev. X*, vol. 10, p. 031037, Aug 2020.

[47] M. Jag, M. Zaccanti, M. Cetina, R. S. Lous, F. Schreck, R. Grimm, D. S. Petrov, and J. Levinsen, "Observation of a strong atom-dimer attraction in a mass-imbalanced fermi-fermi mixture," *Phys. Rev. Lett.*, vol. 112, p. 075302, Feb 2014.

[48] A. Ciamei, S. Finelli, A. Trenkwalder, M. Inguscio, A. Simoni, and M. Zaccanti, "Exploring ultracold collisions in $^6$Li$-^{53}$Cr fermi mixtures: Feshbach resonances and scattering properties of a novel alkali-transition metal system," *Phys. Rev. Lett.*, vol. 129, p. 093402, Aug 2022.

[49] D. S. Petrov, "Three-body problem in fermi gases with short-range interparticle interaction," *Phys. Rev. A*, vol. 67, p. 010703, Jan 2003.

[50] E. Stoner, "Atomic moments in ferromagnetic metals and alloys with non-ferromagnetic elements," *Philos. Mag.*, vol. 15, pp. 1018–1034, 1933.

[51] G.-B. Jo, Y.-R. Lee, J.-H. Choi, C. A. Christensen, T. H. Kim, J. H. Thywissen, D. E. Pritchard, and W. Ketterle, "Itinerant ferromagnetism in a fermi gas of ultracold atoms," *Science*, vol. 325, no. 5947, pp. 1521–1524, 2009.

[52] F. Scazza, G. Valtolina, P. Massignan, A. Recati, A. Amico, A. Burchianti, C. Fort, M. Inguscio, M. Zaccanti, and G. Roati, "Repulsive fermi polarons in a resonant mixture of ultracold $^6$li atoms," *Phys. Rev. Lett.*, vol. 118, p. 083602, Feb 2017.

[53] G. Valtolina, F. Scazza, A. Amico, A. Burchianti, A. Recati, T. Enss, M. Inguscio, M. Zaccanti, and G. Roati, "Exploring the ferromagnetic behaviour of a repulsive fermi gas through spin dynamics," *Nat. Phys.*, vol. 13, pp. 704–709, Jul 2017.

[54] A. Amico, F. Scazza, G. Valtolina, P. E. S. Tavares, W. Ketterle, M. Inguscio, G. Roati, and M. Zaccanti, “Time-resolved observation of competing attractive and repulsive short-range correlations in strongly interacting fermi gases,” *Phys. Rev. Lett.*, vol. 121, p. 253602, Dec 2018.

[55] F. Scazza, G. Valtolina, A. Amico, P. E. S. Tavares, M. Inguscio, W. Ketterle, G. Roati, and M. Zaccanti, “Exploring emergent heterogeneous phases in strongly repulsive fermi gases,” *Phys. Rev. A*, vol. 101, p. 013603, Jan 2020.

[56] K. Zaremba-Kopczyk, M. Gronowski, and M. Tomza. "Ultracold mixtures of Cr and Li atoms: theoretical prospects for controlled atomic collisions, LiCr molecule formation, and molecular precision measurements" (Manuscript in preparation).

[57] F. M. Spiegelhalder, A. Trenkwalder, D. Naik, G. Kerner, E. Wille, G. Hendl, F. Schreck, and R. Grimm, “All-optical production of a degenerate mixture of $^{6}$Li and $^{40}$K and creation of heteronuclear molecules,” *Phys. Rev. A*, vol. 81, p. 043637, Apr 2010.

[58] R. Chicireanu, A. Pouderous, R. Barbé, B. Laburthe-Tolra, E. Maréchal, L. Vernac, J.-C. Keller, and O. Gorceix, “Simultaneous magneto-optical trapping of bosonic and fermionic chromium atoms,” *Phys. Rev. A*, vol. 73, p. 053406, May 2006.

[59] B. Naylor, A. Reigue, E. Maréchal, O. Gorceix, B. Laburthe-Tolra, and L. Vernac, “Chromium dipolar fermi sea,” *Phys. Rev. A*, vol. 91, p. 011603, Jan 2015.

[60] E. Neri, A. Ciamei, C. Simonelli, I. Goti, M. Inguscio, A. Trenkwalder, and M. Zaccanti, “Realization of a cold mixture of fermionic chromium and lithium atoms,” *Phys. Rev. A*, vol. 101, p. 063602, Jun 2020.

[61] Chicireanu, R., Beaufils, Q., Pouderous, A., Laburthe-Tolra, B., Maréchal, É., Vernac, L., Keller, J.-C., and Gorceix, O., “Accumulation of chromium metastable atoms into an optical trap,” *Eur. Phys. J. D*, vol. 45, no. 2, pp. 189–195, 2007.

[62] Q. Beaufils, R. Chicireanu, T. Zanon, B. Laburthe-Tolra, E. Maréchal, L. Vernac, J.-C. Keller, and O. Gorceix, “All-optical production of chromium bose-einstein condensates,” *Phys. Rev. A*, vol. 77, p. 061601, Jun 2008.

[63] D. Naik, A. Trenkwalder, C. Kohstall, F. M. Spiegelhalder, M. Zaccanti, G. Hendl, F. Schreck, R. Grimm, T. M. Hanna, and P. S. Julienne, “Feshbach resonances in the $^{6}$Li and $^{40}$K Fermi-Fermi mixture: elastic versus inelastic interactions,” *The European Physical Journal D*, vol. 65, pp. 55–65, Nov 2011.

[64] A. Ciamei, S. Finelli, A. Cosco, M. Inguscio, A. Trenkwalder, and M. Zaccanti, “Double-degenerate Fermi mixtures of $^{6}$Li and $^{53}$Cr atoms,” *Phys. Rev. A*, vol. 106, p. 053318, Nov 2022.

[65] M. Zaccanti, “Mass-imbalanced Fermi mixtures with resonant interactions,” 2023.

[66] L. Landau and E. Lifshits, *Quantum Mechanics: Non-Relativistic Theory.* A-W series in advanced physics, Oxford: Pergamon Press, 1977.

[67] M. Baranger, “Simplified quantum-mechanical theory of pressure broadening,” *Phys. Rev.*, vol. 111, pp. 481–493, Jul 1958.

[68] M. Baranger, “General impact theory of pressure broadening,” *Phys. Rev.*, vol. 112, pp. 855–865, Nov 1958.

[69] D. S. Petrov, “The few-atom problem,” 2012.

[70] H. Bethe and R. Peierls, *Proceedings of the Royal Society of London Series A*, vol. 148. Royal Society, 1935.

[71] E. Soave, A. Canali, Z.-X. Ye, M. Kreyer, E. Kirilov, and R. Grimm, “Optically trapped feshbach molecules of fermionic 161dy and 40k,” 2023.

[72] M. Inguscio, W. Ketterle, and C. Salomon, eds., *Ultra-cold Fermi gases*, vol. 164 of *Proceedings of the International School of Physics “Enrico Fermi"*, (Amsterdam), IOS press, 2007.

[73] S. Giorgini, L. P. Pitaevskii, and S. Stringari, “Theory of ultracold atomic fermi gases,” *Rev. Mod. Phys.*, vol. 80, pp. 1215–1274, Oct 2008.

[74] W. Zwerger, ed., *The BCS-BEC Crossover and the Unitary Fermi Gas*, vol. 836 of *Lecture Notes in Physics.* Springer Berlin Heidelberg, 2012.

[75] L. Radzihovsky and D. E. Sheehy, “Imbalanced feshbach-resonant fermi gases,” *Rep. Progr. Phys.*, vol. 73, no. 7, p. 076501, 2010.

[76] $T_{F,i} = \hbar\bar{\omega}_i(6N_i)^{1/3}/k_B$ denotes the Fermi temperature of a gas of $N_i$ atoms, $i = Li, Cr$, trapped in a harmonic potential with average angular frequency $\bar{\omega}_i$.

[77] C. Simonelli, E. Neri, A. Ciamei, I. Goti, M. Inguscio, A. Trenkwalder, and M. Zaccanti, “Realization of a high power optical trapping setup free from thermal lensing effects,” *Opt. Express*, vol. 27, pp. 27215–27228, Sep 2019.

[78] E. Neri, *Mass imbalanced Fermi mixtures with 2- and 3-body resonant interactions.* PhD thesis, University of Florence, 2019.

[79] I. Goti, “Towards the production of ultracold mixtures of lithium and chromium atoms,” Master’s thesis, Università degli Studi di Firenze, 2019.

[80] S. Finelli, “Ultracold chromium - lithium fermionic mixtures with resonant interactions,” Master’s thesis, Università degli Studi di Firenze, 2021.

[81] A. Burchianti, G. Valtolina, J. A. Seman, E. Pace, M. De Pas, M. Inguscio, M. Zaccanti, and G. Roati, “Efficient all-optical production of large $^6$Li quantum gases using $D_1$ gray-molasses cooling,” *Phys. Rev. A*, vol. 90, p. 043408, Oct 2014.

[82] H. Metcalf, P. Van der Straten, J. Birman, J. Lynn, H. Stanley, M. Silverman, and M. Voloshin, *Laser Cooling and Trapping.* Graduate texts in contemporary physics, Springer, 1999.

[83] F. P. D. Santos, F. Perales, J. Léonard, A. Sinatra, J. Wang, F. S. Pavone, E. Rasel, C. S. Unnikrishnan, and M. Leduc, "Efficient magneto-optical trapping of a metastable helium gas," *The European Physical Journal - Applied Physics*, vol. 14, no. 1, pp. 69–76, 2001.

[84] R. Chang, A. L. Hoendervanger, Q. Bouton, Y. Fang, T. Klafka, K. Audo, A. Aspect, C. I. Westbrook, and D. Clément, "Three-dimensional laser cooling at the doppler limit," *Phys. Rev. A*, vol. 90, p. 063407, Dec 2014.

[85] G. Bismut, B. Pasquiou, D. Ciampini, B. Laburthe-Tolra, E. Maréchal, L. Vernac, and O. Gorceix, "Optimized loading of an optical dipole trap for the production of chromium becs," *Applied Physics B*, vol. 102, pp. 1–9, Jan 2011.

[86] G. Zürn, T. Lompe, A. N. Wenz, S. Jochim, P. S. Julienne, and J. M. Hutson, "Precise characterization of $^{6}$Li feshbach resonances using trap-sideband-resolved rf spectroscopy of weakly bound molecules," *Phys. Rev. Lett.*, vol. 110, p. 135301, Mar 2013.

[87] C. Ticknor, C. A. Regal, D. S. Jin, and J. L. Bohn, "Multiplet structure of feshbach resonances in nonzero partial waves," *Phys. Rev. A*, vol. 69, p. 042712, Apr 2004.

[88] Y. Cui, C. Shen, M. Deng, S. Dong, C. Chen, R. Lü, B. Gao, M. K. Tey, and L. You, "Observation of broad $d$-wave feshbach resonances with a triplet structure," *Phys. Rev. Lett.*, vol. 119, p. 203402, Nov 2017.

[89] B. Zhu, S. Häfner, B. Tran, M. Gerken, J. Ulmanis, E. Tiemann, and M. Weidemüller, "Spin-rotation coupling in p-wave Feshbach resonances," 2019.

[90] W. J. Childs, L. S. Goodman, and D. von Ehrenstein, "Magnetic hyperfine interaction of $^{53}$Cr," *Phys. Rev.*, vol. 132, pp. 2128–2135, Dec 1963.

[91] E. Arimondo, M. Inguscio, and P. Violino, "Experimental determinations of the hyperfine structure in the alkali atoms," *Rev. Mod. Phys.*, vol. 49, pp. 31–75, Jan 1977.

[92] V. Gurarie, L. Radzihovsky, and A. V. Andreev, "Quantum phase transitions across a $p$-wave feshbach resonance," *Phys. Rev. Lett.*, vol. 94, p. 230403, Jun 2005.

[93] T. D. Cumby, R. A. Shewmon, M. G. Hu, J. D. Perreault, and D. S. Jin, "Feshbach-molecule formation in a bose-fermi mixture," *Phys. Rev. A*, vol. 87, no. 012703, 2013.

[94] E. Hodby, S. T. Thompson, C. A. Regal, M. Greiner, A. C. Wilson, D. S. Jin, E. A. Cornell, and C. E. Wieman, "Production efficiency of ultracold

feshbach molecules in bosonic and fermionic systems," *Phys. Rev. Lett.*, vol. 94, no. 120402, 2005.

[95] C. Chin and R. Grimm, "Thermal equilibrium and efficient evaporation of an ultracold atom-molecule mixture," *Phys. Rev. A*, vol. 69, p. 033612, Mar 2004.

[96] S. J. J. M. F. Kokkelmans, G. V. Shlyapnikov, and C. Salomon, "Degenerate atom-molecule mixture in a cold fermi gas," *Phys. Rev. A*, vol. 69, p. 031602, Mar 2004.

[97] F. Scazza, G. D. Pace, L. Pieri, R. Concas, W. J. Kwon, and G. Roati, "An efficient high-current circuit for fast radio-frequency spectroscopy in cold atomic gases." 2021.

[98] L. Fallani and M. Inguscio, *Atomic Physics: Precise Measurements and Ultracold Matter.* Oxford University Press, 2013.

[99] Wikipedia. Near and far field, `https://en.wikipedia.org/wiki/Near_and_far_field`.

[100] M. Steer, *Microwave and RF Design III - Networks.* Open Education Resource (OER) LibreTexts.

[101] Wikipedia. Scattering matrix, `https://en.wikipedia.org/wiki/S-matrix`.

[102] J. M. Fiore, *AC Electrical Circuit Analysis: A Practical Approach.* Open Education Resource (OER) LibreTexts.

[103] Wikipedia. Smith chart, `https://en.wikipedia.org/wiki/Smith_chart`.

[104] S. W. Ellingson, *Electromagnetics I.* Virginia Tech University.

[105] QUCS Software, `https://qucs.sourceforge.net/`.

[106] Wikipedia. Characteristic impedance, `https://en.wikipedia.org/wiki/Characteristic_impedance`.

[107] Wikipedia. `Coaxial cable, https://en.wikipedia.org/wiki/Coaxial_cable`.

[108] B. Adamczyk. InCompliance, `https://incompliancemag.com/article/balanced-unbalanced-antenna-structures-and-baluns/`.

[109] MiniCircuits. Directional coupler, `https://blog.minicircuits.com/directional-couplers-their-operation-and-application`.

[110] G. Breit and I. I. Rabi, "Measurement of nuclear spin," *Phys. Rev.*, vol. 38, pp. 2082–2083, 1931.

[111] `https://eepublicdownloads.entsoe.eu/clean-documents/pre2015/publications/ce/oh/appendix1_v18.pdf`.